Title
Polymer-Ceramic MEMS Bimorphs as Thermal Infrared Sensors

Author
Warren, Clinton Gregory

Publication Date
2010

Peer reviewed|Thesis/dissertation

Polymer-Ceramic MEMS Bimorphs as Thermal Infrared Sensors

by

Clinton Gregory Warren

A report submitted in partial satisfaction of the

requirements for the degree of

Doctor of Philosophy

in

Mechanical Engineering

in the

Graduate Division

of the

University of California, Berkeley

Committee in charge:

Professor Albert P. Pisano, Chair
Professor Luke P. Lee
Professor Liwei Lin

Spring 2010

Polymer-Ceramic MEMS Bimorphs as Thermal Infrared Sensors

Clinton Gregory Warren

Abstract

Polymer-Ceramic MEMS Bimorphs as Thermal Infrared Sensors

by

Clinton Gregory Warren

Doctor of Philosophy in Mechanical Engineering

University of California, Berkeley

Albert P. Pisano, Chair

Thermal infrared detectors based on MEMS bimorph beams have the potential to exceed the performance of current uncooled thermal infrared cameras both in terms of sensitivity and cost. These cameras are part of a rapidly growing industry are used for a vast array of applications such as military and civilian night vision, industrial monitoring, and medical imaging. Many researchers have explored the use of metal-ceramic MEMS bimorphs for this application even though it has long been acknowledged that polymer-ceramic bimorphs would be superior. However, because of the difficulties of designing and fabricating MEMS systems based on polymer-ceramic bimorphs, little progress has been made towards their development.

This dissertation describes the initial design, fabrication, and testing of thermo-mechanical infrared sensors based on MEMS polymer-ceramic bimorph beams. Sensors based on bimorphs composed of both the biopolymer chitin on poly-silicon and OCG-825 photoresist on poly-silicon were fabricated and tested. Chitin bimorphs were fabricated using a novel photolithographic chitosan process previously developed for this research.

A sensor design based on a residual stress and ambient temperature compensating geometry and which includes novel features such as vertically aligned thermal isolation regions and selective shielding is presented. Simplified sensors were tested using an optical readout method where the deformation of the sensors was observed as variations in the intensity of visible light reflected to a digital camera. In order to obtain quantitative measurements, image analysis was performed. While the feasibility of simply observing the average brightness of the light reflected from a sensor was demonstrated, several image processing algorithms were tested and shown to increase the signal to noise ratio. An IR source approximating a blackbody was combined with a series of filters and lenses to limit transmission of light to the sensor to wavelengths from approximately 1.0 to 3.6 μm.

A periodic signal was produced by coupling a mechanical chopper wheel with the IR source. The sensor was able to detect these signals at frequencies of at least 5 Hz. By comparing the sensor signal to a known rate of warming of the IR source and the measured noise level at equilibrium, a noise equivalent temperature difference of as low as 360 mK was

measured. In light of this encouraging and clear proof of concept, suggestions for achieving performance gains and developing novel imaging systems based on polymer-ceramic bimorphs through future research efforts are offered.

Dedication

To my dear brother Jackson: a true scholar, artist, and friend

Table of Contents

List of Figures

List of Tables

Acknowledgements

I would first like to express my sincere gratitude to my advisor, Prof. Albert P. Pisano, for his ongoing guidance and mentorship. I could not have hoped for a more positive graduate experience or an advisor better matched to my style of learning or more supportive of my goals. I would also like to thank the other members of my dissertation committee: Prof. Liwei Lin and Prof. Luke Lee for their counsel and encouragement.

This work was made possible by the generous support of our industry partner, Textron Systems. I am especially grateful to Mrs. Emel Bulat for her support of this project and of my education. I am thankful for the unique opportunity to have worked closely with Dr. Dennis Pease at IST – Textron Systems in Goleta, CA. Additional funding was provided by the State of California through the UC Discovery Grant.

This work greatly benefited from the collective wisdom of my research group, Berkeley Micromechanical Analysis and Design. Dr. Jim Cheng and Dr. Matt Hopcroft, BMAD research specialists, were especially helpful and both made significant contributions to this research. Thanks to David Myers for training and Nuo Zhang for her work on chitosan conversion.

I would also like to acknowledge my predecessor, Dr. Michael Mueller, whose work established this project and set the direction for its future. Dr. Cheng's previous work on chitosan was also crucial to this work.

I would not have endured the stress of laboratory research were it not for the support of my good friends Andrew Sullivan, Clifford Mak, and Brent Webster.

Finally, I am grateful for the tireless love and encouragement of my parents Thomas and Kathleen who taught me a love of learning and provided me with limitless opportunity.

Chapter 1: Introduction

1.1 Overview

The long term goal of this research is to utilize microfabricated polymer-ceramic MEMS bimorph structures as highly sensitive, uncooled, thermo-mechanical infrared detectors with inherent wavelength specificity and which can be manufactured at a low cost. A bimorph beam, which is a beam composed of two layers of dissimilar materials, will deform with a change in temperature due to the difference in coefficients of thermal expansion of the material. This effect is commonly utilized in bimetal thermostats, for example. The bending of a bimorph infrared detector is a function of its temperature, which is proportional to the intensity of infrared radiation it receives. The mechanical deformation of the detector is then sensed by one of a variety of possible methods. Such devices have several advantages over the predominant uncooled infrared technology including reduced noise, larger temperature conversion sensitivity, and tunable wavelength sensitivities.

Infrared detectors are typically fabricated in microarrays which are incorporated into an imaging system where the detector array is positioned at the focal plane of an infrared lens and is connected to readout and supporting electronics. A schematic representation of a typical infrared imaging system with a two-dimensional (or staring[1]) array of detectors is shown in Fig. 1, below.

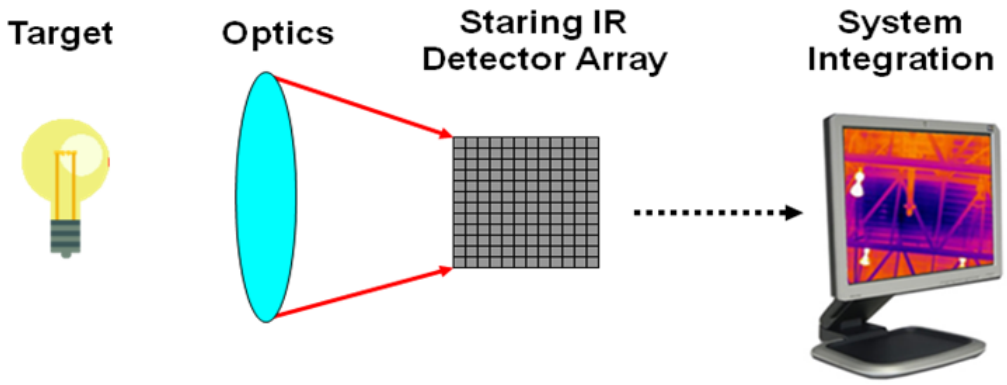

Figure 1. Schematic of typical infrared imaging system

This research focuses on the detector elements themselves, rather than on an entire integrated infrared imaging system. A simplified schematic representation of a bimorph thermo-mechanical infrared sensor is presented in Fig. 2, below, and serves to introduce the general concept of thermo-mechanical infrared sensors. The sensor itself is composed of two layers of different materials and is isolated from the substrate by an insulating anchor. When the structure absorbs infrared radiation, the differential thermal expansion of the two layers causes a

[1] A staring array is a two-dimensional array placed at the focal plane of an optical lens which, unlike one dimensional arrays or single element detectors, does not require scanning in order to produce a two dimensional image.

mechanical deflection. In the example shown in Fig. 2, the structure and the substrate act as a variable gap capacitor and electrical measurements can be correlated to infrared intensity. Alternatively, the structure may act as a visible light reflector for use with an optical readout mechanism.

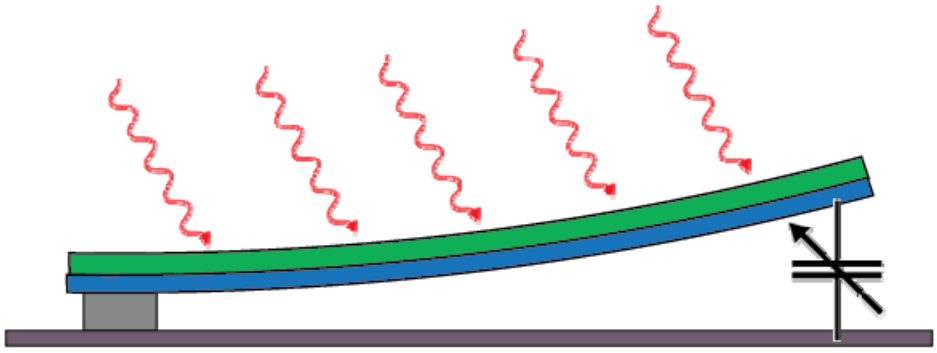

Figure 2. Schematic of bimorph cantilever infrared detector (capacitive readout)

Many researchers have explored the use of metal-ceramic MEMS bimorphs for use as thermal infrared detectors, even though it has long been acknowledged that polymer-ceramic bimorphs would be superior due to the potential for a greater mismatch in the coefficients of thermal expansion between polymers and ceramics. However, because of the difficulties of designing and fabricating MEMS systems based on polymer-ceramic bimorphs, little progress has been made towards their development.

This dissertation describes the design, fabrication, and experimental testing of thermo-mechanical devices based on MEMS polymer-ceramic bimorph beams and demonstrates the feasibility of using these structures as thermal infrared detectors. Sensors utilizing bimorphs composed of both OCG-825 photoresist on poly-silicon and the biopolymer chitin on poly-silicon were fabricated. Photoresist was chosen due to the ease with which it can be used in fabrication and chitin was selected based on its use in the highly sensitive infrared organs of the beetle, *Melanophila acuminata* [1]. A novel chitosan photolithography process was previously developed for this research and expanded upon in this work.

Fabricated sensors were experimentally tested using both optical and capacitance readout methods. The most promising results were obtained through the optical readout method which used a digital camera to observe the change in the reflection of visible light from the sensors as they mechanically deformed in response to infrared light. Signals created by a mechanical chopper wheel, which periodically blocked light from an IR source, were recorded by the sensor at frequencies of at least 5 Hz (for a 28 Hz sampling rate). A noise equivalent temperature difference of as low as 360 mK was estimated based on the response of the sensors and noise measurements. Although these results should not be interpreted as being completely representative of the performance of these sensors (since testing was preliminary and performance figures were estimated for limited conditions), an encouraging and clear proof of concept was demonstrated.

1.2 Motivation

Two of the main goals of modern day infrared sensor research are to move further toward uncooled imagers and to make infrared cameras cheaper and more convenient to use [2]. To achieve these goals, the limitations of the dominant technology need to be addressed. This research aims to eventually enhance the performance and lower the overall cost of uncooled thermal infrared cameras. There is already a large commercial market for this technology. Over 100,000 uncooled infrared imaging chips were sold in 2007 [3]. FLIR Systems Inc., the largest stand-alone infrared company, generated $1.1 billion in revenue in 2008 [4].

Thermal infrared detectors are usually used in place of photon detectors due to their relatively low cost and low power requirements. Therefore, there is significant motivation in the research community to develop techniques to achieve better performance in thermal detectors at the same cost, or to reduce the cost, size, or power requirements while achieving the same performance. Another motivating factor for this research, recognized in the literature [5] and in industry, is to work toward thermal imaging systems that can simultaneously image multiple wavelength bands. Techniques that avoid expensive filtering, such as those that use multiple innovative absorbing materials, may be especially attractive.

1.2.1 Infrared Sensing Applications

While originally developed for military applications, infrared imagers have found myriad applications in a diverse array of industries. As early as 1969, a classic text on infrared systems listed over 100 applications [6] and as infrared technology has experienced profound advancements the number and diversity of applications has increased. That trend is expected to increase as uncooled cameras become increasingly affordable and usable. A brief, non-exhaustive, survey of applications, divided by category, is provided below.

Military

The best known military infrared systems are “heat-seeking” missiles, or missile defense systems, which utilize the infrared radiation emitted by a hot object such as a jet exhaust in order to track a target. Infrared cameras are also used for reconnaissance and navigation in the absence of visible light or through such obstacles as clouds or dust. Land mines and unexploded ordinance can also be detected by airborne infrared imaging [7]. Other applications include search and rescue and fire control.

Industrial

Virtually any industrial or chemical process involves the release or consumption of energy in the form of heat, and thermal observation can yield a wealth of information. Operating temperature is, by far, the most frequently measured property in industrial process control [8] and there are many possible motivations for remote temperature measurement. These include the need to measure targets which are small, fragile, moving, destructive, hazardous, or difficult to

access. Changes in operating temperatures are highly indicative of wear or fault, and are therefore observed for reasons of preventative maintenance. Electrical faults and impending failures can be observed by a remote operator using thermal imaging. There are many applications in manufacturing. For example, observation of temperature gradients in molding and casting processes can give a better understanding of non-uniformities and surface finishes. Finally, non-destructive testing of parts and structures can be performed by observations of heat flow [9].

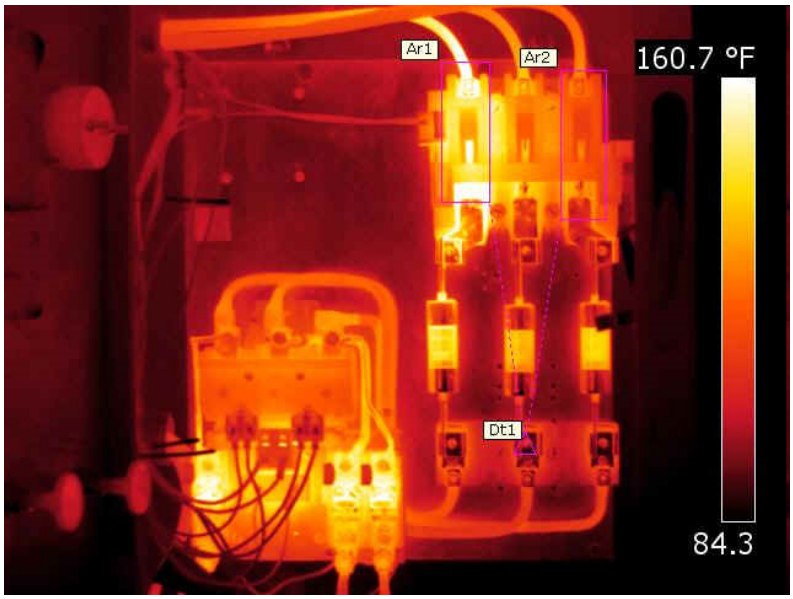

Figure 3. Thermographic image of electrical equipment [10]

Civil

The same technologies used for military applications have been adapted to law enforcement and fire fighting. Reduced light vision technologies are being utilized in civil aviation and automotive applications. In addition, infrared imaging is used extensively in building diagnostics [11] for such applications as detecting gaps in insulation and air leakage, studying HVAC systems, and detecting such problems as leaking roofs or trapped moisture inside walls or roofs. Energy audits, in particular, have been a source of growing interest, even at the consumer level [12]. Environmental applications related to climatology, pollution monitoring, and energy conservation are common. Finally, identification of individuals by their infrared image has been researched as a biometric [13].

Medical

Infrared imaging has been increasingly applied in the field of non-invasive medical imaging. Since factors such as inflammation, infection, blood flow, and arterial constriction all affect skin temperature, thermal patterns and trends can indicate a vast array of medical disorders. Reported medical applications include oncology (especially for mammography and skin cancers), deep venous thrombosis, diabetes, arthritis, brain injuries, burn injuries,

monitoring the efficacy of drugs, and sports medicine [14]. Measurements are made in several ways besides simple body temperature observations or static temperature distributions. For example, thermal imaging of the re-warming of fingers which had previously been immersed in cold water was shown to help evaluate vascular function, thereby successfully diagnosing repetitive stress injuries in a controlled trial [15]. Static temperature measurements of the same patients were not able to diagnose these injuries.

1.2.2 Thermo-mechanical Sensors as a Platform Technology

In addition to infrared detection, this research could readily be applied to many other applications. The same mechanism could easily be adapted for the measurement of other sources of heat and has been demonstrated, for example, by the precise measurement of chemical reactions [16]. Thermo-mechanical MEMS systems can also be used as actuators, switches, and valves when combined with simple heaters. In addition, any progress in the readout mechanisms for thermo-mechanical sensors can be applied to many other forms of sensors. Finally, and as will be discussed below, polymer thin films and bimorphs have been used for a host of applications and so this research can be viewed as having broader motivation outside of that solely from infrared sensing.

1.3 Background - Infrared Sensors

This section will introduce some of the fundamental equations relevant to infrared sensors. It will also discuss the various types of infrared detectors, with a focus on the theory of thermal infrared detectors in general and thermo-mechanical detectors in specific.

1.3.1 Fundamental Equations

Generally speaking, infrared light is simply electromagnetic radiation characterized by wavelengths longer than that of red visible light and shorter than about 300 μm. Unlike visible light, however, infrared light it is emitted in significant amounts by all objects above cryogenic temperatures. The ability to "see" infrared light, therefore, greatly increases our ability to sense the world around us.

Planck's blackbody law gives the power density, M, emitted by a blackbody at a given wavelength, λ, and temperature, T:

$$M(\lambda,T) = \frac{2hc^2}{\lambda^5}\left(\frac{1}{e^{\left(\frac{hc}{\lambda kT}\right)}-1}\right) \quad \left[\frac{W}{m^2\cdot\mu m}\right] \tag{1}$$

where h is Planck's constant ($6.626\times10^{-34}\,J\cdot s$), c is the speed of light ($2.998\times10^{8}\ m/s$), and k is Boltzmann's constant ($1.381\times10^{-23}\,J/K$). For a given temperature and wavelength, Planck's law describes the maximum, or ideal, amount of energy that an object can emit. The

peak wavelength of emission, the wavelength with the maximum emitted power density, for a given temperature is given by Wien's Law:

$$\lambda_{max} = \frac{2897\ mm \cdot K}{T} \tag{2}$$

Integrating Eq. (1) over all wavelengths yields the Stefan-Boltzmann law, which gives the total rate of energy emitted per surface area of a black body at temperature, T:

$$P = \int_0^\infty M(\lambda, T) d\lambda = \sigma T^4 \quad \left[\frac{W}{m^2}\right] \tag{3}$$

where σ is the Stefan Boltzmann constant and is equal to $5.67 \times 10^{-8}\ W/(m^2K^4)$. However, since an object "sees" its surroundings and is receiving radiation as well as emitting it, the actual heat transfer due to radiation is given by:

$$q_{rad} = \epsilon A \sigma (T^4 - T_{sur}^4) \tag{4}$$

where T_{sur} is the temperature of the surroundings and convenience we assume the body has a surface emissivity, ϵ, which is independent of wavelength. In reality, the emissivity of an object usually depends on wavelength, temperature, emission angle, and thickness. A target (or an object of interest) can only be detected if its emitted power, M_T, is different than the background power, M_B, emitted by the surroundings. The power difference between the two is given by:

$$\Delta M = M_T - M_B = \sigma (T_T^4 - T_B^4) \tag{5}$$

where T_T and T_B are the temperatures of the target and the background, respectively. For small differences between the temperature of the target and the temperature of the background:

$$\Delta M \approx 4\sigma T_B^3 \Delta T \tag{6}$$

where $\Delta T = (T_T - T_B)$ [17]. A target can only be detected if the sensor has sufficient sensitivity to detect ΔM, which can be quite small in relation to the magnitude of the emitted power from the background. It should be noted that ΔM is proportional to the cube of T_B, so as the background temperature increases, so does the power difference for a given temperature difference of a target.

1.3.2 Infrared Wavelength Bands

The infrared spectrum has historically been divided into three or more bands of wavelengths. Wavelengths from approximately 1.1 to 2.5 μm are referred to as short wavelength infrared (SWIR). The mid-wavelength infrared (MWIR) band spans approximately 2.5 to 7.0 μm and the long wavelength infrared (LWIR) band ranges from about 7 to 15 μm. Wavelengths longer than 15 μm are referred to as either far infrared (FIR) or very long range infrared (VLWIR). Due to differences in the transmissibility of IR light through the atmosphere

according to wavelength, interest has mainly focused on the two "atmospheric windows", the MWIR window from about 3-5.5 μm and the LWIR window from about 8-14 μm. The LWIR window also encompasses the peak emissivity wavelength of ~10 μm for objects at a temperature of around 300 K. These two imaging windows are illustrated in Fig. 4, below, in which the typical transmittance through a one kilometer path length in air is shown. Actual transmission in the atmosphere depends on a variety of factors such as humidity, particulates, etc. The absorbing molecules primarily responsible for the atmospheric absorption of particular wavelengths are also shown in Fig. 4.

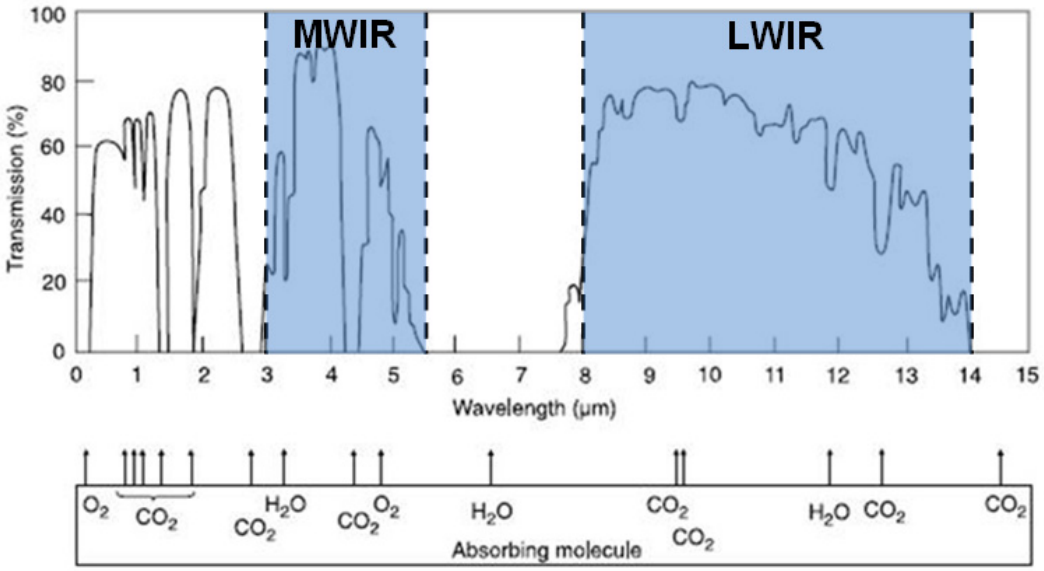

Figure 4. Atmospheric transmission of infrared light, with absorbing molecules indicated [18]

Though narrow wavelength windows are typically used for imaging, it should be noted that for a 10 m path length, transmission is typically greater than 60% for any wavelength from 3-14 μm, and at 10 km only a very narrow band at 4 μm typically exceeds 10% transmission [17]. Consideration should be given to the anticipated range of targets to be detected and the target wavelength of imaging systems since, for example, wavelengths in the 6-7 μm range can only be detected at close range.

Wavelength windows for imaging systems are chosen based on atmospheric transmission and the emission of anticipated targets. The spectral emissive power of blackbody objects at various temperatures, predicted by Plank's blackbody law, Eq. (1), is shown in Fig. 5, below. The peak spectral emittance of an object at room temperature, or about 300 K, is approximately 10 μm and falls within the LWIR atmospheric window. Therefore, when attempting to detect variations in a background at ambient temperature most imaging systems are designed for the MWIR and LWIR atmosphere windows. Objects at about 600 K start to emit some of their power within the visible range and therefore start to appear "red hot". A blackbody at 1000 K, the approximate temperature of a wood fire, has a peak spectral emittance at about 3 μm which falls within the MWIR atmospheric window. The sun, with an effective radiation temperature of about 5800 K, emits most strongly in the visible portion of the electromagnetic spectrum. However, the majority of the energy emitted by the sun is in the form of infrared light.

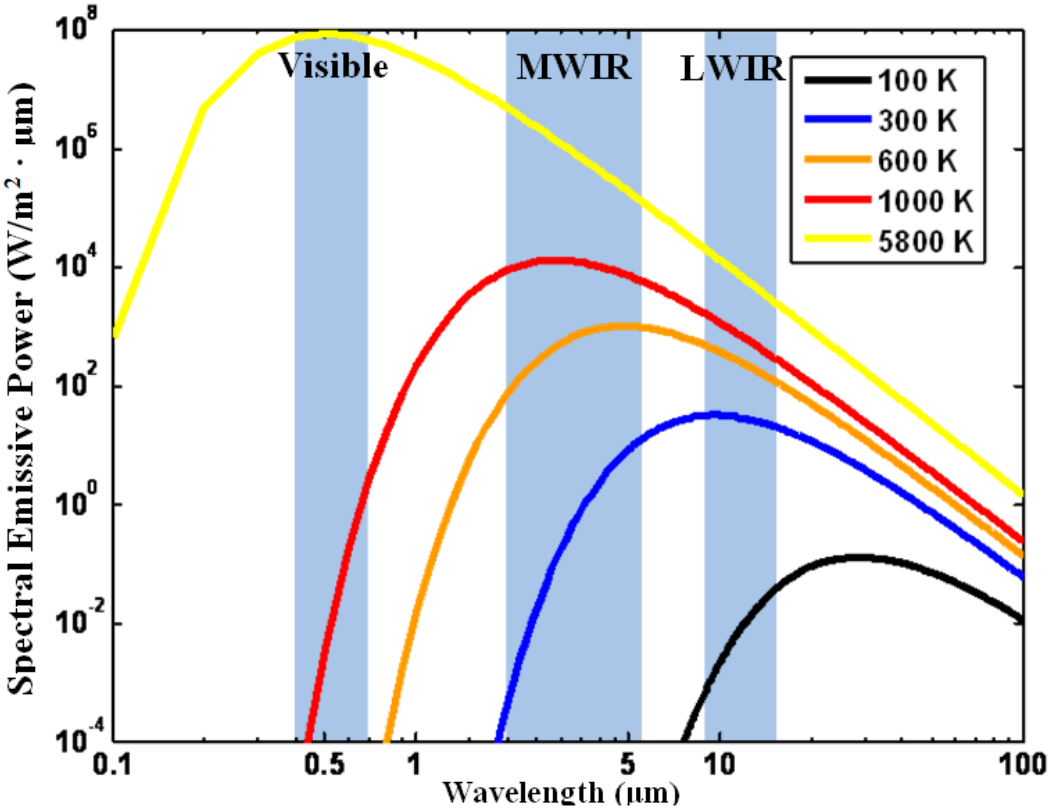

Figure 5. Planck's distribution for sample blackbody target temperatures

1.3.3 Types of Infrared Detectors (Photon vs. Thermal)

In general, infrared detectors are divided into two classes based on their fundamental operating principle. Photon detectors are detectors in which absorbed infrared radiation excites electronic transitions within the material. These transitions cause a change in some output signal, which is then sensed by a variety of mechanisms. They tend to have narrow wavelength sensitivity, extremely fast response, and, when cooled, exhibit very low noise.

Thermal detectors, on the other hand, are detectors where infrared radiation is absorbed and causes a change in the temperature of the detector which changes some property of the material. Since the mechanism of detection is independent of the photonic nature of the infrared light, thermal IR detectors are usually sensitive to a very broad range of wavelengths. Broadband sensitivity can be an advantage or a disadvantage, depending on the application.

A major difference between the two classes of detectors is the need for active cooling. In order to image objects at or near room temperature, photon detectors must have a forbidden energy gap of no greater than 0.25 eV (for 5 µm). However, a small band gap leads to large fluctuations in the generation and recombination of thermally generated charge carriers, which is referred to as "g-r noise" [19]. Therefore, for operation at wavelengths longer than about 3 µm, photon detectors usually require cryogenic cooling in order to reduce thermally generated charge carriers which compete with target signals[20]. Unfortunately, cryogenic cooling systems force stringent requirements on infrared cameras. It has been reported [21] that without these cooling systems, infrared cameras can be up to a hundred times smaller, use twenty times less power, and

cost around ten times less. Cooled photon imagers typically cost at least $50,000 [22]. Due to this high cost and the relatively high power consumption needed for cooling, photon imagers are not suitable for low cost, low power applications for wavelengths longer than about 3 μm.

Although photon detectors generally exhibit superior signal-to-noise ratios compared to thermal detectors, it is easier to create two-dimensional arrays with uncooled thermal detectors. Arrays have a smaller system noise bandwidth than scanning (one-dimensional) arrays which helps to compensate for higher noise [19]. Thermal detectors are characterized by modest response speeds compared to photon detectors, due to the thermal inertia of the sensing elements. However, thermal staring arrays, arrays arranged in a two-dimensional grid, can easily operate at TV frame rates of 30 Hz. Thermal detectors can also be designed so that their thermal time constant acts to integrate signals over the frame time of an imager, enhancing performance [23].

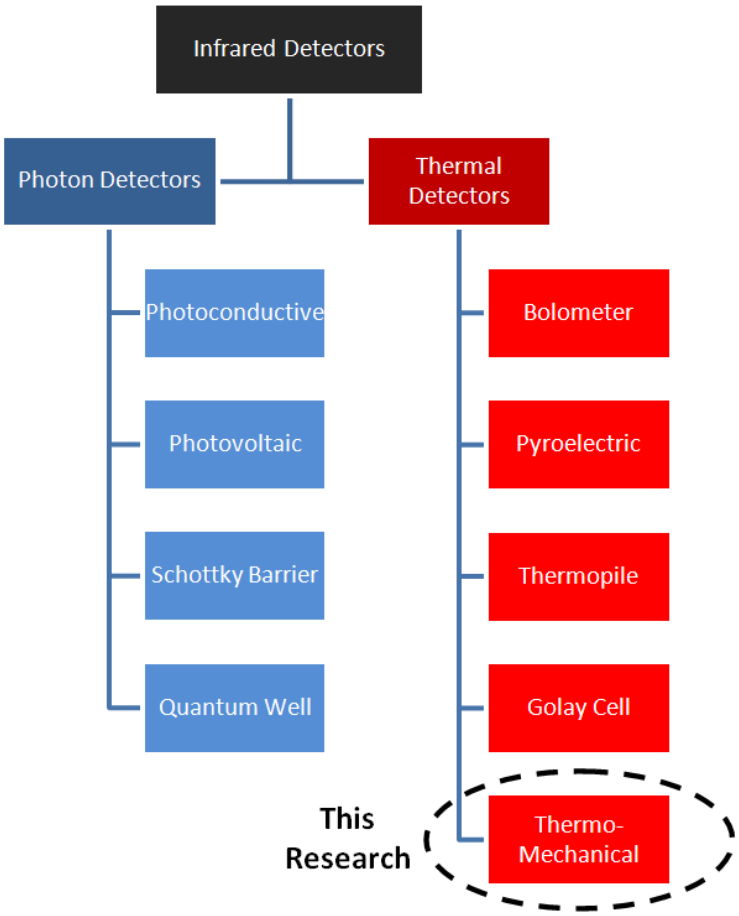

Figure 6. Infrared technology tree showing the major types of detectors

Though not exhaustive, a technology tree illustrating the major types of infrared detectors is presented in Fig. 6, above. Within thermal detectors, a variety of methods are used to sense the change in temperature of the detector element. Bolometers operate based on the change in electrical resistance of a material with a change in temperature, and will be discussed in more depth below. Pyroelectric detectors operate based on the change in the internal electric field within ferroelectric materials and required a chopped signal since they generate no signal in

equilibrium. Thermopiles utilize the Seebeck effect between dissimilar metals, the same principle used in thermo-couples. Golay cells utilize the thermal expansion of a gas in a small chamber to deflect a membrane. Thermo-mechanical detectors are the focus of this research, and will be discussed in depth.

1.3.4 Thermal Detector Theory

In principle, a thermal infrared detector is simply a temperature sensor designed to only interact with incident radiant energy while minimizing all other thermal contacts with its surroundings [22]. The general theory of thermal detectors has been analyzed in depth. Here we follow the analysis of Putley [24].

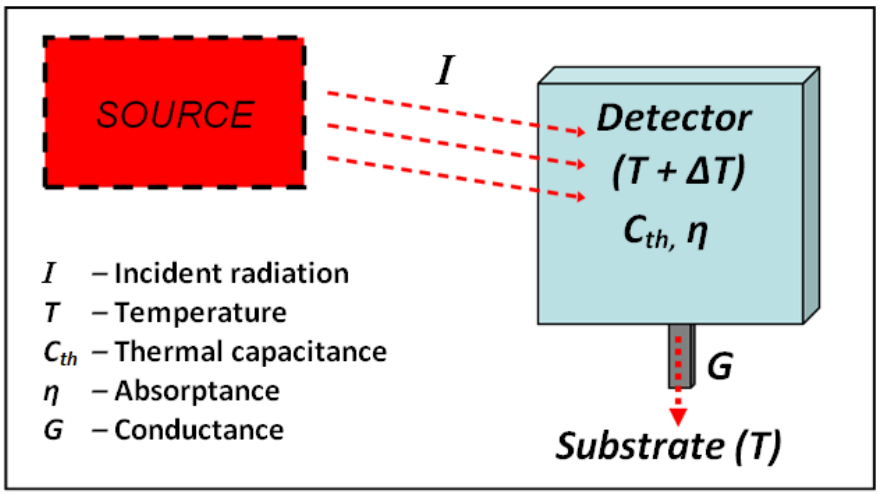

Figure 7. Thermal detector schematic diagram

A simplified schematic of a representative thermal detector is shown in Fig. 7, above. The detector is necessarily connected to a substrate by one or more supporting beams. The substrate, being much larger than the detector itself, acts as a heat sink and is assumed to remain at a constant temperature, T. The supporting beams have thermal conductance, G, to the substrate. The detector element is characterized by, C_{th}, its thermal capacitance.

The incident radiation can be assumed to have both a steady state and periodic component and therefore takes the following form:

$$I = I_0 + I_\omega e^{j\omega t} \tag{7}$$

The heat transfer equation, assuming conduction and convention to the ambient and radiative heat transfer to the substrate are negligible compared to conduction through the supports, is:

$$\eta I = C_{th}\left(\frac{d\Delta T}{dt}\right) + G\Delta T \tag{8}$$

where ΔT is the rise in temperature of the detector over the temperature of the substrate and η is the fraction of the incident power which is actually absorbed by the detector. The temperature rise of the detector due to the periodic component of the incident radiation is given by:

$$\Delta T_\omega = \frac{\eta I_\omega}{\sqrt{G^2 + \omega^2 C_{th}^2}} \tag{9}$$

and the phase shift of the detector fluctuation is:

$$\varphi = \tan^{-1}\left(\frac{\omega C_{th}}{G}\right) \tag{10}$$

The characteristic thermal response time is the ratio of the thermal mass to the conductance:

$$\tau = \frac{C_{th}}{G} \tag{11}$$

Depending on the type of thermal detector, a variety of methods are utilized to convert the temperature change of the detector to an electronic signal. In general, the voltage responsivity, R_s, is given by the voltage of the output signal from a detector, V_s, divided by the radiant power incident upon the detector, P_o.

$$R_s = \frac{V_s}{P_o} \tag{12}$$

The noise equivalent power (NEP) is the radiant power incident upon the detector which would be required to generate a voltage signal, V_N equal to the root mean square of the noise in a detector for a given bandwidth.

$$NEP = \frac{V_N}{R_s} \tag{13}$$

A commonly used figure of merit is the detectivity (D^*), given by:

$$D^* = \frac{\sqrt{A_D \Delta f}}{NEP} \quad \left[\frac{cm \cdot \sqrt{Hz}}{watt}\right] \tag{14}$$

where A_D is the active surface area of the detector, and Δf is the measurement bandwidth. The units $cm\sqrt{Hz}/W$ are also referred to as "Jones", in honor of R. Clark Jones who originally defined them [25]. In order to maximize the detectivity of a sensor, the NEP should be minimized. Some sources of noise, such a temperature noise, are common to all thermal infrared detectors, while some are relevant only to specific types of thermal detectors. First, the ultimate limiting factors for the performance of thermal detectors will be considered. Sources of noise for specific types of sensors, specifically micro-bolometers and thermo-mechanical detectors, will be discussed separately.

Limits of Thermal Detectors

Fundamentally, all infrared detectors are limited in their performance by the random fluctuations in temperature due to the statistical nature of heat transfer [26]. Temperature fluctuations will arise due to the interaction between the detector area and the substrate, even if they are in thermal equilibrium [19]. If interactions between the substrate and the detector are minimized, the fundamental limit of performance is due to fluctuations in the background radiation. A detailed analysis of these limits has been previously performed by Kruse, *et al*. [27] but will be omitted here, except for the results.

The mean power fluctuation due to temperature fluctuation noise is given by:

$$P_{TF} = \sqrt{4kT^2G\Delta f} \tag{15}$$

and the corresponding spectral noise voltage due to temperature fluctuation is:

$$V_{TF}^2 = \frac{4kT^2\Delta f R_s}{G(1+\omega^2\tau_{th}^2)} \tag{16}$$

In the case that interactions with the substrate are made insignificant, radiation temperature noise will dominate. For a 2π field of view, the radiation background limit temperature noise voltage is:

$$V_{TF}^2 = \frac{kR_s\Delta f}{\sigma T A_d(1+\omega^2\tau_{th}^2)} \tag{17}$$

Based upon the radiation background limit, for a thermal detector operating at room temperature and viewing a background at room temperature, the highest detectivity (D^*) possible is $1.98 \times 10^9 cm\sqrt{Hz}/W$. [22].

Temperature Conversion Sensitivity

Temperature conversion sensitivity, related to voltage responsivity, V_s, can be generally defined as:

$$R_T = \frac{V_s}{\Delta T} \tag{18}$$

where ΔT is the temperature rise of the detector for a given power input, P_o. The temperature conversion sensitivity depends on the type of thermal detector and how it generates a signal. As an example, for a device in which a change in electrical capacitance due to temperature differences is measured, it is given by:

$$R_T = B \cdot TCC \tag{19}$$

where B is the gain of the capacitance readout circuitry and TCC is the temperature coefficient of capacitance and is itself defined as:

$$TCC = \frac{1}{C_S}\frac{\Delta C}{\Delta T} \tag{20}$$

where C_S is the capacitance of the sensor at equilibrium, and $\Delta C/\Delta T$ is the change in capacitance for a given change in temperature of the sensor. For a resistive bolometer, assuming no Joule heating and a constant measurement bias, i_b [19]:

$$R_T = i_b R \cdot TCR \tag{21}$$

where R is the electrical resistance of the sensor, and TCR is the temperature coefficient of resistance and is defined as:

$$TCR = \frac{1}{R}\frac{\Delta R}{\Delta T} \tag{22}$$

Design Goals for Thermal Detectors

Based on Eq. (9) above, some general principles for the design of a thermal detector can be developed. First, since maximizing ΔT_ω is clearly advantageous, the thermal conductance through the supports and the thermal mass of the detector must be minimized.

Limiting thermal conductance also reduces temperature noise, as shown in Eq. (15) above. However, any reduction of the thermal mass relative to the conductance results in an increase in the thermal response time, effectively slowing the response speed of the detector. Usually, a minimum detector response speed is determined by system requirements and the thermal mass is then minimized to the extent possible. Thermal detectors can also be designed so that their thermal time constant is similar to the frame time of the imaging system so that the detector itself performs a signal integration which can help compensate for a generally lower detectivity versus photon detectors [23].

The absorption of the detector, η, should be maximized since any radiation not absorbed is wasted. Accordingly, infrared cameras employ carefully chosen materials in the window and other optical components. Infrared windows are also usually treated with an anti-reflective coating and made from a material with very low absorption in the target wavelengths. Several methods exist for maximizing absorption within the detector element itself and these methods will be discussed in further depth below. Vacuum packaging has the benefit of improving thermal isolation by reducing conductance through the ambient and raising the quality factor [28].

Benefits of Scaling

There are a number of motivating factors that make MEMS technology particularly suited to thermal infrared detectors. First, the desire to minimize the thermal mass and maximize the absorption of detectors leads to thin film technologies, with their inherently high surface area to

volume ratios. In addition, the increased relative strength of beams at the micro-scale is favorable for creating structures which can be thermally isolated from their surroundings. Small detector size also allows for the creation of dense arrays of detectors which can be used for high resolution imaging. Two-dimensional arrays are called either staring arrays or focal plane arrays (FPA). Smaller detectors allow for the reduced size of infrared optical components which are extremely expensive and also significantly contribute to the overall size and weight of the system [2]. In addition, smaller pixels increase the detection range of IR imaging systems and allow for more arrays to be fabricated on a single wafer, thereby reducing cost [22]. However, decreasing the scale of detectors leads to problems with manufacturability, repeatability, and issues such as pixel cross-talk.

1.3.5 State of the Art

Infrared radiation was first discovered in 1800 by William Herschel upon observing its thermal effects. Accordingly, early infrared detector research was largely focused on thermal detectors until photon detectors were developed in the twentieth century. Single element cooled lead salt detectors were utilized as anti-aircraft seeker technology in the 1950s and 1960s [29]. The drive for night vision tools spurred the development of scanning linear arrays, however these systems were extremely large and heavy due to the high power requirements, mirror scanners, and cooling systems. Scanning linear arrays were also mounted in aircraft and utilized the motion of the aircraft to image terrain below [30]. Two-dimensional, or staring, arrays greatly simplified imaging systems and became commercially available in 1989. Much of the subsequent advancements stemmed from on-board processing capabilities and computer interfaces. In the mid 1990s, uncooled long wavelength cameras were developed based on micro-bolometers and ferroelectric detectors [8].

Infrared bolometers, or resistance bolometers, are thermal infrared sensors in which the change in temperature is measured by a change in the electrical resistance of the detector element. Uncooled bolometer arrays are currently the dominate technology in the majority of both commercial and military applications [3]. State of the art micro-bolometer cameras, manufactured by Raytheon, have 17 μm pixels in a 640 by 512 array and achieve a noise equivalent temperature difference (NETD) of less than 50 mK [31]. A schematic diagram of a typical micro-bolometer bridge pixel structure is presented in Fig. 8, below.

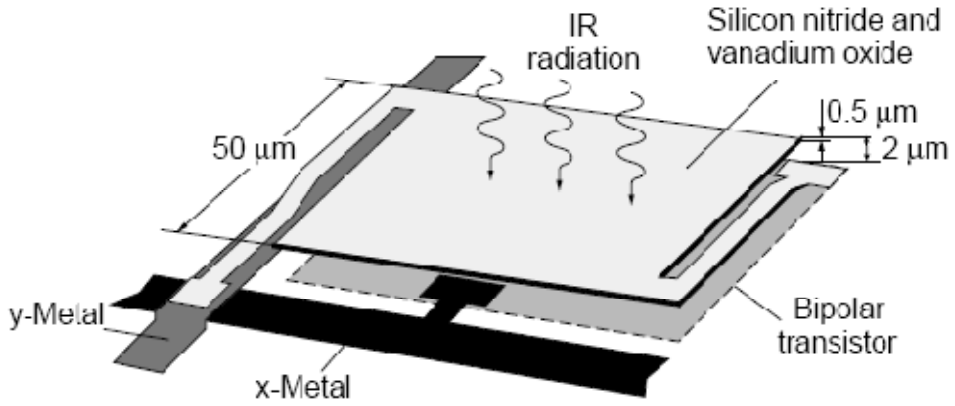

Figure 8. Micro-bolometer bridge pixel structure [32]

Limitations of Micro-bolometers

Micro-bolometers have several inherent limitations that may be overcome by competing technologies. First, due to the fact that they rely on the measurement of the electrical resistance of the sensor element, they necessarily require electrical connections which compromise the thermal isolation of the sensor because these electrical connections must be made from a material, such as a metal, with high thermal conductivity. Higher thermal conductance through these connections leads to higher temperature fluctuation noise. Also, measuring electrical resistance introduces significant Johnson and 1/f noise. Johnson noise is caused by the random thermal motion of electrical charges within a dissipative material and 1/f noise originates from a variety of sources is characterized by a spectral density that varies inversely with the frequency [33].

Another important issue related to micro-bolometers is the limitations of the available materials. An important material property is its temperature coefficient of resistance (TCR), the amount by which the electrical resistance of the material changes for a given temperature. The noise characteristics of the material are also important. The most commonly used thermistor material in micro-bolometers is vanadium oxide, VO_x, because it has a large temperature coefficient of resistance (up to about 4% per degree for a single element bolometer [22]). However, depositing films of VO_x with the intended material properties and reasonable uniformity is extremely difficult and expensive [34]. Many other materials such as metals and amorphous silicon have been used, but there is typically a tradeoff between cost and performance. A large amount of research has worked towards the goal of lower cost high performance micro-bolometers.

Micro-bolometer arrays also require precise temperature control due to the non-linear dependence of the material's electrical resistance on temperature [35, 36]. This requirement further contributes to the cost of the overall system and is further complicated by the fact that resistive measurements generate heat within the sensor itself.

As will be discussed later, thermo-mechanical sensors are not inherently limited in their responsivity by material properties and they exhibit neither Johnson nor 1/f noise in the detector element [37]. They can also be designed with superior thermal isolation, since they do not necessarily require electrical contact to the sensor, and they can be made to be largely insensitive to ambient temperature fluctuations. Their uniformity is primarily a function of the mechanical properties of thin films, rather than precise control of the TCR or noise characteristics of an exotic material. Due to these and other advantages, thermo-mechanical infrared sensors have the potential to surpass the performance and reduce the cost of the dominant uncooled infrared technology available today.

1.3.6 Thermo-Mechanical Infrared Sensors

Among the types of thermal infrared detectors, thermo-mechanical infrared sensors are those that convert the rise in temperature of the detector element to a mechanical deflection. A brief review of the literature is presented below, followed by a discussion of the various methods used to convert the mechanical deflection to a usable signal.

Literature Review

Although bimetallic strips had been used for many years, Barnes and Gimzeksi were the first to utilize microfabricated bimorph structures to measure changes in temperature [38, 39]. They utilized commercially available atomic force microscope (AFM) tips made of silicon nitride and coated one side with a thin layer of metal. Manalis *et al*. [40] first attempted to create a two-dimensional array of bimorph devices, in order to act as an infrared imager. They later fabricated silicon-aluminum bimorphs in the shape of spirals and measured the deflection by the change in the optical reflection. However, these devices were used only to detect a near-infrared laser. Majumdar *et al*. were the first to create an array which imaged thermal infrared [41]. They utilized silicon nitride and gold bimorphs with interdigitated fingers on a paddle [42, 43]. In this system, the readout was performed optically based on the diffraction of visible light. Majumdar's group later developed a multi-beamed structure utilizing coatings on the top and bottom (so-called "flip-over" bimorphs) of structural beams [44] in order to increase the deflection of sensor elements.

Datskos *et al*. at the Oak Ridge National Laboratory made significant process toward improving bimorph arrays. They worked on problems with repeatability and the influence of ambient temperature fluctuations by introducing a double leg design [45]. Much work has revolved around different readout techniques, to be discussed below. Several commercial ventures are currently pursuing thermo-mechanical bimorph infrared technology including Multispectral Imaging Inc. [37, 46] and Agiltron Inc. [47].

Readout Mechanisms

Since the result of absorbed infrared radiation in a thermo-mechanical sensor is mechanical displacement, many readout techniques are possible. Commonly employed techniques are capacitive, optical, piezoresistive, and electron tunneling.

Capacitance measurements work based on the same principles as a variable gap capacitor. When mechanical deformation occurs, the spacing between two conductive objects changes which results in a change in electrical capacitance. Various geometries have been attempted, but most designs have arms supporting a movable electrode. The capacitance between this movable electrode and an electrode on the substrate plane is then measured [48]. The capacitance measurement technique has the advantage of being compatible with standard CMOS readout circuitry, which could lead to very high volume manufacturing. This technique also directly produces an electronic signal which would be easily integrated into camera systems.

A variety of optical readout techniques have been explored, the first of which made use of commercial atomic force microscope systems which measure the reflection of the light from a laser off a cantilever [49, 50]. In these systems, the reflected laser is directed to a small array of photodiodes. Their relative outputs are used to infer the shifting of the laser beam associated with the deflection of the cantilever. AFM systems are extremely sensitive and allow for sub-angstrom sensitivities to be routinely achieved. Although useful for experimentation, these systems are difficult to scale to commercial applications and large arrays. Optical interference measurements, correlated with the displacement of a detector, have been made using white light interferometers [44]. Another optical approach is to utilize a charge-coupled device (CCD) camera to measure the reflection [40, 47] or diffraction [42] of visible light off an array of pixels.

These readout mechanisms usually utilize a laser as a visible light source and an aligned array of pinhole apertures between the sensor array and the CCD camera [51, 52].

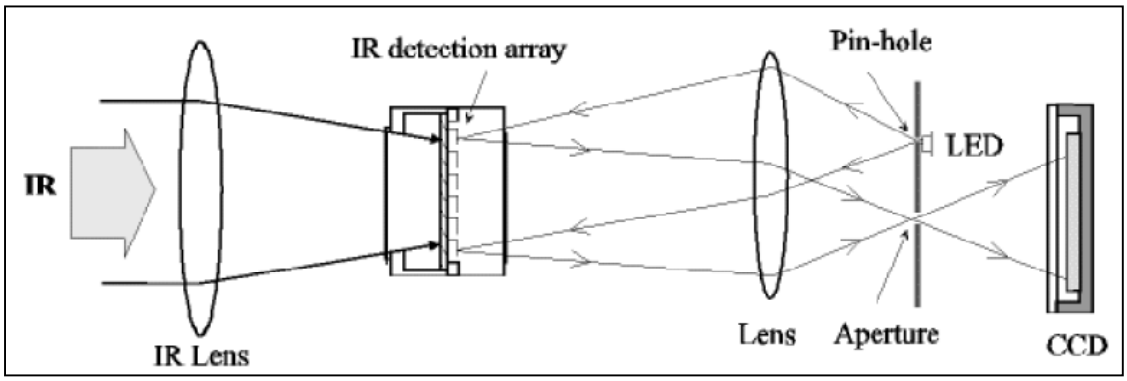

Figure 9. Schematic of an optical readout IR imager design using a CCD camera [47]

Optical readout methods have several compelling advantages over capacitance techniques. First, the lack of a need for any electrical contact to the detector elements allows for extremely high thermal isolation to be achieved because insulating materials can be used. However, it should be noted that capacitance readout methods have been proposed which use a "floating electrode" and therefore do not required electrical connections to the detector element [53]. Another advantage of optical readouts is that the sources of noise on the detector array itself are essentially limited to vibration and thermal fluctuation noise, thereby eliminating the need to consider noise and power consumption associated with on-chip readout integrated circuitry (ROIC) [50]. Leveraging the mature technology of CCDs allows for the use of a component already in high volume production and which is therefore quite inexpensive. By using high performance CCD sensor arrays, imaging speeds for optical readouts of up 1,000 frames per second have been demonstrated [47].

Several researchers [5, 52, 54] have proposed and worked toward a "direct-view" optical readout, whereby a human observer would simply look at the optical reflections of a detector array, essentially replacing the CCD with a human eye. Since no power would be consumed by the detector array, this method would allow for an extremely low powered camera. However, a direct-view system would have no pixel-by-pixel correction or image processing, and would therefore require extremely precise manufacturing, beyond what is currently possible, in order to be practical.

1.4 Polymers in MEMS

Since MEMS was an offshoot of the semiconductor fabrication industry, it initially inherited the traditional substrate material of crystalline silicon and thin films of poly-silicon, oxides, metals, and other ceramics. However, since the 1990s, polymers have been increasingly incorporated into MEMS. Polymers are used for several reasons. First, they allow for much larger degrees of deformation than typical semiconductor materials and have radically different mechanical, optical, and chemical properties. Polymers also allow for a much wider array of deposition and forming processes than other materials. These include casting, molding, LPCVD,

embossing, printing, stamping, and others. Polymers tend to be available at lower costs than other materials, especially when used as a substrate material in place of costly crystalline silicon or quartz. Finally, polymers allow for unique chemical and biological functionalities. Because of their distinctive properties, polymers have been used in many different capacities including as substrate materials, structural and functional thin films, adhesive agents, and for device packaging [55]. For the purposes of this research, their use as structural and functional thin films, especially for use as sensors, is of greatest interest rather than their use in other common applications such as micro-fluidics.

1.4.1 Previous uses in MEMS

The mechanical response of polymer thin films has been used to detect a variety of chemical vapors. Analytes cause the polymer film to swell, inducing a reversible deflection or stress which is detected [56]. The response of polymers to chemical vapors, especially solvent vapors, has also been utilized to measure chemical surface interactions and changes in the mechanical properties of polymer thin films [57].

Commercially available microfabricated cantilevers (typically used for atomic force microscopes and made of silicon) have been coated with polymers using a variety of methods and for a variety of purposes. AFM tips were coated with an ultraviolet (UV) curable polymer in order to act as a radiation dosimeter [58]. In that instance, the nonreversible cross-linking of the polymer led to a change in stress in the cantilever bimorph, which led to a measurable shift in resonant frequency. Similar methods were used to detect relative humidity and mercury vapor [59]. AFM tips have also been functionalized with multilayer depositions in order to detect such analytes as glucose [60] or with a hydrogel for the measurement of cations in an aqueous solution [61] or the pH of a solution [62]. Cantilevered beams made from a spin-coated film of SU-8 have been fabricated and proposed for use as biological sensors [63].

1.4.2 Chitosan and Chitin

Chitin, one of the most common polysaccharides in nature, acts primarily as a structural material for many organisms such as crustaceans, insects, and fungi. It is chemically related to cellulose and has some similar properties such as low solubility and a lack of chemical reactivity. Chitosan is the partially deacetylated derivative of chitin. There is no sharply defined convention for the nomenclature between chitin and chitosan based on the degree of acetylation, but a 50% degree of acetylation is sometimes used as the separating point. Unlike chitin, chitosan is soluble in dilute acids, making it much more easily processed and used in applications where it must be flowed, cast, or made into forms such as fibers. Vast quantities of chitin and chitosan are commercially obtained from the crab and shrimp industries.

Chitin and chitosan have many useful properties such as biocompatibility, non-toxicity, biodegradability, and the ability to absorb heavy metals [64]. For these reasons, chitin has been utilized in a vast variety of applications. Many biomedical applications have been demonstrated [65], notably the use of chitin fibers to promote healing and aid tissue reconstruction in wound dressings and as an agent for drug delivery [66]. Other applications are far too numerous to mention here, but range from cosmetics and textiles [67] to food applications [68] and water

purification [69]. The chemical structures of chitin and chitosan are shown in Fig. 10, below.
Figure 11. Bimorph diagram with cross section and dimensions
Although material properties can vary based on chemical composition and other factors, representative material properties for chitosan and chitin films are provided in Table 1, below.

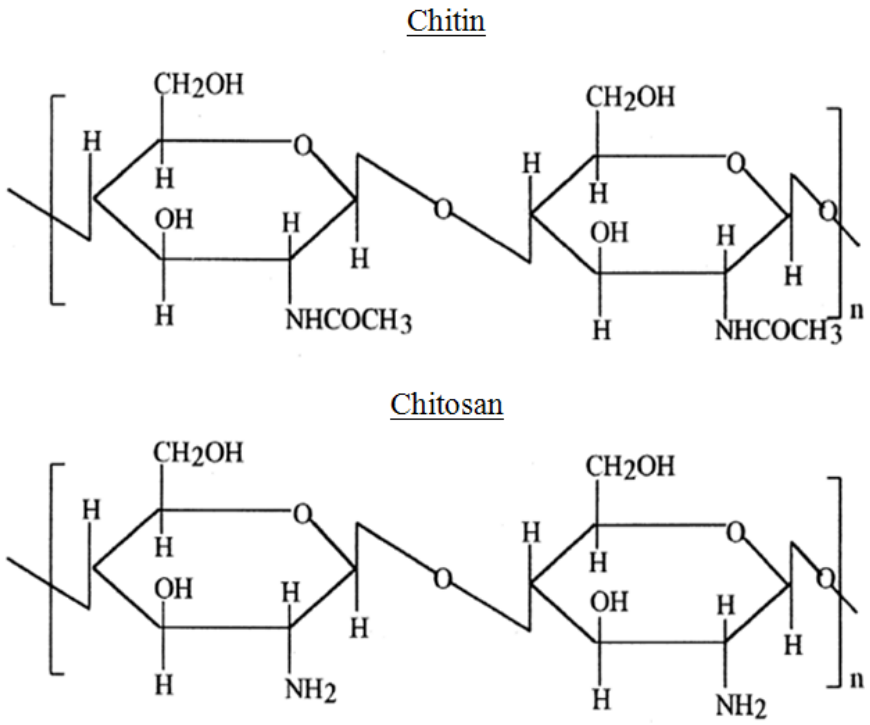

Figure 10. Chemical structures of chitin and chitosan [64]

Of particular interest to this research is the use of chitin in the pit organs of the beetle, *Melanophila acuminata*. These organs act as highly sensitive infrared detectors and allow the beetles to locate freshly burned trees in which to lay their eggs. Although the exact method of transduction is still being debated, it is clear that chitin, which makes up the majority of the sensing bulb, acts as the infrared absorbing material [70]. The beetle is most sensitive to infrared radiation of about 3 μm wavelength, which roughly corresponds to the peak emissive wavelength of forest fires at temperatures of about 425 to 1150 °C [1] and corresponds to one of the absorption peaks of chitin. The absorption characteristics of chitin are shown in Fig. 18, in the next chapter.

Because of the immense interest in the use of chitin and chitosan for the aforementioned variety of practical applications, there is also an interest in incorporating these materials into micro-systems, especially for sensors. Several manufacturing techniques have been attempted using chitosan including nano-imprinting [71], electro-deposition [72], and photolithography using a photo-crosslinkable form of chitosan [73]. The electro-deposition of chitosan on MEMS cantilevers has been used for bio-sensing [74]. However, these fabrication methods impose limitations in resolution, alignment, required substrates, and chemical functionality [70].

Due to its use in a highly sensitive uncooled infrared sensor in beetles, as well as its potential for myriad other uses in microsensors, chitin was selected as a candidate material for the sensors created in the this research. A novel photolithographic process originally developed

by Pisano and Cheng [75] was utilized for this research and will be discussed in depth in Chapter 2.

Property	Value
Young's Modulus	2.3 - 4.2 MPa
Poisson ratio	0.42
Dielectric constant	30
Index of Refraction	1.53
pKA	6.1
Coefficient of Thermal Expansion	$6 \cdot 10^{-5}$ K^{-1}
Thermal conductivity	0.15 $Wm^{-1}K^{-1}$

Table 1. Chitosan / chitin material properties [76]

1.5 Dissertation Organization

The following chapters will describe the design and development of a thermal infrared detector based on polymer bimorph MEMS structures. Chapter 2 describes the theory of thermal bimorphs and the fabrication of polymer bimorphs for this research. Chapter 3 introduces the principles of design of thermal infrared detectors in general, and thermo-mechanical detectors in particular, and also describes the fabrication of sensors. Chapter 4 presents the results of sensor fabrication and describes the testing and evaluation of sensors by both optical and electrical methods. Chapter 5 concludes with a summary of this research and a set of recommendations for future work.

Chapter 2: MEMS Bimorph Structures

Structures composed of two materials with different properties are commonly referred to as being bimorphic or called bimorphs. In MEMS, these structures usually take the form of thin strips or beams. Any bimorph structure which experiences some stimulus promoting unequal strains in the two layers will necessarily bend. This bending has been utilized in sensors and actuators throughout the years in myriad applications [77]. A common example is the bimetallic thermostat, a thin strip composed of two different metals which deflects when experiencing a change in temperature due to the differing coefficients of thermal expansion of the two metals. In addition to temperature changes, stimuli such as chemical reactions, electric or magnetic fields, and light may cause strain mismatches in properly selected materials [78]. These structures may then act as sensors or actuators utilizing a variety of methods, to be discussed later.

When used as thermal infrared sensors, the deflection of bimorphs is caused by interfacial thermal stresses caused by a mismatch in the coefficients of thermal expansion (α) of the two materials. The first microfabricated bimorph beams used as temperature sensors were silicon cantilever beams coated with a thin layer of aluminum and used to measure the energy produced during surface chemical reactions [16].

2.1 Theory of Thermal Bending

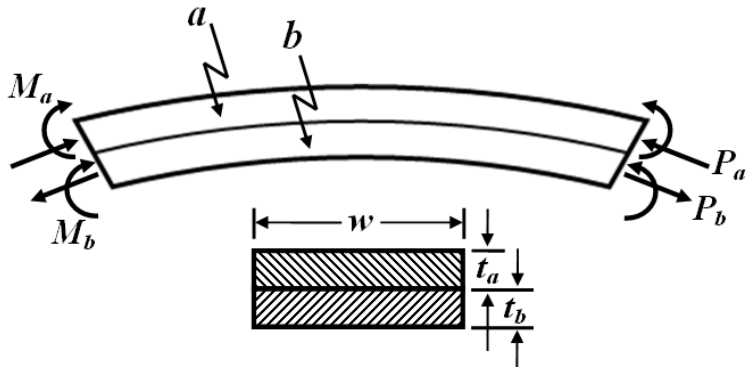

Figure 11. Bimorph diagram with cross section and dimensions

The deflection of a bimorph beam was first formally analyzed in 1925 by Timoshenko who applied the analysis to bi-metal thermostats [79]. An equation for the thermally induced deflection can be derived based on energy minimization [80] or balancing forces. The Timoshenko formulation, however, neglects the effect of the transverse bending moment. This important effect will be accounted for by a subsequent analysis in this chapter.

Following Timoshenko's original derivation, we examine a bimorph strip with length much greater than width and undergoing a temperature change, ΔT. Given that the top layer has a coefficient of thermal expansion, α_a, greater than that of the bottom layer, α_b, it will deflect as shown in Fig. 11, above. We assume original planar cross sections in the unbent bimorph remain planar and become perpendicular to the curved axis upon bending. We also assume uniform

heating, isotropic expansion, no yielding, and constant material properties. For any section taken within the beam, the internal forces and moments acting on each layer can be represented as shown in Fig. 11. Lacking any external moments or forces, we can sum forces to find:

$$P_a = P_b = P \tag{23}$$

Summing moments yields:

$$\frac{Pt_a}{2} + \frac{Pt_b}{2} = M_a + M_b \tag{24}$$

With E as the Young's modulus of each respective layer, I the moment of inertia, and ρ the radius of curvature of the entire beam we have:

$$M_a = \frac{E_a I_a}{\rho} \qquad M_b = \frac{E_b I_b}{\rho} \tag{25}$$

Since the moment of inertia for each layer is given by Eq. (26), below, combining Eqs. (24) and (25) leads to Eq. (27), below:

$$I = \frac{wt^3}{12} \tag{26}$$

$$\frac{P(t_a + t_b)}{2} = \frac{E_a w_a t_a^3}{12\rho} + \frac{E_b w_b t_b^3}{12\rho} \tag{27}$$

We assume perfect bonding between the layers and therefore let a boundary condition be the equality of strain in each layer at the interface. We can therefore write:

$$\alpha_a \Delta T + \frac{P}{E_a t_a w_a} + \frac{t_a}{2\rho} = \alpha_b \Delta T - \frac{P}{E_b t_b w_b} - \frac{t_b}{2\rho} \tag{28}$$

If a bimorph beam of length L is cantilevered, the free end will deflect due to the curling of the beam. By assuming the vertical tip deflection, y, is small relative to the radius of curvature, we can relate the radius of curvature to the tip deflection:

$$y = \frac{L^2}{2\rho} \tag{29}$$

Finally, by solving for P in Eq. (27) and substituting into Eq. (28), we arrive at an expression for the tip deflection of the bimorph:

$$y = \frac{3L^2\Delta T(\alpha_a - \alpha_b)(t_a + t_b)}{\left[\frac{E_b t_b^3}{E_a t_a} + \frac{E_a t_a^3}{E_b t_b} + 6t_a t_b + 4t_a^2 + 4t_b^2\right]} \tag{30}$$

This is the original bimorph equation from Timoshenko [79] and utilized by a number of researchers [46, 81]. It is interesting to note that Eq. (30) reduces to a form of the Stoney equation, Eq. (34) below, when one layer is much thinner than the other. However, this result neglected the transverse bending moment, assuming it to be insignificant for narrow beams. Subsequent study revealed that, even for the narrow beams typical of MEMS structures, this transverse bending moment is significant and should be accounted for by including the influence of the Poisson's ratio, ν, of each material. Neglecting the role of Poisson's ratio has been documented to result in errors as large as 50% for representative MEMS structures [82]. It is therefore more appropriate to use the bi-axial modulus of each material, given by:

$$E' = \frac{E}{(1-\nu)} \tag{31}$$

Substituting the bi-axial modulus into Eq. (30) yields the final form of the thermal deflection equation for a bimorph beam:

$$y = \frac{3L^2\Delta T(\alpha_a - \alpha_b)(t_a + t_b)}{\left[\frac{E_b' t_b^3}{E_a' t_a} + \frac{E_a' t_a^3}{E_b' t_b} + 6t_a t_b + 4t_a^2 + 4t_b^2\right]} \tag{32}$$

This equation was utilized for the purposes of this research, and has been shown to be in close agreement with finite element models for a wide variety of designs [82, 83]. For convenience, Eq. (30) can also be rewritten to predict the radius of curvature of a beam so that:

$$\frac{1}{\rho} = \frac{6\Delta T(\alpha_a - \alpha_b)(t_a + t_b)}{\left[\frac{E_b' t_b^3}{E_a' t_a} + \frac{E_a' t_a^3}{E_b' t_b} + 6t_a t_b + 4t_a^2 + 4t_b^2\right]} \tag{33}$$

Optimization of the thermo-mechanical response and selection of layer thicknesses for bimorphs will be discussed in Chapter 3.

2.2 Residual Stress

Residual stresses are stresses which remain in a material or body after manufacturing and processing in the absence of external forces or thermal gradients [84]. Residual stresses in thin films have been studied for over a century [85] and frequently affect the design, performance, reliability, and manufacturing of MEMS devices. These stresses and their affects are usually undesirable but arise naturally in thin films from their deposition or growth processes by way of a variety of mechanisms [86].

With respect to MEMS bimorph structures, residual stresses often lead to undesired deformations. If a film with residual stress is applied to a substrate and the substrate is allowed to deform, the resulting composite structure will curl. Besides curling, residual stress can result in cracking of the film or delamination from the substrate. Even a structure made from a single layer of a material can exhibit curling if the residual stress is not uniform over the cross section of the structure, as is frequently the case.

The residual stress in a thin film, σ_f, coating a relatively thick substrate is described by the Stoney [85] equation:

$$\sigma_f = \left(\frac{E_s}{1-\nu_s}\right)\frac{t_s^2}{6\rho t_f} \tag{34}$$

where $E_s$is the Young's modulus of the substrate, $\nu_s$is the Poisson's ratio of the substrate, t_s and t_f are the thicknesses of the substrate and the thin film, and ρ is the radius of curvature of the structure. The Stoney equation assumes isotropic and uniform stress in the thin film, no initial curvature of the substrate, and elastic deformations. It is frequently utilized along with an optical profilometer to measure the stress in thin films. Many variations of the Stoney equation have been developed to account for factors such as anisotropic substrates [87].

For bimorph cantilever beams, a mismatch in residual stress will lead to curling of the beam. An equation predicting the initial curvature of the beam can be derived in a similar manner to Eq. (33) above, the equation for thermal deflection [77]. It is given by:

$$\frac{1}{\rho_{initial}} = \frac{6(\varepsilon_a^* - \varepsilon_b^*)(t_a + t_b)}{\left[\frac{E_b' t_b^3}{E_a' t_a} + \frac{E_a' t_a^3}{E_b' t_b} + 6t_a t_b + 4t_a^2 + 4t_b^2\right]} \tag{35}$$

where the residual strain of a layer, ε^*, due to its residual stress, σ^*, is defined as:

$$\varepsilon^* = \frac{\sigma^*}{E'} \tag{36}$$

For a MEMS bimorph used as a thermo-mechanical detector, there will be an initial curvature, ρ_i, from the residual stress and a curvature, ρ_t, imposed by any change in temperature. It can be easily shown that these deformations superimpose such that:

$$\frac{1}{\rho} = \frac{1}{\rho_i} + \frac{1}{\rho_t} \tag{37}$$

where ρ is the actual deflection of the beam. The implications of residual stress on the design of thermo-mechanical bimorph detectors will be discussed in Chapter 3.

2.3 Material Selection

Since the thermal deflection sensitivity is strongly dependent on the difference in coefficients of thermal expansion (α) of the two materials in a bimorph, materials should be chosen in order to maximize this difference. In the past, the low α material was usually a ceramic such as silicon, silicon carbide, or silicon nitride.[88] The high α material was almost always a metal, commonly aluminum or gold [42]. However, restricting design to these materials limits mismatch in α to less than 30 ppm/K.

The use of polymers allows for a dramatically higher difference in coefficients of thermal expansion, leading to higher thermal deflection sensitivities. A table of the coefficients of thermal expansion of several materials commonly used in MEMS is provided below. In addition to having high coefficients of thermal expansion, polymers are interesting materials for use as infrared sensors because they exhibit strong absorption of infrared light. This absorption is associated with the vibrational resonance of their organic chemical bonds. The strength of the bond, mass of the atoms, and mode of vibration all effect absorption. Absorption in polymers can also be associated with morphological changes, crystalline rearrangements, and other effects. Therefore, the particular pattern of light absorption as a function of frequency is a trait of individual polymers and can be advantageously utilized in the design of thermal infrared sensors. By using multiple polymers, or functionalizing or altering different regions of a single polymer, an array of sensors with differing wavelength sensitivities would be achievable. A camera that is able to simultaneously image multiple wavelength bands has been a recognized goal in the literature [5] and may be achieved by using polymer-ceramic bimorphs.

However, polymers have received little attention for use in thermal bimorphs due to the perception of polymers as having inferior mechanical strength and poor adhesion to many materials. Many polymers absorb water and change properties drastically with changes in temperature. They are also sensitive to subsequent processing steps and temperatures and known to exhibit stresses which can damage many MEMS structures. Past researchers have utilized metals instead of polymers for lack of having a solution to the problems caused by residual stress [42].

Recently, the high thermal sensitivity of microfabricated polymer bimorph beams has been experimentally verified by coating one side of AFM cantilevers with plasma-polymerized polystyrene via PECVD. The temperature resolution of these bimorphs was reported by LeMieux *et al*. to be as low as 0.2 mK based on a deflection of 2 nm/mK for a 300 μm long cantilever [89]. This thermal sensitivity was more than 30 times that of a similar gold-silicon cantilever. However, with further optimization of material selection and geometry, and the incorporation of features which enhance layer adhesion and bending response [37, 90] it is reasonable to conjecture that thermal sensitivities of more than 100 times that of simple gold-silicon cantilevers may be achieved. The polymer coated cantilevers also showed good repeatability even when deflected up to 50 μm. Later, conventional metal coated silicon nitride AFM cantilevers were coated with nano-particle composite polymers in order increase the mechanical strength of the polymer layer. The surfaces of the uncoated cantilevers were also modified in order to promote adhesion of the polymer composite and strain transfer. However, these structures were unable to reach the thermal sensitivities of the simpler polymer on silicon beams [91]. These same researchers fabricated a simple bimorph composed of ZnO and plasma-polymerized benzonitrile for use as a temperature sensor and switch [92]. This device relied on the change in electrical contact resistance as the bimorph deformed into the substrate.

These previous efforts at producing MEMS bimorphs with polymers generally do not lend themselves to high volume production or integration with other MEMS systems or CMOS because they relied on pre-fabricated structures such as AFM tips and were not part of a batch process. Ideally, polymer bimorph fabrication techniques would be performed using common batch processing manufacturing processes and compatible with a variety of CMOS integrated substrates.

Material	(10^{-6}/K) at 300 K
Silicon Dioxide (SiO_2)	0.4 – 0.6
Silicon Carbide	3.9 – 4.0
Silicon	2.6 – 3.3
Silicon Nitride (Si_3N_4)	2.8 – 3.2
Titanium	8.4 – 8.6
Gold	14
Aluminum	23
Chitosan	~45
Photoresists	~50
PMMA	~70
Silicon Elastomers	30 - 300

Table 2. Coefficients of thermal expansion for selected ceramics, metals, and polymers

Residual Stress in Thin Film Polymers

Polymer films are typically deposited on a substrate as liquids and converted to solids by the evaporation of a solvent, a chemical reaction, or a phase separation. Most polymer coatings shrink during these processes but the strain is constrained by adhesion to the substrate and stress therefore develops in the plane of the film [93]. The amount of stress in polymer thin films can vary over time and due to subsequent processing.

Processing steps, including drying rates and the chemistry of the deposition, are frequently varied in order to minimize residual stress. As with other materials such as semiconductors [94], polymer thin films may be exposed to thermal cycling in order to promote molecular motion and provide stress relaxation. However, due to the nature of polymer deposition, it is difficult to entirely eliminate residual stress from these films and the repeatability in the level of residual stress of any process can be problematic. Therefore, MEMS devices relying on the precise control of, or the minimization of, residual stress in thin films polymers will face severe difficulties. Ideal designs will be insensitive to residual stress.

2.4 Fabrication

Microfabrication processes were developed and demonstrated for three different polymers in order to compare the results for their application toward bimorph MEMS devices.

All three processes utilize a sacrificial layer of silicon dioxide (SiO_2) in order to create cantilevered structures. These processes may serve as a template for processes incorporating other polymers, alternative structural layers, or other modifications. Fabrication was performed in the Microfabrication Laboratory at the University of California, Berkeley.

2.4.1 Photoresist

The first polymer employed in this research for the creation of microfabricated bimorphs was photoresist due to its ability to be directly patterned through photolithography. Photoresist is the most commonly employed polymer in all of microfabrication and is used broadly throughout the semiconductor industry to transfer patterns from optical masks onto thin films. Although many types of photoresist are available, Fuji Film OCG-825 (G-line) positive photoresist was selected for the purposes of this research. Due to its complicated chemistry, photoresist tends to exhibit absorption over a broad range of frequencies. The FTIR absorption spectrum for OCG 825 photoresist is shown in Fig. 12, below.

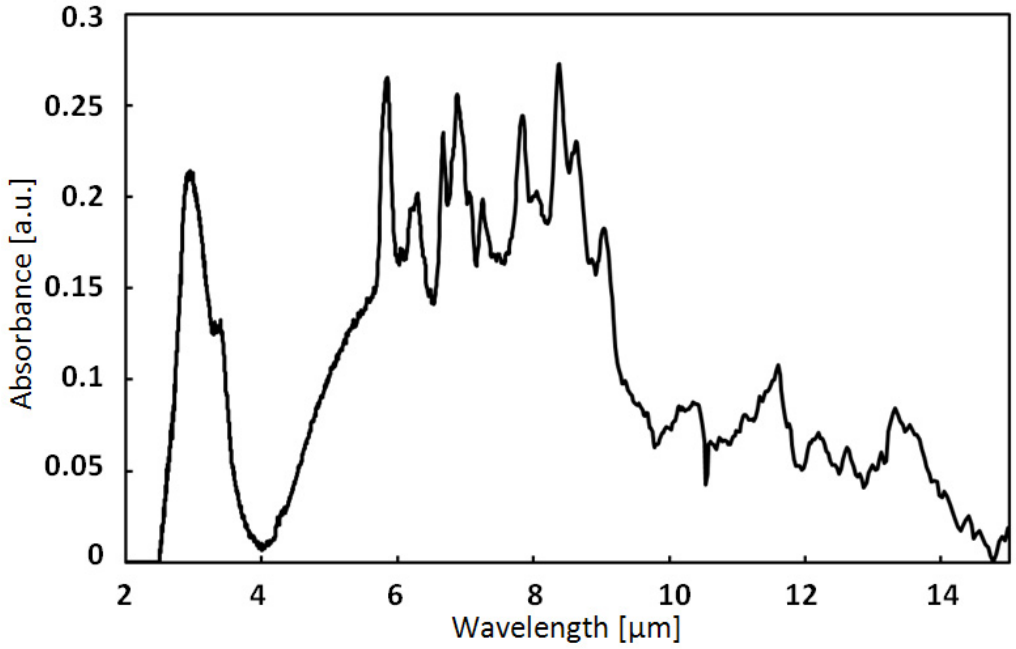

Figure 12. FTIR absorption spectrum of OCG-825 G-line photoresist

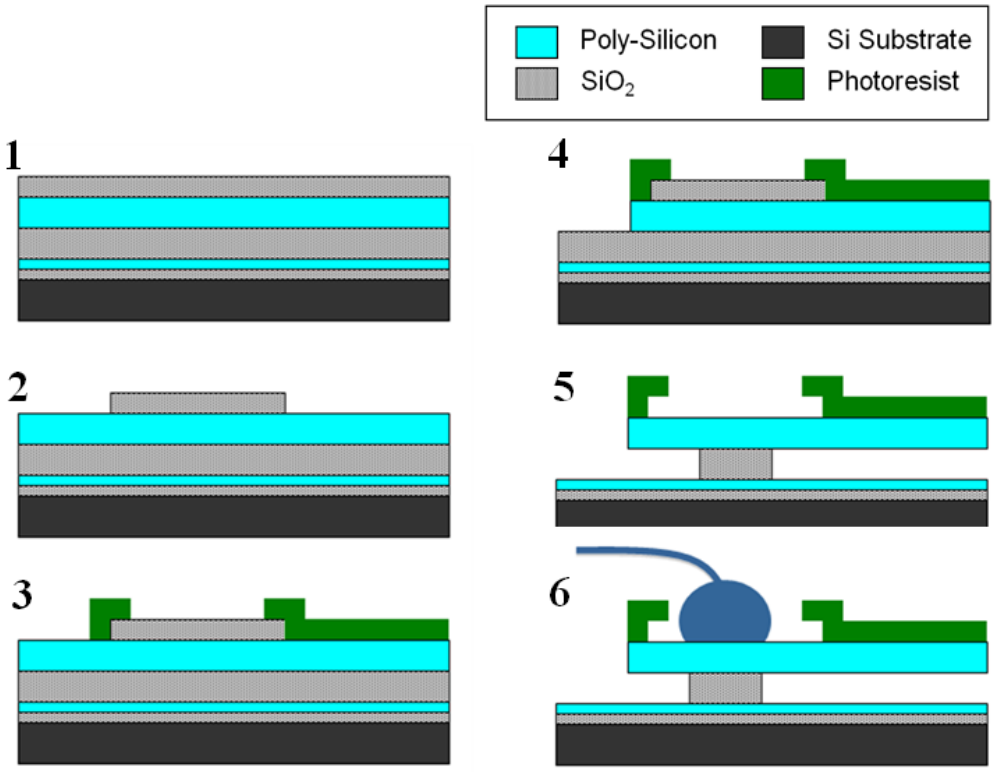

Figure 13. Photoresist bimorph process flow

A schematic of the photoresist bimorph fabrication process is presented in Fig. 13, above. Each step is described in detailed below.

1. Starting with a new silicon wafer as a substrate, alternating layers of silicon dioxide (low temperature oxide) and highly-doped poly-crystalline silicon are deposited by low pressure chemical vapor deposition (LPCVD). LPCVD steps were performed in Tystar furnaces. The first layer of oxide acts to electrically isolate the bottom layer of poly-Si, which will act as the bottom electrode of the variable gap capacitor, from the substrate. Alternatively, these two layers can be omitted if a heavily doped silicon wafer is used as the initial substrate, or the bimorph will be used with an optical readout method. The third deposited layer is the sacrificial oxide layer. Its thickness will define the thickness of the initial gap between the base of the bimorph cantilever and the bottom electrode. Another layer of highly-doped poly-crystalline silicon is deposited. This layer will act as the bottom layer of the bimorph structure. Finally, a top layer of oxide is deposited.

2. Once the layers have been deposited, the top oxide layer is patterned using standard photolithography and etched by CF_4 plasma. This patterned area will act as a hard mask and define the area used for wirebonding. For all photolithography steps, a 10x reduction stepper was used (CGA-6200) to create an 8 by 8 array of dies. Before spin casting the photoresist, wafers are dried and treated with a vapor of hexamethyldisilazane (HMDS) in order to promote adhesion of the photoresist.

3. Next, photoresist is spun cast at 5000 rpm and pre-baked at 90 °C for one minute. The photoresist is then patterned by exposure to ultraviolet light to define the bimorph regions. The wafer is hard baked at 120 °C for 45 minutes in order in stabilize the photoresist film and improve its etch selectivity.

4. The structural poly-Si layer is etched using chlorine (Cl_2) plasma. The wafer is then covered with a low-tack tape to protect it from damage during wafer dicing, which is performed using an automated dicing saw (Esec 8003). The use of tape for this application is discussed in depth at the end of this section.

5. The bimorph structure is then released by isotropically etching away the oxide by exposure to hydrofluoric acid (HF) vapor in a reaction vessel (Idonus HF VPE-100). Dies are attached to a silicon wafer with cool-grease and the wafer is held in place using an electrostatic clamp. The substrate is maintained at 43 °C during the release on a temperature controlled chuck in order to mitigate water condensation which would lead to sticking. This etching step also removes the top oxide hard mask, revealing an area of poly-Si not coated with photoresist. The etch is timed such that a layer of oxide remains under the bond pad and acts to electrically isolate the beam structure and bond pad from the substrate. The HF fluid reservoir is maintained at 31 °C.

6. Finally, an ultrasonic wire bonder (West Bond 7400B) is used to attach an aluminum wire to the uncoated poly-Si bond pad for electrical testing.

2.4.2 Chitosan

It has been documented that chitosan thin films are highly sensitive to changes in relative humidity [95]. Absorption of moisture is associated with swelling and affects the level of intrinsic stress in these films. However, chitin films display much greater stability with respect to changes in relative humidity. For this reason, chitosan bimorphs are less appropriate for use in this research than chitin bimorphs. However, since many other applications may use the unique properties of chitosan films [96] and a chitosan process can be used as a basis for a chitin process, the development of a chitosan bimorph process was useful to this research.

The fabrication process for chitosan bimorphs is more complicated than the photoresist process because chitosan cannot be directly patterned by exposure to light without severe chemical alternations, reduced functionality, and highly limited photolithographic resolution due to hydrogel swelling [73]. The process follows the work of Cheng and Pisano [70, 75], who first developed a chitosan photolithographic process for this research. A solution of chitosan suitable for spin casting was created by dissolving purified medium molecular weight (average 250 kDA) chitosan into a solution of acetic acid, buffered by deionized water, while heating to 40 °C. Solutions with chitosan concentrations of about 0.66% to 4.0% w/v were prepared. Particles were removed from the solution by vacuum filtration through 5 μm pored filters. Two separate processes were developed to create chitosan bimorphs and are detailed below.

"Wet" Chitosan Process

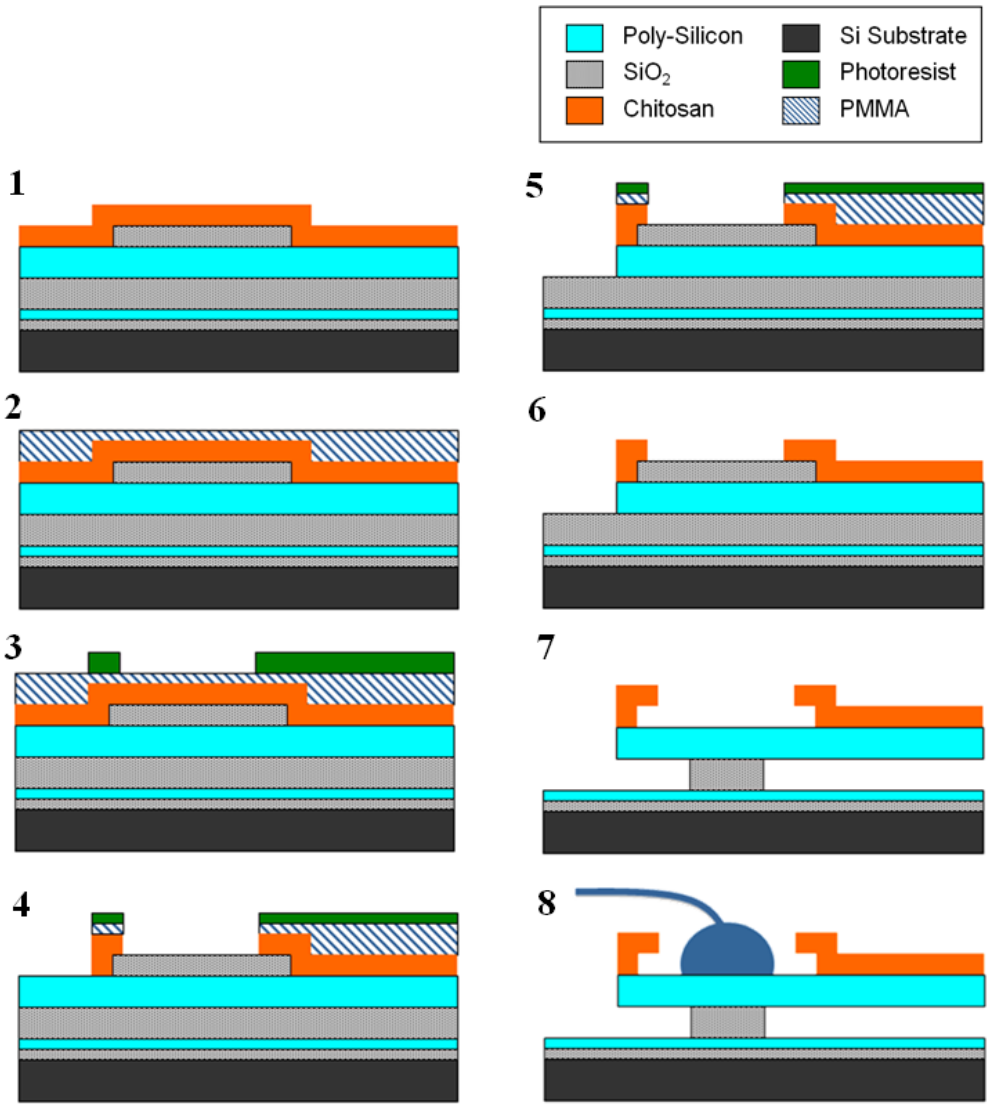

Figure 14. Chitosan bimorph process flow

A schematic flow of the "wet" chitosan bimorph fabrication process is presented in Fig. 14, above. Each step is described in detailed below.

1. The same initial layers are deposited via LPCVD as in the photoresist bimorph process. The top layer of oxide is patterned using standard photolithography and etched by CF_4 plasma. The thickness of the chitosan layer may be controlled by modulating the spin speed and viscosity of the chitosan solution. The chitosan and acetic acid solution is spun onto the wafer and baked at 95 °C for 5 minutes on a hotplate in order to evaporate the acetic acid. After the initial bake the hotplate is turned off and the chitosan coated wafer is left on the hotplate for 10 minutes in order to allow the chitosan layer to cool slowly.

2. In order to protect the chitosan film from swelling and exposure to solvents, a layer of polymethyl methacrylate (PMMA) is spun onto the chitosan layer and baked at 95 °C for 5 minutes. 495 C5 PMMA from MicroChem was chosen due to its viscosity.

   Next, photoresist is spun on top of the PMMA film and patterned using standard photolithography. Any contact between the photoresist developer and the chitosan film was observed to result in cracking and swelling of the chitosan film. Therefore, complete coverage by the PMMA layer is important.

3. The PMMA and chitosan are now etched using an anisotropic oxygen plasma reactive-ion etch in a parallel plate plasma etching system (Plasma-Therm PK-12 RIE). Due to the selectivity of the etch (observed to be about 1:1.65 for chitosan to photoresist), the photoresist layer is eroded but not completely etched away during this process.

4. Using the same layer of photoresist as a mask, the structural poly-Si layer is now etched using a 90% SF_6 10% O_2 plasma, also in the PK-12 RIE.

5. The photoresist and PMMA layers are now stripped in a bath of 80 °C PRS-3000 stripper (J.T. Baker) and briefly rinsed using deionized water. This step requires precise timing, is difficult to reliably repeat, and was found to lead to high levels of residual stress in the chitosan film. Therefore, an alternative process was developed and is described below.

6. Release of the bimorph structures is performed in the same way as in the photoresist bimorph process, using timed exposure to HF vapor.

7. Finally, an aluminum wire bond is attached to the anchor.

"Dry" Chitosan Process

As noted earlier, the removal of photoresist and PMMA from atop the film of chitosan (performed by PRS-3000 followed by a deionized water rinse) was difficult to repeat and was observed to cause high levels of residual stress in the chitosan film. In order to address these issues, a "dry" chitosan process was developed in which an anisotropic oxygen plasma reactive-ion etch was used to remove the photoresist and PMMA. Although requiring proper timing, this process resulted in lower levels of residual stress and was found to exhibit greater repeatability. All other steps in the process remained the same as in the "wet" chitosan process above.

2.4.3 Chitin

The chitin bimorph process follows the chitosan bimorph process, as previously described. However, since chitin is not readily soluble and therefore cannot be deposited by spin casting, a film of chitosan is deposited via spin casting and then converted to chitin by reacetylation (between steps 1 and 2 in Fig. 14, above). The chitosan film is converted to chitin by reacetylation, following the work of East and Qin [97], by immersion in a bath of 5% acetic

anhydride in methanol at 40 °C for 2 hours. Following conversion, the film is rinsed with deionized water and dried.

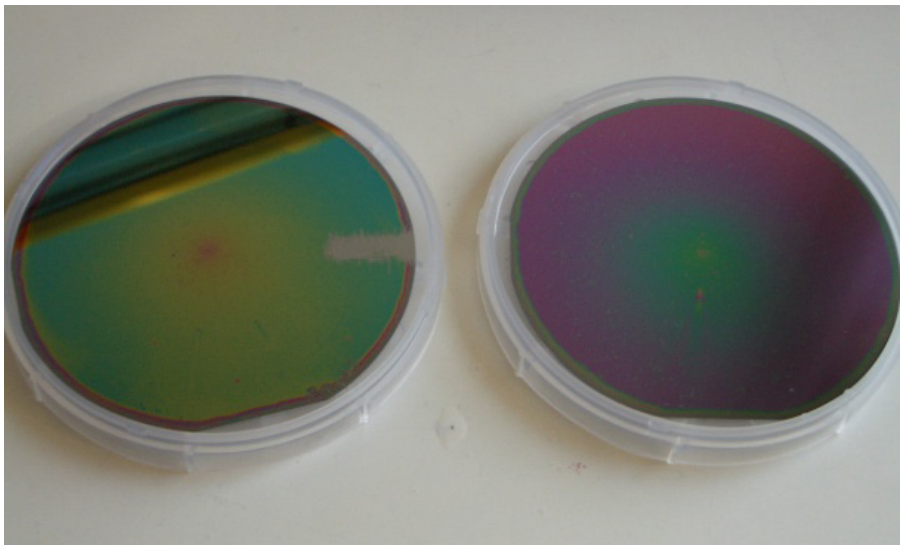

Figure 15. Photograph of silicon wafers coated with chitin (left) and chitosan (right)

2.4.4 Discussion

The use of polymers as functional and structural components in MEMS systems requires special considerations and processing. This section discusses the protection of the polymer layers during wafer dicing and the issues relating to the HF vapor release of the final structures.

Wafer Dicing

In order to prevent damage to released microstructures, wafer dicing was performed prior to the final release of the sacrificial oxide. From a manufacturing perspective, dicing before the final release can greatly increase the cost per die since the final steps cannot be done as a batch, or wafer level, process. There are a variety of strategies for dicing released structures, such as bonded caps or covers, that are employed in industry [98] but were not pursued in this research.

During wafer dicing, it is necessary to protect the functional surface of the wafer from contamination and damage due to water jets and particles generated during the dicing. A frequently employed [99, 100] strategy is to utilize a layer of protective photoresist, which is subsequently stripped away using acetone or photoresist stripper. However, this method presents a problem for polymer coated MEMS since the functional polymers may be affected or removed by the removal of the protective photoresist layer. A process utilizing a layer of protective photoresist was attempted for use in the fabrication of photoresist and chitosan bimorphs. For the photoresist process, the protective layer was not treated with a hard baking step, and was therefore dissolved more easily by photo resist stripper. A 60 second timed immersion in photoresist stripper (PRS-3000) at 80 °C, followed by a rinse with de-ionized water was found to be effective in removing only the protective photoresist and leaving the hard baked photoresist on the bimorph beams. However, this process was difficult to repeat and frequently led to

removal of all photoresist, incomplete removal of the protective photoresist or delamination from the substrate. A scanning electron micrograph illustrating the incomplete removal of photoresist from unreleased chitosan beams is provided in Fig. 16, below. For the chitosan process, a similar process was attempted but resulted in severe swelling of the chitosan layer or delamination.

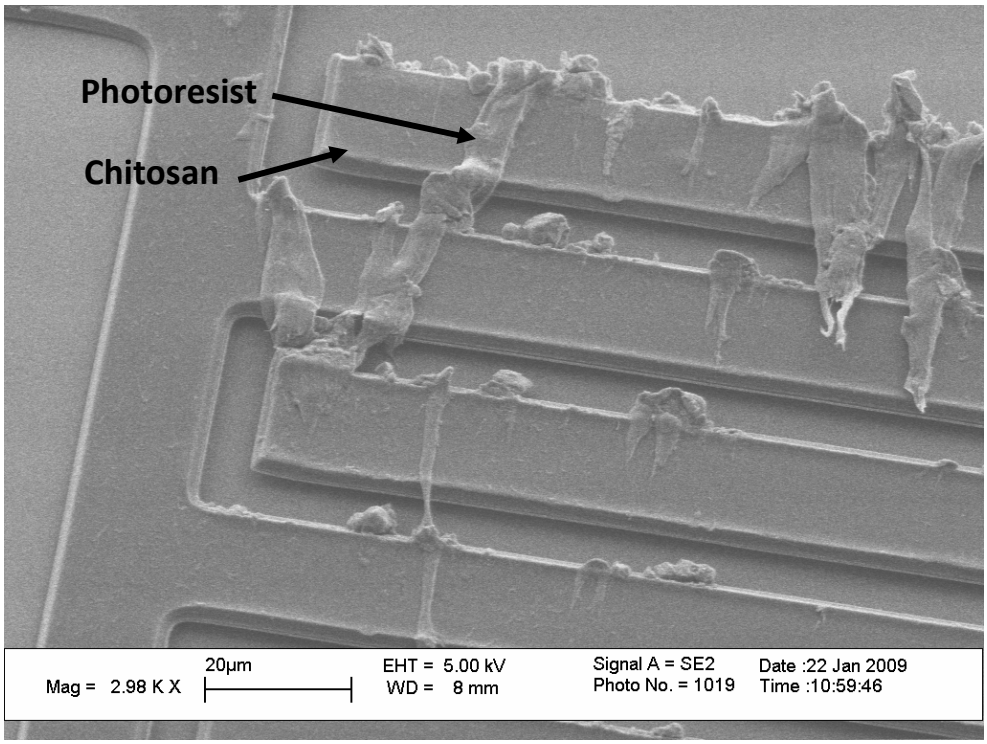

Figure 16. Incomplete removal of photoresist from unreleased chitosan beams

In order to circumvent these difficulties, the protective photoresist layer was replaced by a layer of low-tack adhesive tape. The tape employed was a blue dicing tape usually used to attach the back side of a wafer to the chuck used during dicing. The tape was applied to both the front and back of the wafer by applying light pressure with a roller, attempting to avoid the formation of air bubbles under the tape. The wafer was then diced and the tape gently removed from individual dies using tweezers. Two possible issues were the removal of the polymer layer during tape removal or deposition of residual adhesive from the tape. Careful inspection of dies was performed in order to assess the feasibility of this process. Microscope images of devices before and after dicing and tape removal were compared to ensure preservation of the polymer pattern. In addition, a stylus profilometer (Alpha-Step IQ) was used to compare the profiles of the polymer patterns. The removed tape was also examined for any traces of material which had been removed and remained attached to the tape.

An example of one such image is provided in Fig. 17, below, in which the impression from an array of cantilevers extending from a bond pad is shown. No material from the die was present on the tape. Irregularities in the adhesive on the tape occur in the topologically lower areas surrounding the device. These patterns are probably a result of the lower height of those areas since they were likely not smoothed by the roller during application of the tape to the wafer. No residual adhesive was detected on the die itself.

Overall, results of the tape removal were highly favorable and repeatable. Whether the tape remained on the dies for hours or months did not affect the integrity of the resulting die. However, with some chitosan samples, the tape was observed to remove chitosan, but only from non-functional, bulk areas of the film. The patterned areas of chitosan exhibited adequate adhesion to withstand the tape removal. Chitin was observed to exhibit similar adhesion properties as chitosan.

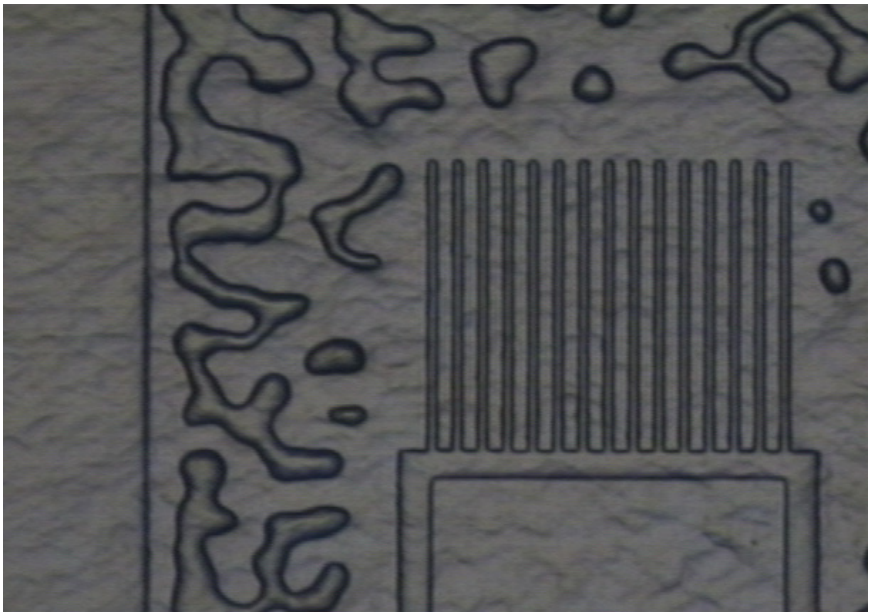

Figure 17. Microscope image of protective tape after removal from die

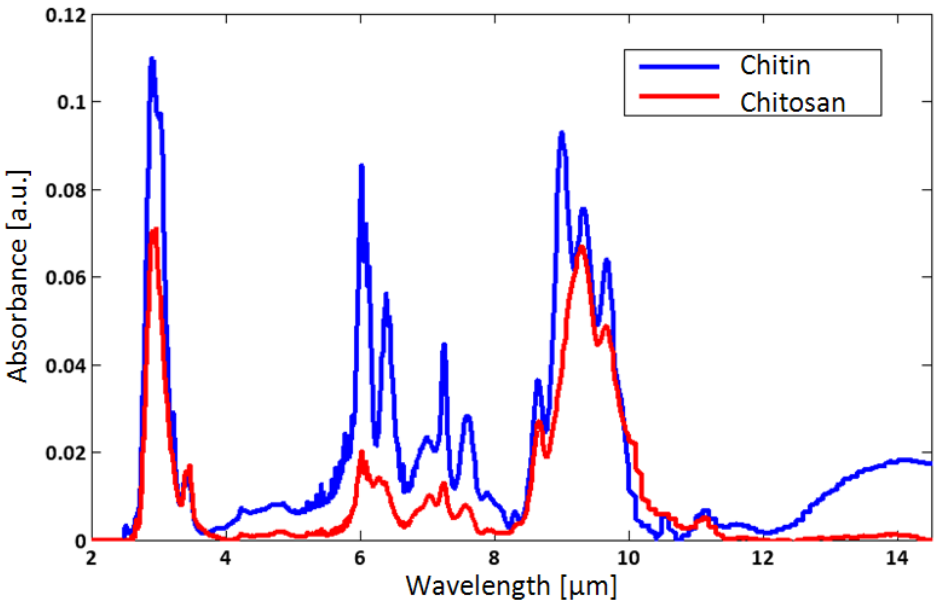

Figure 18. FTIR spectrograph of chitin and chitosan films on a silicon reference

Chitosan Reacetylation

FTIR measurements were made in order to measure the change in the degree of acetylation of chitosan thin films during the chitin bimorph process and are shown in Fig. 18, above. Degrees of acetylation were determined according to the ratio of absorption peaks according to the methods of Zhang *et al.* [101]. The degree of acetylation of the spin-casted chitosan films was about 20% while the degree of acetylation of the films after the reacetylation bath was approximately 58%. A higher degree of acetylation would likely be achieved for longer immersion duration and higher temperatures during reacetylation. Higher degrees of acetylation are associated with reduced solubility. Therefore, chitin films with higher degrees of acetylation may more compatible with the "wet" chitosan process.

2.5 Results of Fabrication

In order to demonstrate the feasibility of these polymer MEMS bimorph processes, poly-crystalline silicon cantilever coated with photoresist, chitosan, and chitin were fabricated. Beams of various dimensions were fabricated with lengths ranging from 50 to 300 μm and widths of 2 to 20 μm. Scanning electron microscope (SEM) images were taken in a Leo 1550 SEM. Structures were sputtered with a thin layer of gold–palladium prior to imaging. The results for each polymer are presented in this section.

2.5.1 Photoresist

SEM images showing bimorph beams composed of OCG-825 photoresist on poly-silicon are presented below. The tip of a cantilevered beam with about 1.25 μm of photoresist on approximately 0.25 μm of poly-Si is shown in Fig. 19, below. A slight apparent shrinking of the photoresist layer is evident and is consistent with the observed presence of tensile residual stresses.

The thickness of the polymer layer was controlled by either the conditions of the spin-casting, such as the solution viscosity and spin speed, or by reducing the deposited thickness by oxygen plasma etching. A bimorph beam with photoresist thickness reduced by etching to a near optimal ratio with the poly-silicon layer is shown in Fig. 20, below. Here the poly-silicon is about 0.25 μm thick and the photoresist is about 0.35 μm thick.

Two interdigitated arrays of beams are shown in Fig. 21. These beams are 300 μm long and 10 μm wide with about 1.5 μm of photoresist on ~0.45 μm of poly-Si . The beams are curled away from the substrate due to the residual stress in the photoresist. The observed radius of curvature is about 250 μm, which corresponds with model projections for a residual stress of approximately 10 MPa in the photoresist layer. The beams are attached to long rectangular regions which act as anchors and pads for wire bonding. The consistency of the curvature of the beams across the array is an indication of constant dimensions and levels of residual stress in the layers in the area of these arrays.

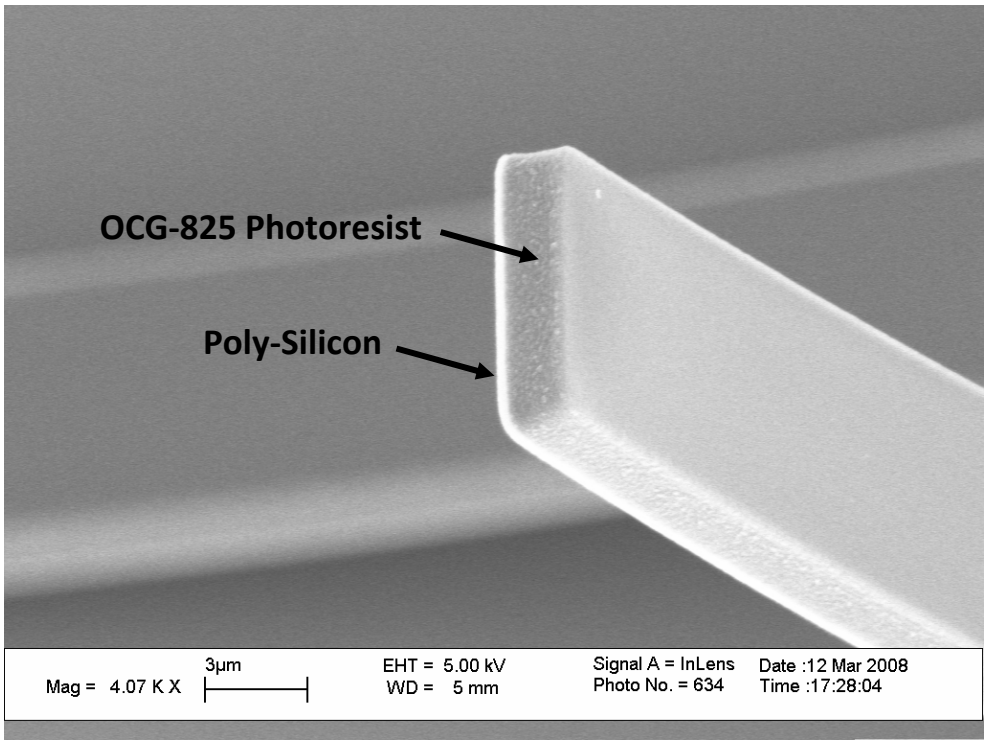

Figure 19. Tip of bimorph cantilever beam composed of OCG-825 photoresist on poly-Si

2.5.2 Chitosan

Chitosan bimorphs were successfully fabricated. However, as expected, these beams exhibited strong deformation in response to changes in relative humidity. This sensitivity was observed through changes in the radius of curvature of bimorph beams. Samples put into the SEM for imaging were dried and subjected to a very low pressure environment. These conditions were observed to lead to severe curling of chitosan bimorph beams, as shown in Fig. 22, below. These beams, composed of about 1.75 µm of chitosan on about 0.35 µm of poly-Si, reached a radius of curvature of about 25 µm. However, the degree of curvature of these beams in ambient conditions was significantly smaller. A comparison of chitosan beams from the same sample in ambient conditions (left) and in the SEM chamber (right) is shown in Fig. 23. In the ambient image, the tips of the beams are out of focus since they extend away from the focal plane of the microscope, but display moderate levels of curling compared to the beams in the SEM chamber.

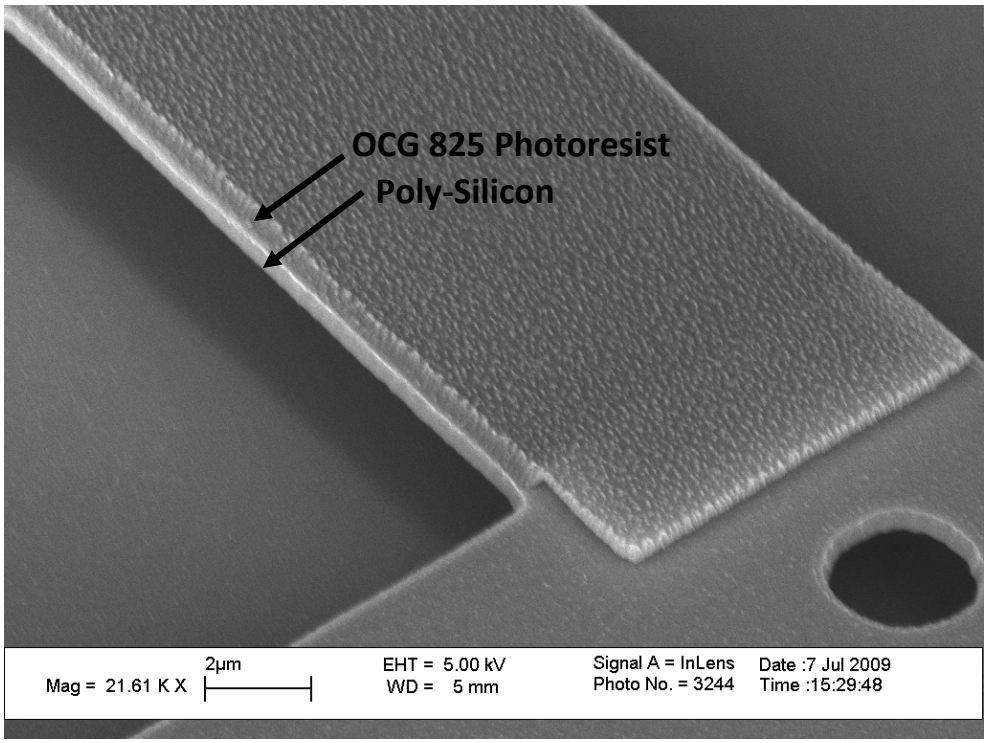

Figure 20. Bimorph beam with optimized photoresist layer thickness

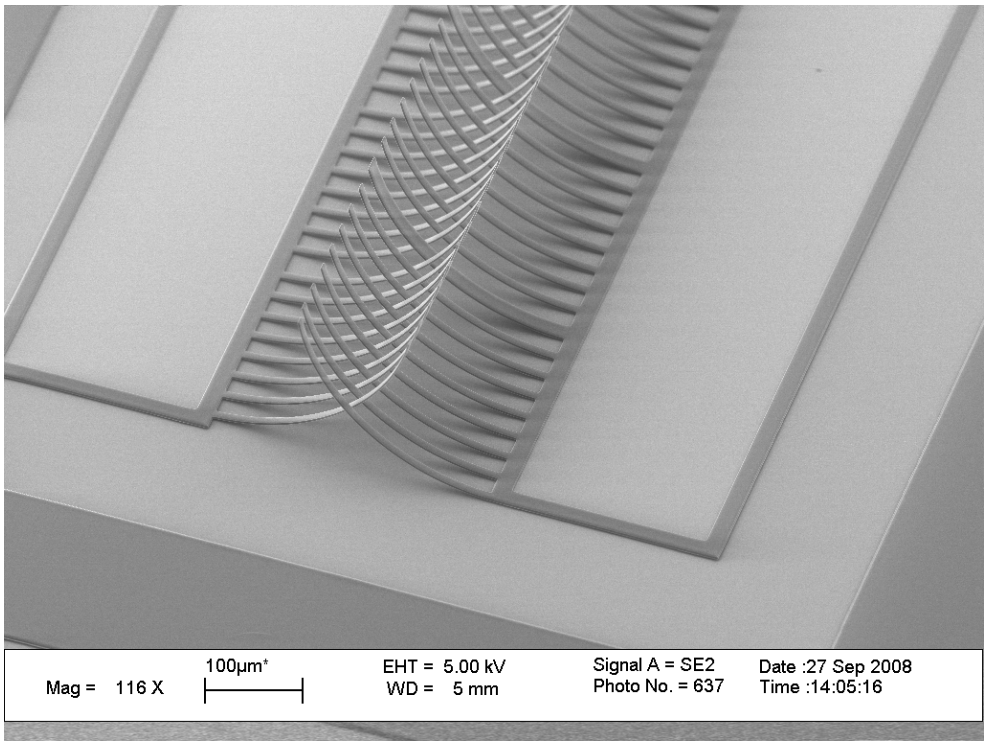

Figure 21. Interdigitated arrays of photoresist bimorph beams connected to large poly-si wire bonding pads

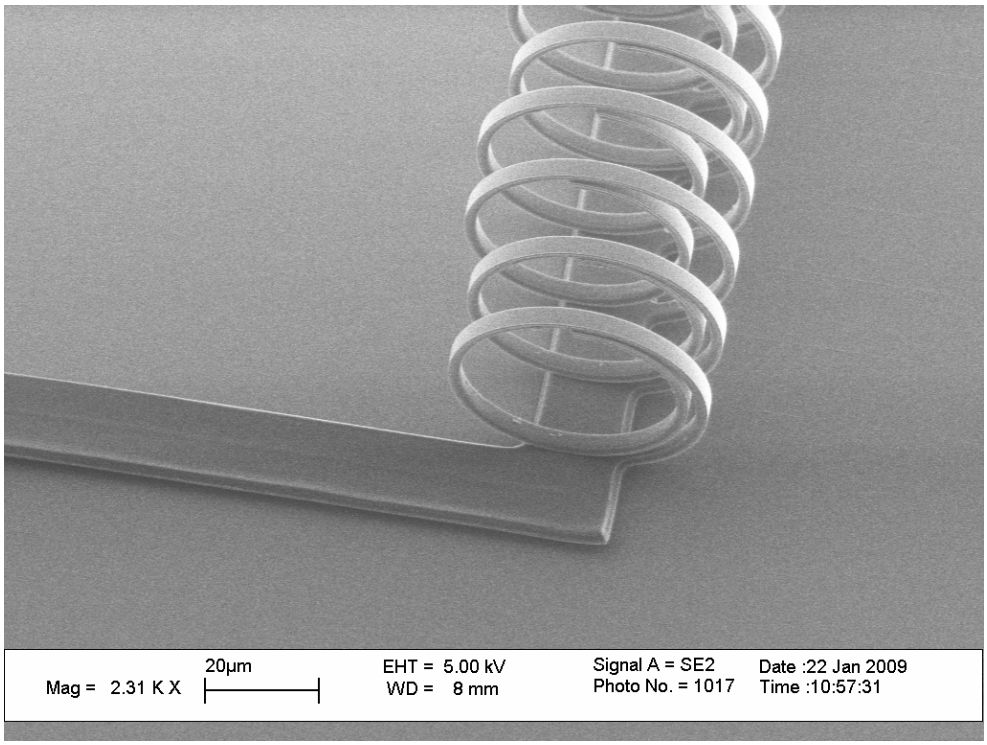

Figure 22. Chitosan bimorph beams exhibiting severe curling due to excessive residual stress

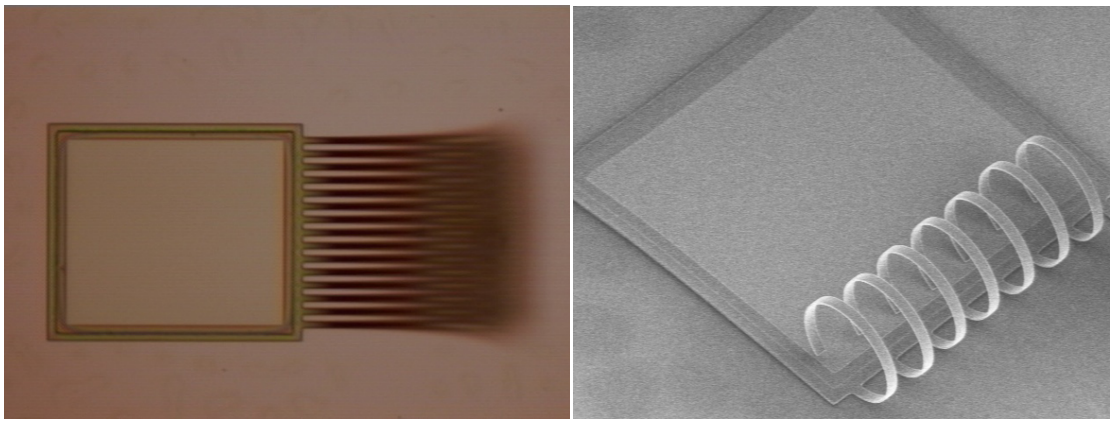

Figure 23. Comparison of chitosan bimorph beams in ambient (left) and in SEM chamber (right)

2.5.3 Chitin

Chitin bimorph beams were successfully fabricated following the process previously described. An SEM image showing an array of cantilevered bimorph beams composed of chitin on top of poly-silicon is presented in Fig. 24, below. An image in which the two distinct layers of material at a beam tip are visible is provided in Fig. 25. As expected, fabricated chitin bimorphs did not display a strong dependence of their curvature on relative humidity. A comparison of a chitosan bimorph beam device in ambient conditions (left) and in the SEM

chamber (right) is provided in Fig. 26 and shows little change in the shape of the bimorph beams.

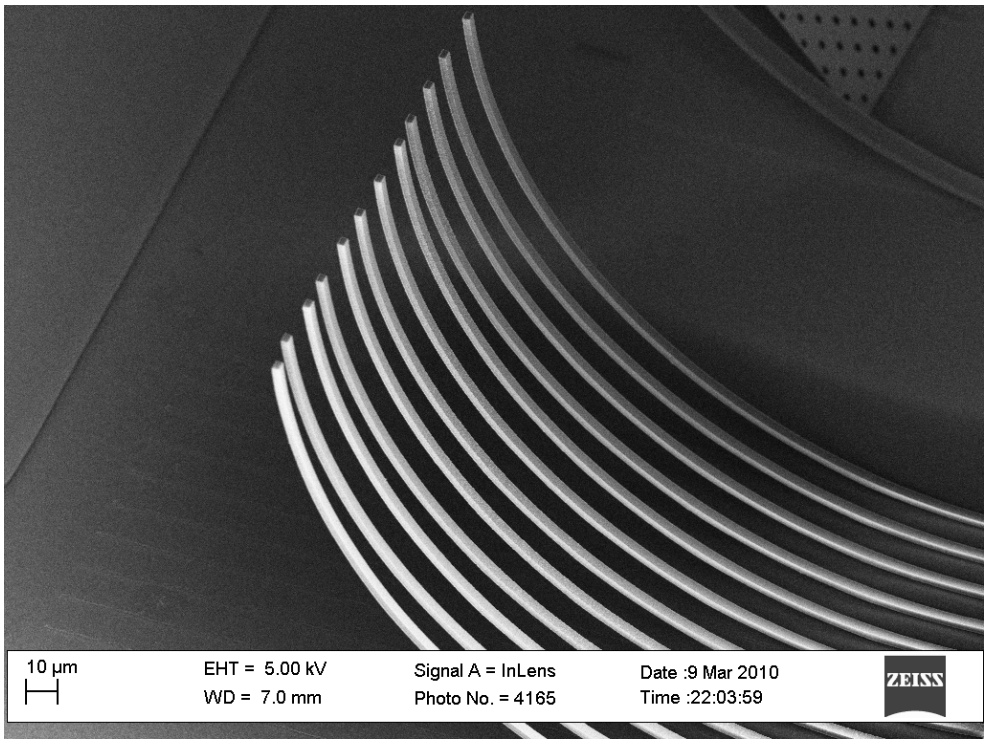

Figure 24. Array of chitin bimorph cantilever beams

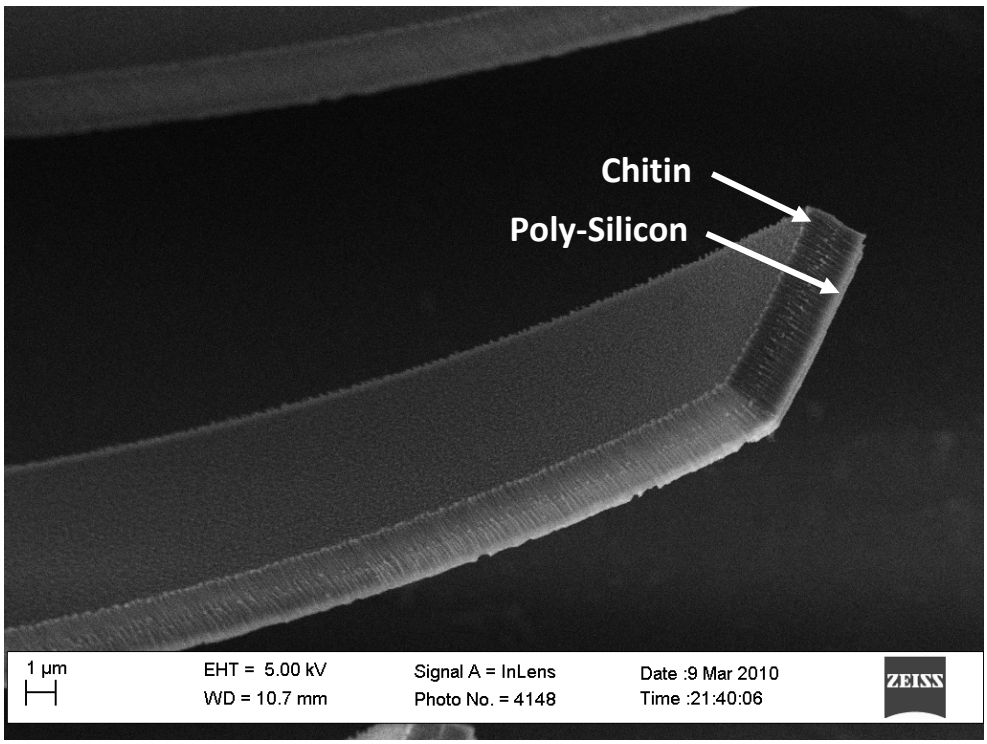

Figure 25. Tip of bimorph cantilever beam composed of chitin on poly-silicon

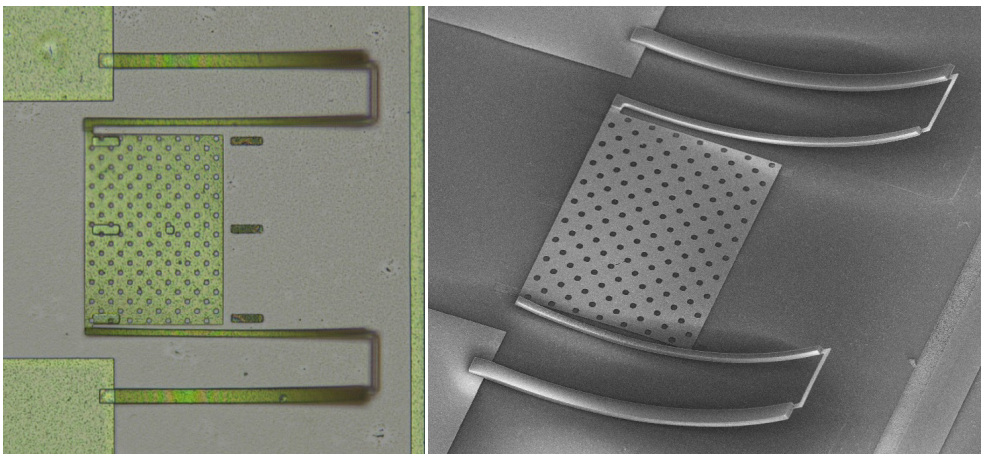

Figure 26. Comparison of released chitosan bimorph beam device in ambient (left) and in an SEM chamber (right)

2.5.4 Discussion

Several un-patterned silicon test wafers were coated with photoresist, developed (but not exposed to lithography), baked, and exposed to HF vapor, thereby mimicking the photoresist bimorph process. The levels of residual stress in these wafers were measured using a laser interferometer thin-film stress measurement instrument (Tencor FLX-2320). The measured levels of residual stress ranged from 7.4 to 9.0 MPA (tensile) which is in reasonable agreement with the observed deflections in fabricated bimorphs and lends support to the validity of the models used.

As discussed above, chitosan beams displayed significant sensitivity to changes in ambient humidity. Since their moisture content would also be affected by variations in temperature, chitosan bimorph beams would not be ideal for us as thermal infrared detectors. For this and other reasons, chitin bimorphs are more suited to this research, though their fabrication is more complicated because chitin cannot be dissolved for spin casting.

Adhesion

Adhesion between the polymer layers and the poly-Si was observed to be adequate for the fabrication of bimorphs using photoresist, chitosan, and chitin. However, in the most extreme cases of curling for chitosan bimorphs, delamination between the layers was occasionally observed. An example of such delamination is shown in Fig. 27, below. For most beams, adhesion was adequate to allow large reversible deformations in the bimorphs and was also observed to maintain stability over a period of at least several months in ambient conditions. However, during the removal of the protective tape following wafer dicing, bulk (un-patterned) areas of chitin and chitosan were usually removed. Although not affecting the fabricated devices, this observation revealed inferior adhesion of chitin and chitosan compared to photoresist.

Various methods of increasing the adhesion of chitin and chitosan such as chemical treatments, surface roughening, or topographical features in the bimorph beams may be beneficial.

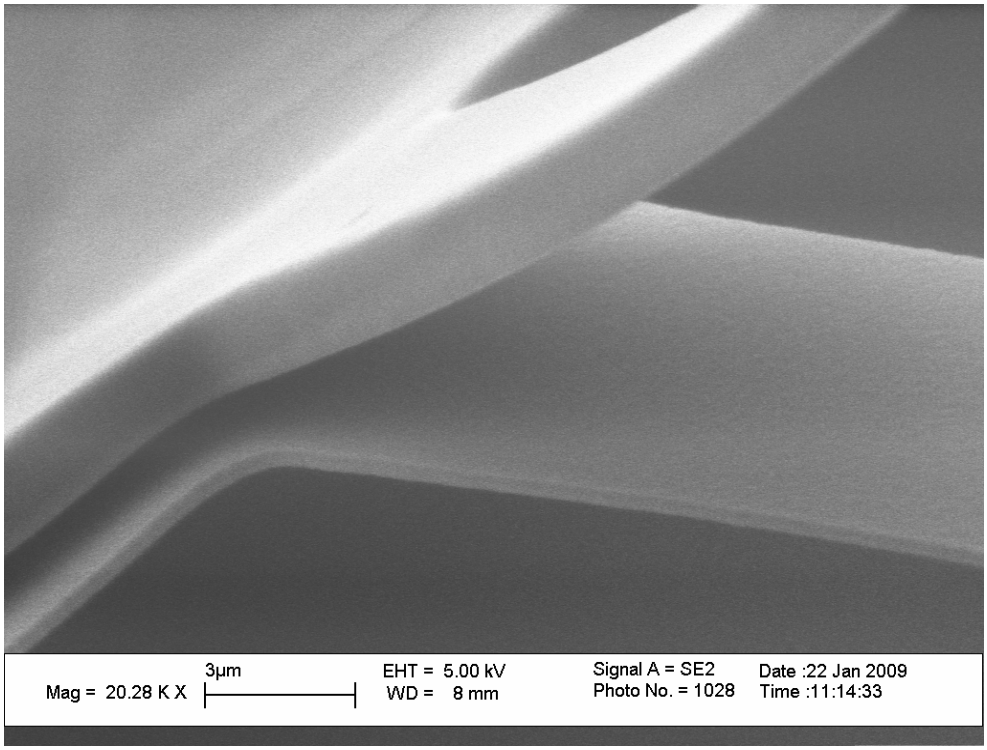

Figure 27. Delamination of layers in a chitosan bimorph

Chapter 3: Sensor Design

This chapter describes the design of a polymer bimorph thermo-mechanical infrared sensor. The mechanical deflection of the detector is measured as a change in electrical capacitance. As previously discussed, several readout mechanisms are possible for thermo-mechanical infrared detectors. The most common are optical and capacitive methods. Optical methods usually achieve lower noise levels but often require complicated alignments and experimental apparatuses. However, simpler optical readout methods have recently been demonstrated [47] and will be further explored in Chapter 4. Capacitive readouts have the advantage of being potentially simpler and are able to utilize commercially available CMOS readout circuitry. A design for use with a capacitive readout scheme was primarily selected for the purposes of this research. However, the design is also compatible with optical readout methods. The following chapter discusses the various considerations in this design.

3.1 Modeling Deflection and Capacitance

In order to model the deflection of thermo-mechanical infrared sensors, standard bimorph bending theory, as previously discussed, was utilized. The final shape of bimorph beams is a combination of the initial curvature of the beam from residual stress, ρ_i, and the curvature of the beam due to thermal bending, ρ_t, such that:

$$\frac{1}{\rho} = \frac{1}{\rho_i} + \frac{1}{\rho_t} \tag{38}$$

where ρ is the radius of curvature of the bimorph beam. The thermal curvature and initial curvature due to residual stress are calculated according to the Eqs. (33) and (35), respectively. These equations assume constant material properties, uniform stresses, and uniform temperatures in the beam. Given these assumptions, the beam will assume the shape of a circular arc. In that case, the distance, $y(x)$, from the substrate to any cross section along the length of the beam can be calculated as:

$$y(x) = g_0 + \rho\left(1 - cos\frac{x}{\rho}\right) \tag{39}$$

where g_0 is the distance from the base of the beam to the substrate, as shown in Fig. 28, below.

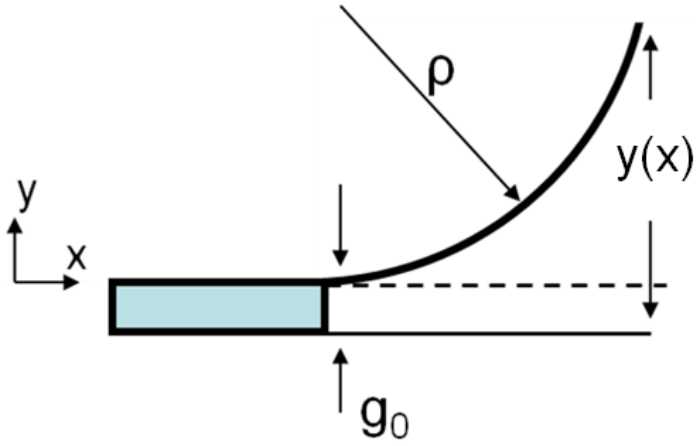

Figure 28. Geometry of a bent beam with an initial gap based on anchor thickness

The electrical capacitance can be measured from one deformable structure to another, but is most frequently measured from the beam to either the substrate or a thin planar electrode on the substrate. A simple model for capacitance follows that of a parallel plate capacitor and has been utilized in the literature [102] so that that the capacitance of a bent beam, C, such as that shown in Fig. 28 is given by:

$$C = \varepsilon_r \varepsilon_0 w \int_0^L \frac{1}{y(x)} dx \tag{40}$$

where ε_0 is the permittivity of free space, ε_r is the dielectric constant of the medium between the beam and substrate, and w and L are the width and length of the beam, respectively. This formula, however, neglects fringing fields. An analytical formula for the capacitance of a beam, including the contribution of fringing fields, was proposed by Chang [103] and verified experimentally with similar MEMS scale structures in the literature [104, 105].

$$C = \varepsilon_r \varepsilon_0 \int_0^L \left[\left(\frac{w}{y(x)} \right) + 0.77 + 1.06 \left(\frac{w}{y(x)} \right)^{.25} + 1.06 \left(\frac{t}{y(x)} \right)^{.5} \right] dx \tag{41}$$

For a capacitive readout device, the temperature conversion sensitivity is derived from the temperature coefficient of capacitance (TCC) defined as:

$$TCC = \frac{1}{C_S} \frac{\Delta C}{\Delta T} \tag{20}$$

where C_S is the capacitance of the sensor at equilibrium, and $\Delta C / \Delta T$ is the change in capacitance for a given change in temperature of the sensor. This quantity, which can be calculated based on the models for deflection and capacitance presented above, is an important characteristic of detectors and is analogous to the temperature coefficient of resistance (TCR) for resistive micro-bolometers. The enhanced thermal bimorph effect from the use of polymers increases the TCC, but geometric design should also consider the maximization of the TCC. TCCs of over 100%

per degree have been demonstrated [37]. For comparison, a TCR of 4% per degree is considered very large for micro-bolometers [34].

3.2 Limitations of Simple Cantilevers

Although simple MEMS bimorph cantilevers, such as those presented in Chapter 2, can be used with capacitive readout systems, the presence of residual stress during fabrication causes them to curve away from the substrate which will greatly reduce their sensitivity. Since the greatest mechanical motion occurs at the tip of a cantilever bimorph and the change in capacitance for displacement toward or away from the substrate is inversely proportional to the square of the distance, motion at the tip of a curled beam is essentially wasted.

A perfectly flat cantilever would have an extremely high TCC since its motion would be very near the substrate. However, researchers have struggled to fabricate flat bimorphs, even when using metal on semiconductor designs, due to residual stress and failures cause by sticking after release. Many techniques for mitigating the residual stress in multi-layered structures exist such as rapid thermal annealing at high temperatures and ion beam machining [106]. However, these techniques are not generally compatible with polymer layers.

An example plot of the change in capacitance for a temperature difference of 1 K for single cantilever beams of length 300 μm and width 20 μm as a function of the residual stress in the polymer layer is provided below in Fig. 29, below. In this instance, the beam is composed of 1 μm of OCG-825 photoresist on 0.2 μm poly-Si with a gap between the base of the beam and the substrate of 2 μm. It is assumed that the poly-Si has no residual stress. Since typical values of residual stress for fabricated chitosan devices are about 12 MPa, the sensitivity of these devices is less than 1% of what it would be were the devices fabricated with no residual stress and therefore flat. As is illustrated in the plot, even a relatively small amount of residual stress would significantly compromise the sensitivity of such a device.

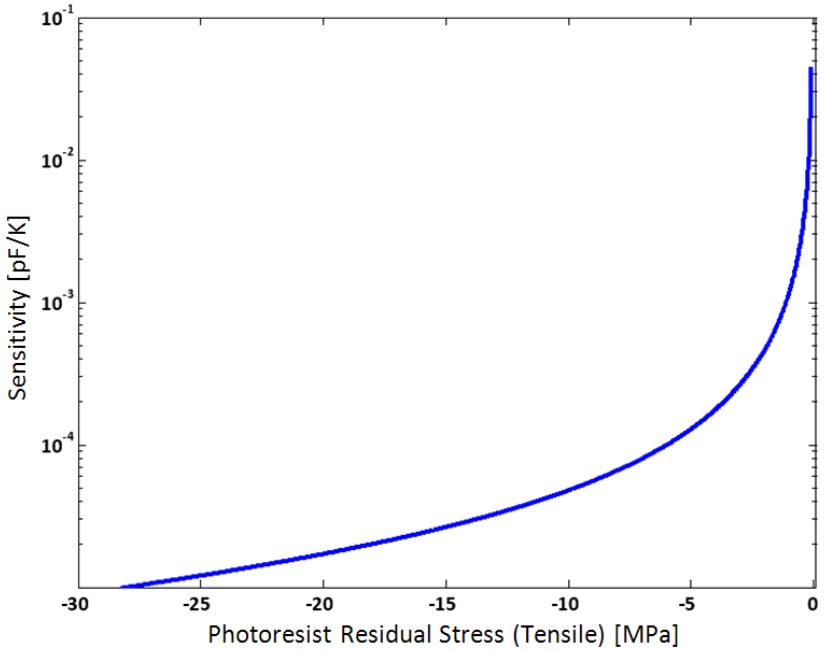

Figure 29. Plot of the sensitivity of cantilever beam as a function of the residual stress in the polymer layer

3.3 Double-Beam Design

Given the strong dependence of the sensitivity of capacitive bimorphs on the precise control of residual stress, they are not ideally suited to the goals of this research. In order to circumvent these limitations, a double-beam or "self-leveling" design was pursued. This concept was first demonstrated by researchers at Oak Ridge National Laboratory [45, 107] and will be explored in detail in this section.

3.3.1 Residual Stress Compensation

If a pair of identical bimorph beams is joined by a stiff mechanical linkage, as illustrated in Fig. 30, below, the first (anchored) beam will curl due to residual stress and the second (free) beam will curl back down by the same amount. The result is that the free end of the structure is level and at the same height as the anchored base of the structure. In this way, the structure "compensates" for the curling due to residual stress and any structure placed at the free end of the beam combination will be level and remain at its original, unreleased, height regardless of the amount of residual stress.

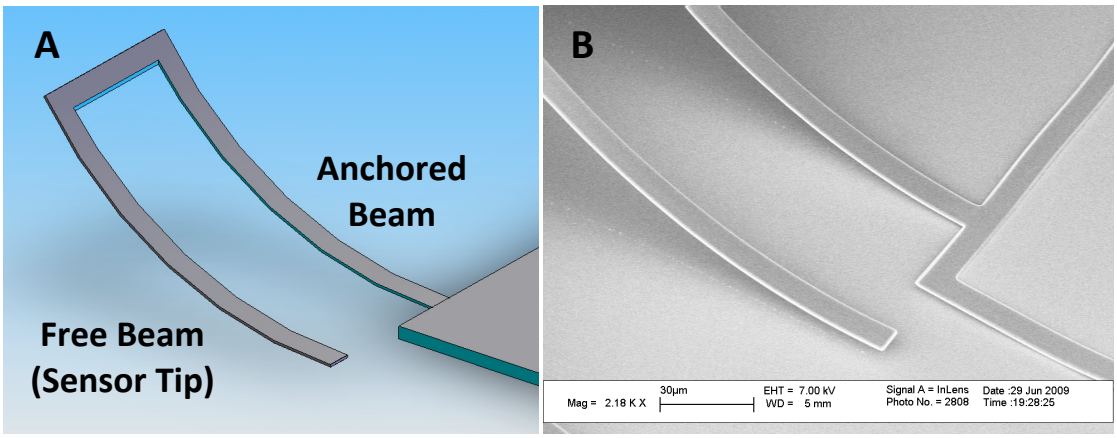

Figure 30. Illustration (A) and SEM micrograph (B) of double-beam concept geometry

Not only does this effect address the key limitation of simple cantilever geometries, it also helps to address the problem of non-uniformity in the fabrication of arrays. Ideally, pixels in an array are identical in initial shape following fabrication and release. However, subtle variations in material properties and dimensions usually lead to significant variations in the initial curvature of bimorph devices. This non-uniformity typically necessitates the need for pixel-by-pixel calibration and processing in an imaging array, which adds to the overall complexity of the system. However, the double-beam design will theoretically allow for uniformity of the position of sensor tips in an array, even if significant non-uniformities exist across the area of the array. This result, however, assumes that the non-uniformities between the two legs of the double-leg design are insignificant, which in practice has not shown to hold true for metal-semiconductor designs. Jones *et al.* speculated that local crystal grain variations in the top metal layer of their devices were the cause of non-uniformities in released double-leg device

arrays [5]. Even so, a double-beam design will clearly reduce the effect of wafer scale non-uniformities in material properties and thicknesses.

3.3.2 Thermal Design for Double-Beam Geometries

The double-beam bimorph geometry requires special consideration with regard to thermal design. In the following section, the advantages and challenges of double-beam designs are discussed. Several published innovations are reviewed and novel methods for enhancing performance are proposed.

Ambient Temperature Compensation

Since identical deformations in the two beams of a double-beam design effectively cancel each other out, any effect which causes equivalent deflections in both beams will, to first order, not affect the position of a structure placed at the free beam tip. If changes in the ambient temperature surrounding a device occur slowly, and both beams in the device change temperature together, the resulting deflections should not significantly affect the position of the sensor tip. Datskos *et al*. [45] compared the influence of ambient temperature variations on two functionally equivalent metal-ceramic bimorph structures: one with a double-leg design and one without. They found that the double-leg design exhibited only 3% of the deflection of the device with no compensating legs for an ambient temperature change of 20 °C.

Sensitivity to ambient temperature variation is a serious problem in uncooled infrared detectors. Thermal effects from camera electronic components, the user, or the environment can create thermal gradients over the detector array which can appear as distortion patterns on the image produced by the camera. In addition, many detectors such as micro-bolometers experience a change in sensitivity as a function of the ambient temperature [36]. As a result, many uncooled infrared cameras today must employ a thermoelectric cooler. Such systems have been reported to require as much as 500 to 2000 mW of power and 3 to 10 cm^3 of additional volume [35]. Therefore, the ability to design double-beam systems to compensate for ambient temperature variations is a significant advantage and can help to achieve the goals of a very low powered and inexpensive imaging system.

Thermal Isolation Region

A natural result of the ability of the double-leg design to compensate for ambient temperature variations is that it will also work to eliminate any sensitivity from infrared radiation which heats both the inner and outer legs equally. For this reason, thermo-mechanical infrared detectors with double-beam geometries need to be designed in order to maximize the difference in temperature between the inner and outer beams in response to incident radiation. The conventional approach to addressing this problem in the literature has been to include an absorbing structure attached to the inner (free) leg of double-beam designs and to create a thermal isolation region between the two beams. Such a design, created by Corbeil and Datskos [45] is shown in Fig. 31, below.

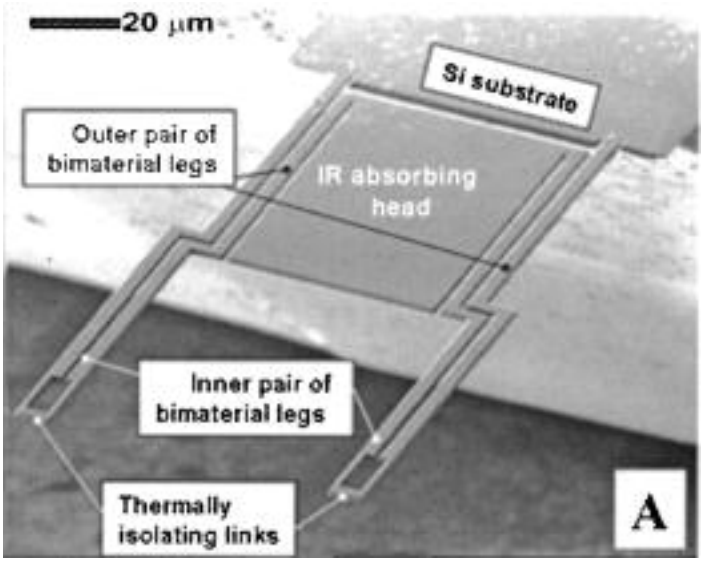

Figure 31. "Self-leveling" micro-cantilever thermal detector design, from [45]

Assuming the majority of the heat is absorbed in the infrared absorbing head and the substrate effectively acts as a constant temperature heat sink, the thermally isolating links will tend to create a temperature differential between the inner and outer beams because of their lower thermal conductivity. In the instance shown, the thermal isolation regions are composed of silicon and the bimorph beams are composed of gold on silicon. The absorbing head also acts as a mirror for an optical readout scheme. The decrease in thermal conductivity of this region is achieved by a reduced cross section and increased length. However, there will obviously be a certain degree of heating in the outer pair of legs which will reduce the sensitivity of this device.

Other Methods to Increase Double-Leg Temperature Difference

For polymer bimorphs, the situation is more complicated because the bimorph legs themselves are designed to act as infrared absorbers. Infrared absorption in the outer (anchored) compensation leg will result in decreased sensitivity since the resulting temperature rise and increased curvature will act to cancel out the response of the inner leg. Therefore, preventing irradiation of the outer leg will improve sensitivity by increasing the temperature difference between the inner and outer legs.

One way to prevent irradiation to certain areas of a sensor is by fabricating an integrated shield pattern. Shielding could be achieved in a number of ways. In back-illuminated devices, devices which are designed to receive infrared radiation through the substrate, a relatively thick metal layer could be patterned on the back of the substrate such that only infrared radiation aligned with the intended absorption region of the sensor would be transmitted and infrared radiation that would fall upon other areas would be reflected away. Patterning the shielding layer on the back of the substrate would be simpler than patterning shielding on top of the substrate, but below the device layers. For front-illuminated designs, shielding may be accomplished by a thin metal layer on top of the outer bimorph beams. However, this metal layer would introduce the same complications as previously discussed for metal layers intended to reflect radiation for a double pass through the beam.

Since temperature rise in the thermal isolation region is undesirable, the shielding pattern could also block that region from being illuminated. Another possibility is to utilize the curvature of the bimorph beams to intentionally reduce the view factor of the thermal isolation region to incident radiation. If, as is usually the case, the incident infrared radiation is arriving normal to the substrate plane, a vertically aligned structure will receive very little radiant flux. In Fig. 32, below, a fabricated double-beam bimorph device with serpentine thermal isolation links which are aligned roughly normal to the plain of the substrate is shown to illustrate this concept.

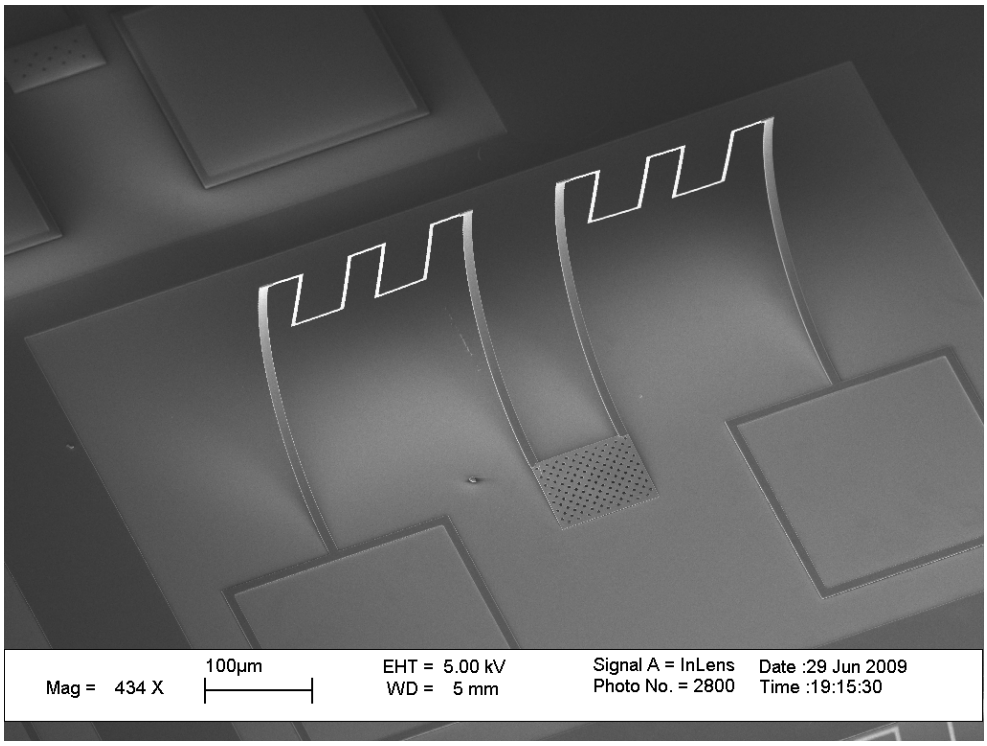

Figure 32. Thermal isolation regions tilted vertically to reduce radiant flux

3.3.3 Capacitance Simulations

Modeling of stress compensated designs was performed in order to compare the capacitive sensitivities with simple cantilever geometries. Two pairs of beams were compared and are illustrated in Fig. 33, below. The first geometry (A) was a pair of simple cantilevered beams, 300 µm long and 20 µm wide. The second geometry (B) was a double-beam, with each section composed of a beam 300 µm long and 20 µm wide. Both sets of beams were assumed to be composed of 600 nm of photoresist on top of 300 nm of poly-Si. These geometries were chosen since they are almost exactly the same size and therefore have approximately the same initial capacitance and require the same functional area. The initial residual stress curvature corresponded with stress free poly-Si and photoresist with ~6 MPa of tensile residual stress (typical for fabricated devices).

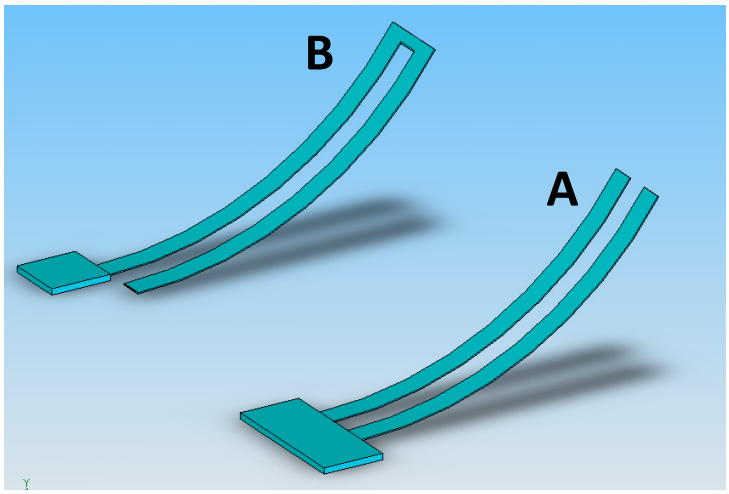

Figure 33. Illustration of geometry of beam pairs used for modeling

The analytic model assumed uniform temperature changes for the two simple cantilevers (A) and a temperature change confined to the outer (or free) arm in geometry B. The model utilized the parallel plate capacitance model, Eq. (40) above, which was found to vary only slightly from the fringing field model for these geometries. The gap between the base of the beams and the substrate was 1.5 μm and the dielectric was air.

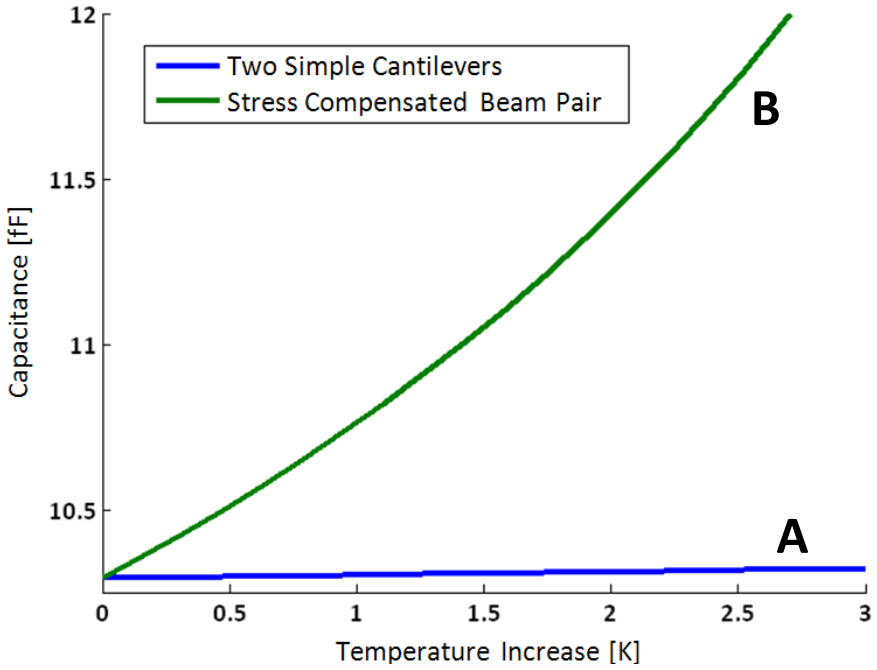

Figure 34. Comparison of change in capacitance for single (A) and compensated (B) beam pairs

Figure 34, above, illustrates the modeling results for these two devices for a temperature increase of 3 K over their equilibrium state. For the stress compensated design, the beam tip deflected about 0.8 μm toward the substrate. The dramatically larger change in capacitance for

the double-beam is a result of the residual stress compensation inherent to that design and the fact that the motion of the beam occurs near the substrate rather than at the tip of beams curled away from the substrate.

3.4 Layer Thicknesses

Another factor in the design of bimorph infrared sensors is the thickness of each layer. The goals are to maximize thermal deflection, thermal mass, and the absorption of target wavelengths of light. Obviously, all of these criteria cannot be simultaneously achieved. In addition, the limitations of manufacturing technologies must be considered. These include the limitations of chemical vapor deposition, spin-casting, and photolithography.

The bimorph bending equation, previously derived, is provided again below.

$$y = \frac{3L^2\Delta T(\alpha_a - \alpha_b)(t_a + t_b)}{\left[\frac{E_b' t_b^3}{E_a' t_a} + \frac{E_a' t_a^3}{E_b' t_b} + 6t_a t_b + 4t_a^2 + 4t_b^2\right]} \tag{32}$$

Here we see that the deflection is dependent on the ratios of the biaxial moduli and thicknesses of the two layers, not their actual values. It is easily shown [108] that for a fixed total thickness, the maximum thermal deflection, y_{max} is:

$$y_{max} = \frac{3(\alpha_a - \alpha_b)\Delta T L^2}{4t_{total}} \tag{42}$$

where t_{total} is the total thickness of the bimorph, and the optimal layer thicknesses, t_{a*} and t_{b*}, are given by:

$$t_{a*} = \frac{\sqrt{E_b'}}{\sqrt{E_a'} + \sqrt{E_b'}} t_{total} \qquad t_{b*} = \frac{\sqrt{E_a'}}{\sqrt{E_a'} + \sqrt{E_b'}} t_{total} \tag{43}$$

These relationships confirm the benefit of maximizing the difference in the coefficients of thermal expansion of the two materials, irrespective of their moduli. Through Eq. (43) it is evident that the thickness of the softer, lower modulus, material should exceed that of the stiffer material. In the case of polymer-semiconductor bimorphs, this indicates that the thickness of the polymer layer should be greater than that of the semiconductor for optical thermal deflection. Analyses for the optimization of thermal deflection when the thickness of one of the layers is held constant have also been published [109].

A plot illustrating the dependence of the thermal sensitivity of cantilever bimorph beams of different layer thicknesses is provided in Fig. 35, below, calculated according to Eq. (32). All beams are composed with a bottom layer of poly-Si of thickness 0.4 μm (solid lines) or 0.3 μm (dashed lines). The top layers are composed of either OCG-285 photoresist, aluminum, or gold with varying thicknesses. All beams are 100 μm long and 10 μm wide. The thermal sensitivity is defined as the vertical deflection of the beam tip for a one Kelvin temperature rise. In this plot, the enhanced sensitivity of polymer coated bimorphs due to the higher difference in

coefficients of thermal expansion is shown. Also apparent is the dependence of the optimal thickness ratios on the ratios of the stiffness of the two materials. Gold and aluminum, with their similar moduli, have optimal peaks at similar thickness ratios, while the optimal peaks of photoresist bimorphs occur for relatively thick top layers.

A plot showing the modeled thermal sensitivity as the thickness of both layers is varied is provided in Fig. 36, below. Such a plot can be used to optimize the deflection of a bimorph once the materials for a bimorph have been selected. The plot should be limited to thicknesses within the limits of the applicable manufacturing technologies. Figure 35 illustrates the superior thermal sensitivity of polymers, such as photoresist, compared to traditional materials such as aluminum and gold. The higher potential thermal sensitivity is an important advantage of polymer based bimorph devices. The flatter curve for photoresist also indicates a reduced sensitivity on performance to any variation in thickness from the optimal thickness due to manufacturing errors.

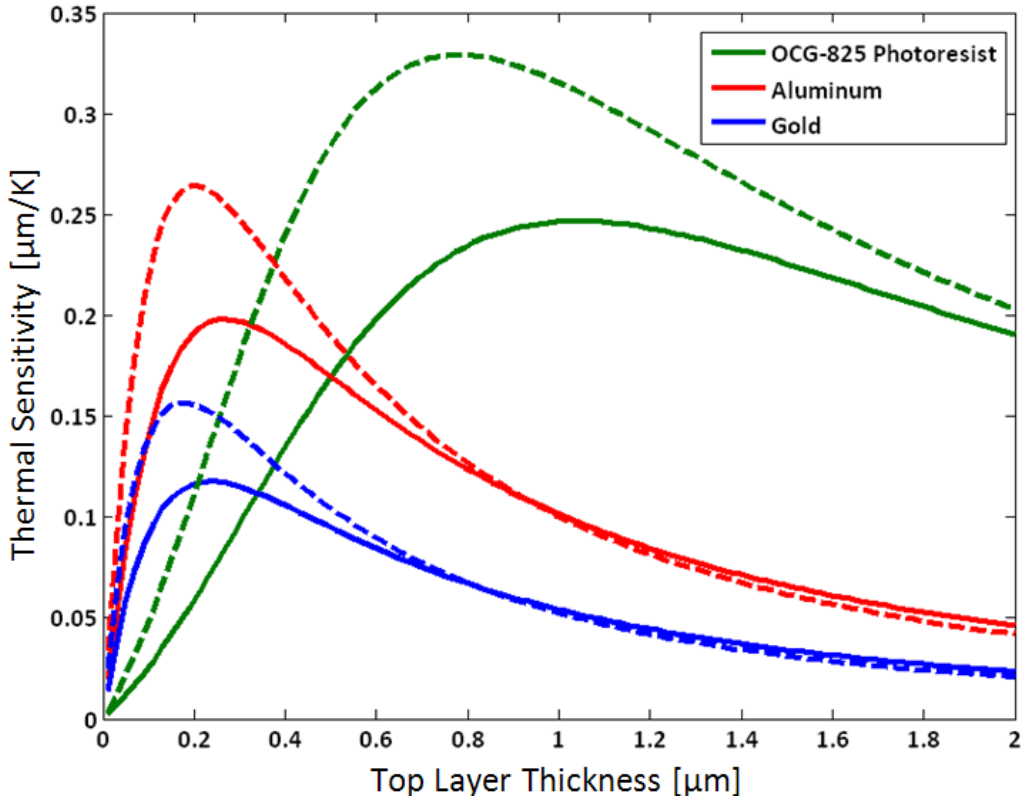

Figure 35. Thermal sensitivity of a 100 µm by 10 µm cantilever bimorph with bottom layer composed of poly-Si of thickness 0.4 µm (solid lines) and 0.3 µm (dashed lines) and top layer composed of either photoresist, aluminum, or gold as indicated

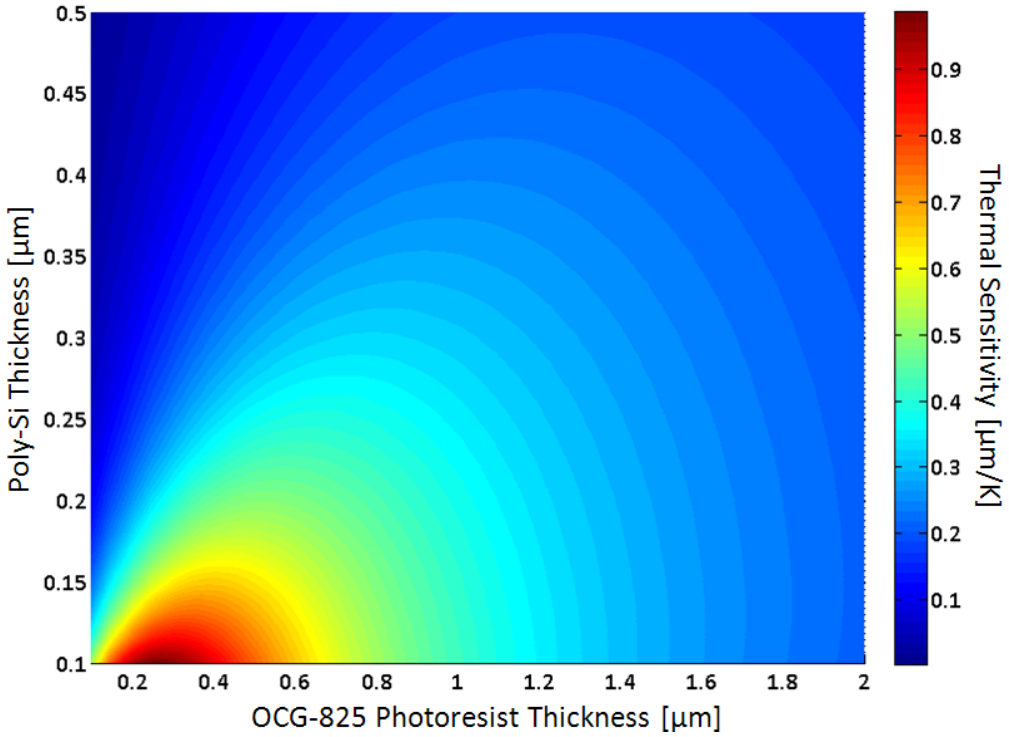

Figure 36. Thermal sensitivity of a 100 µm by 10 µm cantilever bimorph with bottom layer composed of poly-Si and top layer composed of OCG-825 photoresist

3.5 Nitride Spacers for Reduced Sticking and Pull-in Resistance

The adhesion of microstructures to adjacent surfaces, also called stiction, is a common problem in microfabricated devices [110]. Adhesion can occur during the final release of a microstructure or later during its use. Adhesion during release is usually caused by capillary forces while in-use adhesion is usually caused by electrostatic and van der Waals forces, or capillary forces when the device is exposed to a humid environment [111]. All of these forces increase as the gap between surfaces decreases and as the surface area to volume ratio increases. However, a capacitive readout device relies upon small gap distances and large surface areas in order to achieve maximum sensitivity. In addition electrostatic pull-in can act to bring structures into contact, at which point stiction forces can cause them to remain in contact. Therefore, it is expected that MEMS devices with small gaps have the potential to fail from adhesion and should be designed with this problem in mind.

Even if adhesion does not occur, when a capacitive sensor structure deflects enough to make contact with the substrate it creates an electrical conduction path and shorts the variable gap capacitor. Shorting was observed to result in unpredictable signals when using the capacitance measurement scheme in this research, which will be discussed later. The presence of insulating spacers should allow for the measurement of capacitance even at the end point of the sensor's range of motion (when it is in contact with the substrate).

In order to reduce the effective contact area of the devices in this research and to maintain electrical isolation even for extreme deflections, small patterned spacer structures were created between the substrate and the structural layer. An electrically isolating layer is needed

which is compatible with silicon surface micromachining and silicon oxide sacrificial layers. Silicon nitride is a suitable material which is frequently used and is etched relatively slowly by hydrofluoric acid (HF) [111]. It was therefore selected as the material for the spacers in this research.

3.6 Methods for Increasing Infrared Absorption

As previously discussed, maximizing the proportion of incident radiation of the target wavelengths which are absorbed by the sensor is a fundamental design goal for thermal infrared detectors. There are several methods which can be used to achieve this goal. First, consideration should be given to the effect of the thicknesses of the device layers on its absorption characteristics. Many MEMS materials, such as silicon, are effectively transparent to infrared light, though they may exhibit significant surface reflection.

Since metal is a good reflector of both visible and infrared light, a thin metal layer can be used as a reflector to induce a double-pass of radiation through the absorbing polymer. Since it is possible for the device to be illuminated from the front or through the substrate, a metal layer could be patterned on either the top (Fig. 37 C) or the bottom of the bimorph structure (Fig. 37 A) via sputtering or evaporation. However, any additional layers on the bimorph structure will affect its initial curvature due to residual stress and its thermal deflection sensitivity. In addition, metal layers will increase the thermal conductance of the device.

Many researchers have employed a resonant cavity absorber, a gap of thickness $\lambda/4$ or $\lambda/2$, between the absorber a reflector on the substrate, where λ is the target wavelength [42, 53, 54]. One possible instance of this method is illustrated in Fig. 37 (B). For thermal infrared imaging, radiation at 10 μm is usually targeted. However, these features tend to increase absorption primarily at the targeted wavelength and also impose limitations on the thickness of the gap as it relates to considerations like capacitive responsivity. Movement of the absorber relative to the substrate will also change the absorption characteristics of a device with a resonant cavity absorber, complicating its response as a function of intensity. For this reason, Mueller [83] proposed creating a "parasitic" resonant cavity which targeted a frequency of infrared light which would mostly be absorbed by the atmosphere (such as one from 5-8 μm), thus rendering it essentially nonfunctional. Without some method of residual stress compensation or mitigation, achieving the proper spacing for a resonant cavity absorber is difficult due to the unpredictable curvature and deformation of the released structures [53].

In order to preserve the composition, response, and thermal properties of the bimorph legs in a thermo-mechanical infrared detector, an absorbing paddle or head is often utilized [45, 46, 88] and designed for maximum absorption. This same paddle can be used as a large surface for optical measurements, where it usually acts as a visible light mirror, or as the primary movable electrode for capacitance measurements. The paddle is typically coated with an absorbing material or acts as part of a resonant cavity absorber. Many compositions are possible and nearly ideal absorption characteristics are possible. For example, a three layer absorber stack employing metal thin films and based on interferometric techniques has been shown to achieve an effective absorption of over 90% across a 8-13 μm waveband [112].

It should be noted that if irradiation is directed through the substrate, an effort to minimize absorption and reflection should be made. The use of anti-reflective coatings is

common, and some researchers have also explored the practice of etching small features into substrate surfaces to reduce reflection [52].

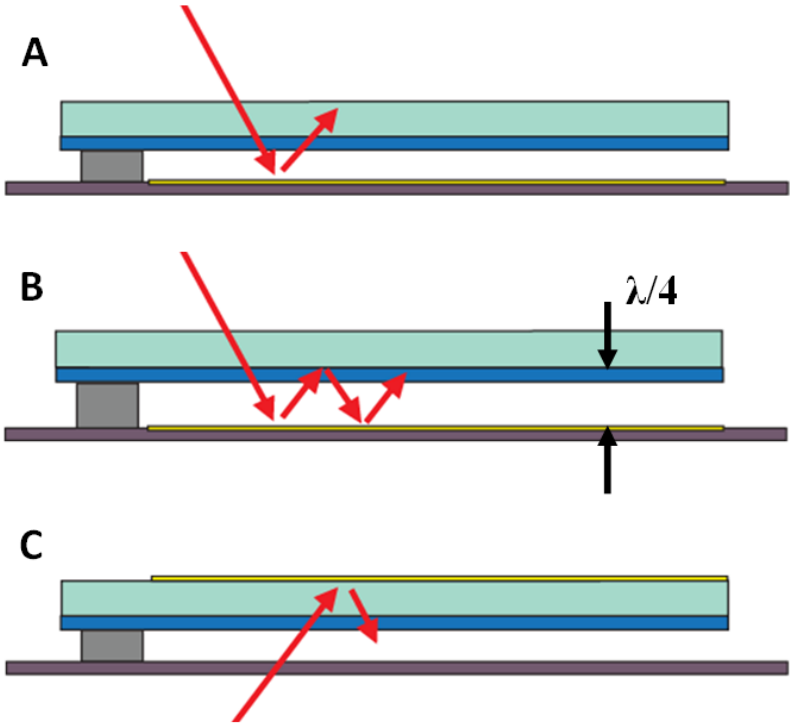

Figure 37. Illustrations of methods to increase infrared absorption: metal reflector under beam (A), resonant cavity absorber (B), and metal reflector above beam (C)

3.7 Design Summary

A schematic diagram summarizing the features of the sensor design is presented in Fig. 38, below. Shown in green (A) are the polymer coated bimorph sections in a double beam geometry for residual stress and ambient temperature compensation. These bimorph beams are joined by a thermal isolation linkage (B) which is thinner than the bimorph beams in order to minimize thermal conduction and may have a serpentine geometry in order to increase the length of this section. The bimorph beams are anchored to a large region used for wire bonding (C) and electrically isolated from the substrate by silicon dioxide. Nitride spacers are shown in blue (D) and are patterned on the substrate below the sensor paddle (E). The sensor paddle acts to increase the size of the capacitance for electrical measurements or acts as a mirror for optical measurements. It is patterned with etch holes in order to allow the passage of etchant during sacrificial oxide release. On the opposite side of the substrate, a layer of metal (F) is patterned below the outer bimorph beams and thermal isolation region in order to shield those areas from incoming infrared light when the sensor is illuminated through the substrate. Many different geometries are possible based on this design concept.

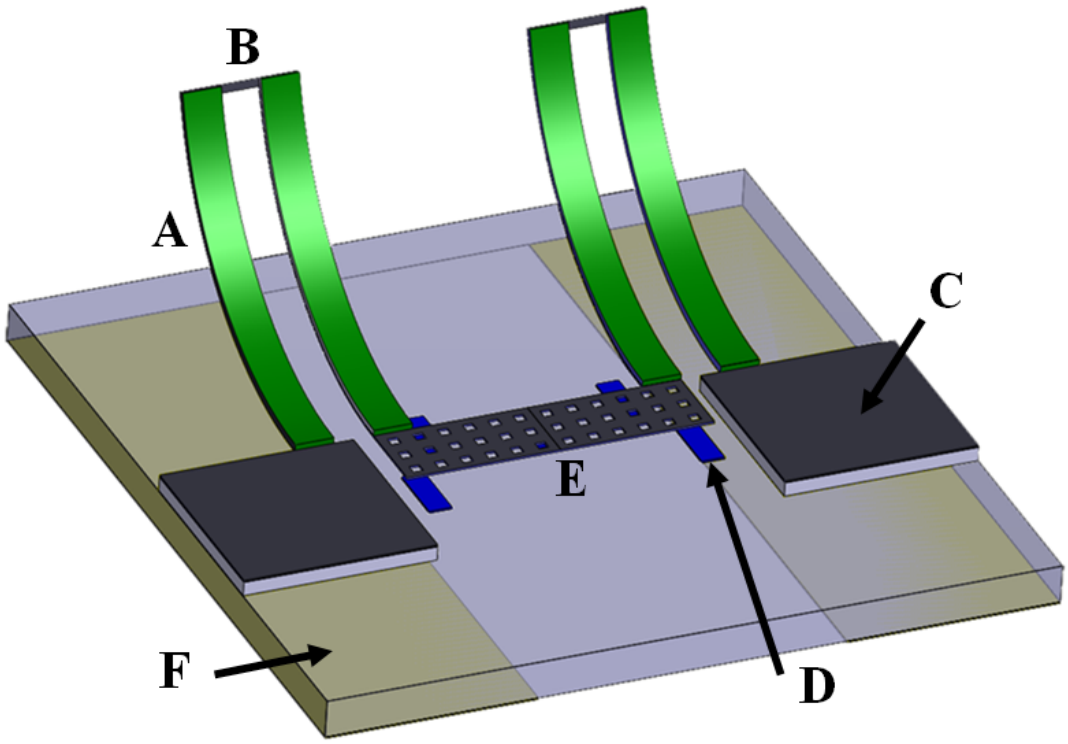

Figure 38. Diagram illustrating sensor design features: A) double bimorph beams B) thermal isolation linkage C) bond pad anchor D) nitride spacers E) sensor paddle F) backside shield

3.8 Fabrication

Fabrication followed the bimorph processes previously described in Chapter 2 with the addition of the patterning of a nitride layer onto the substrate before deposition of the sacrificial oxide layer. This section discusses the fabrication process.

3.8.1 Process Overview

The sensor paddle was protected during the etching of the poly-silicon by an oxide hard mask in exactly the same way as the anchors. However, the sensor paddle is patterned with etch holes, allowing the oxide etchant to release the entire paddle in a short amount of time compared to the anchors, which are only slightly under-etched at the edges in the same amount of time. The oxide hard mask is etched away from the sensor paddle and anchor, exposing the poly-silicon beneath it. The thermal isolation linkages are also defined by a hard oxide mask, but do not require etch holes due to their relatively narrow profiles.

Three masks were used: one defining the geometry of the nitride spacers, one defining the non-bimorph regions (the anchors, sensor paddle, and thermal isolation linkages), and one defining the bimorph beams. A metal backside shield was omitted from prototype fabrication in this research. All steps in the process prior to the final release are illustrated by a series of

microscope images contained in Fig. 39, below. In each image in the sequence, a step in the fabrication of an array of devices is shown and is described below:

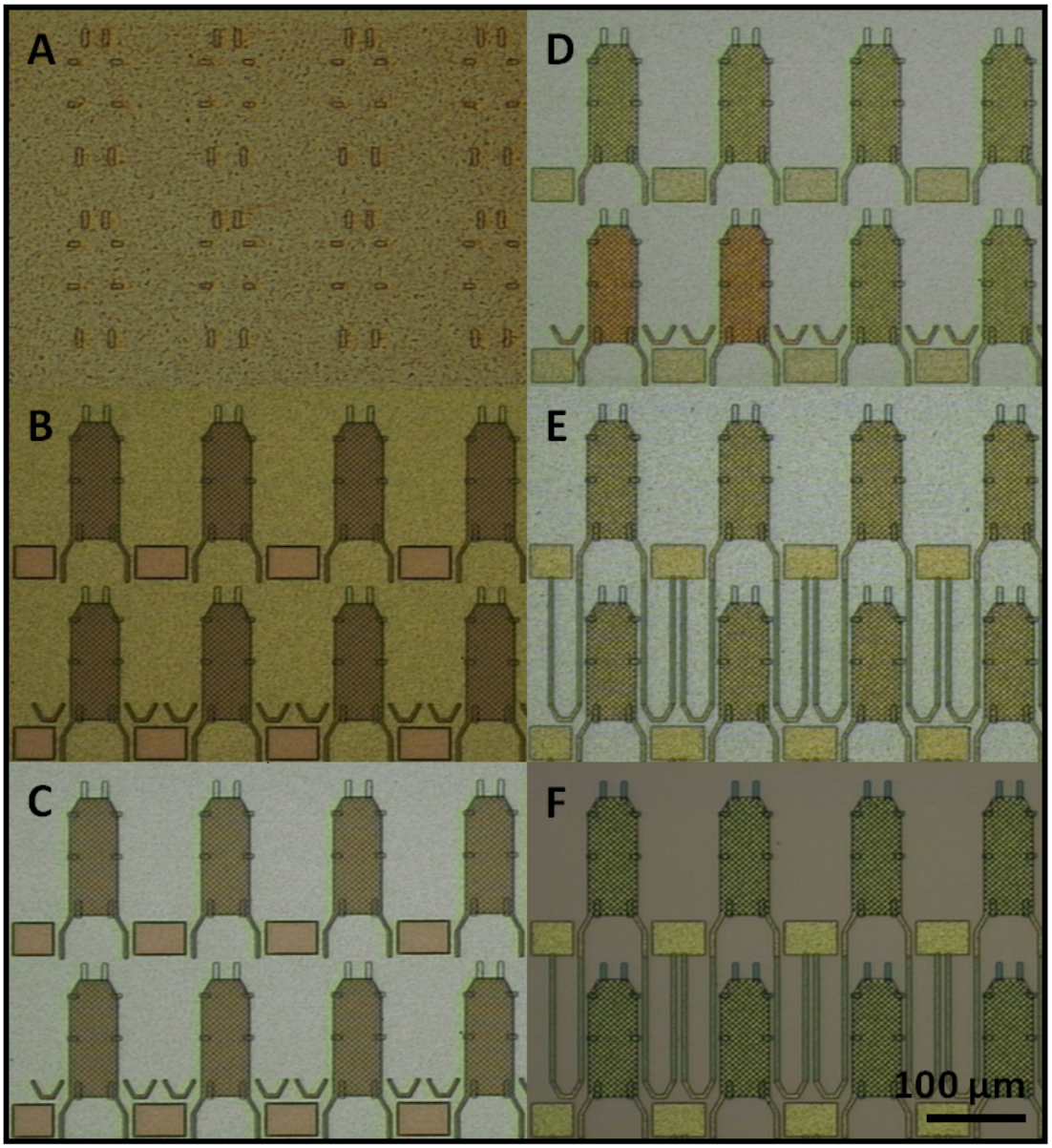

Figure 39. Microscope images illustrating various steps during bimorph device fabrication

A. All layers have been deposited. The nitride spacers, which were patterned with the first mask, are visible below through the structural and sacrificial layers.
B. Areas defining the anchors, sensor paddle, and thermal isolation linkages have been coated with photoresist and patterned by the second mask.
C. The top oxide layer, which defines the hard mask for non-bimorph areas, has been etched to expose the poly-silicon layer beneath.
D. The photoresist has been stripped away, revealing the oxide hard mask which will protect the non-bimorph areas during etching of the poly-silicon

E. A polymer layer has been patterned using the third mask which defines the bimorph beams.
F. The poly-silicon layer has been etched, revealing the sacrificial oxide layer beneath it. A layer of poly-silicon remains under all patterned areas. The device is now ready for the sacrificial oxide layer release.

For chitin devices, an additional etching step is required to remove the chitin and PMMA layers from non-bimorph areas, as previously described in the chitin bimorph process (section 2.4.3). This etching step follows the spin casting of chitin and PMMA over the entire wafer and is masked by a layer of photoresist. Chitin etching is illustrated in Fig. 40, below. In image (A), layers of chitin and PMMA coat the entire surface and a patterned layer of photoresist acts as a mask. In image (B), an oxygen plasma etch has removed the chitin and PMMA from the device, except beneath the photoresist regions which define the bimorph beams. The photoresist and PMMA are subsequently removed from above the chitin layer following poly-silicon etching using either a solvent or etching, as previously discussed.

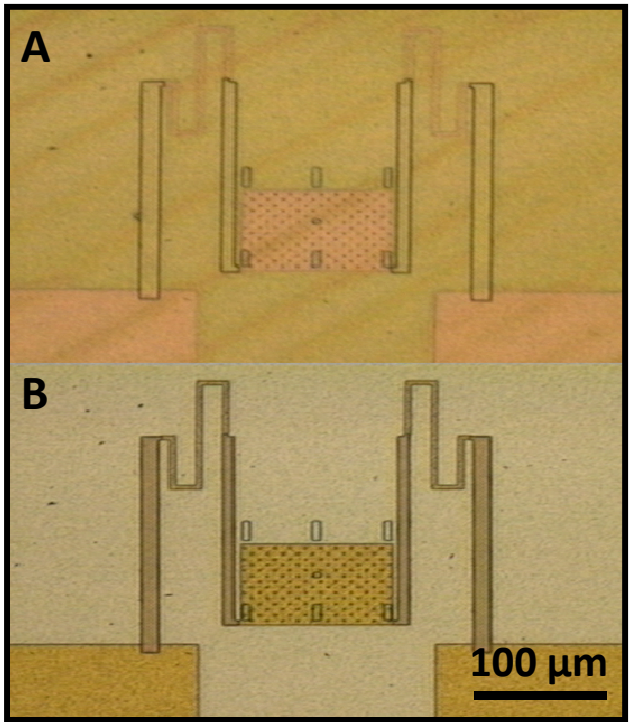

Figure 40. Chitin bimorph device before (A) and after (B) etching of chitin and PMMA by O_2 plasma

3.8.2 HF Vapor Release

Consideration must be given to the order in which different components of a device are released during the isotropic HF vapor release. The thermal isolation linkages of most devices are the first to release since these regions have a smaller width and therefore require less distance of undercutting from etching. For many devices, the areas which released first were observed to have a tendency to stick to the substrate with greater frequency than other areas. However,

breaking the etch into many small steps was found to mitigate this problem and result in a higher yield of properly released devices on a die. Alternating periods of 5 minutes of etching and 5 minutes of exposure to ambient, while still maintaining a temperature of 43 °C on the chuck between etches, was found to be optimal. The most likely causes of the observed improvement in quality of the etching are the limitation of the buildup of etching byproducts and the mitigation of moisture accumulation.

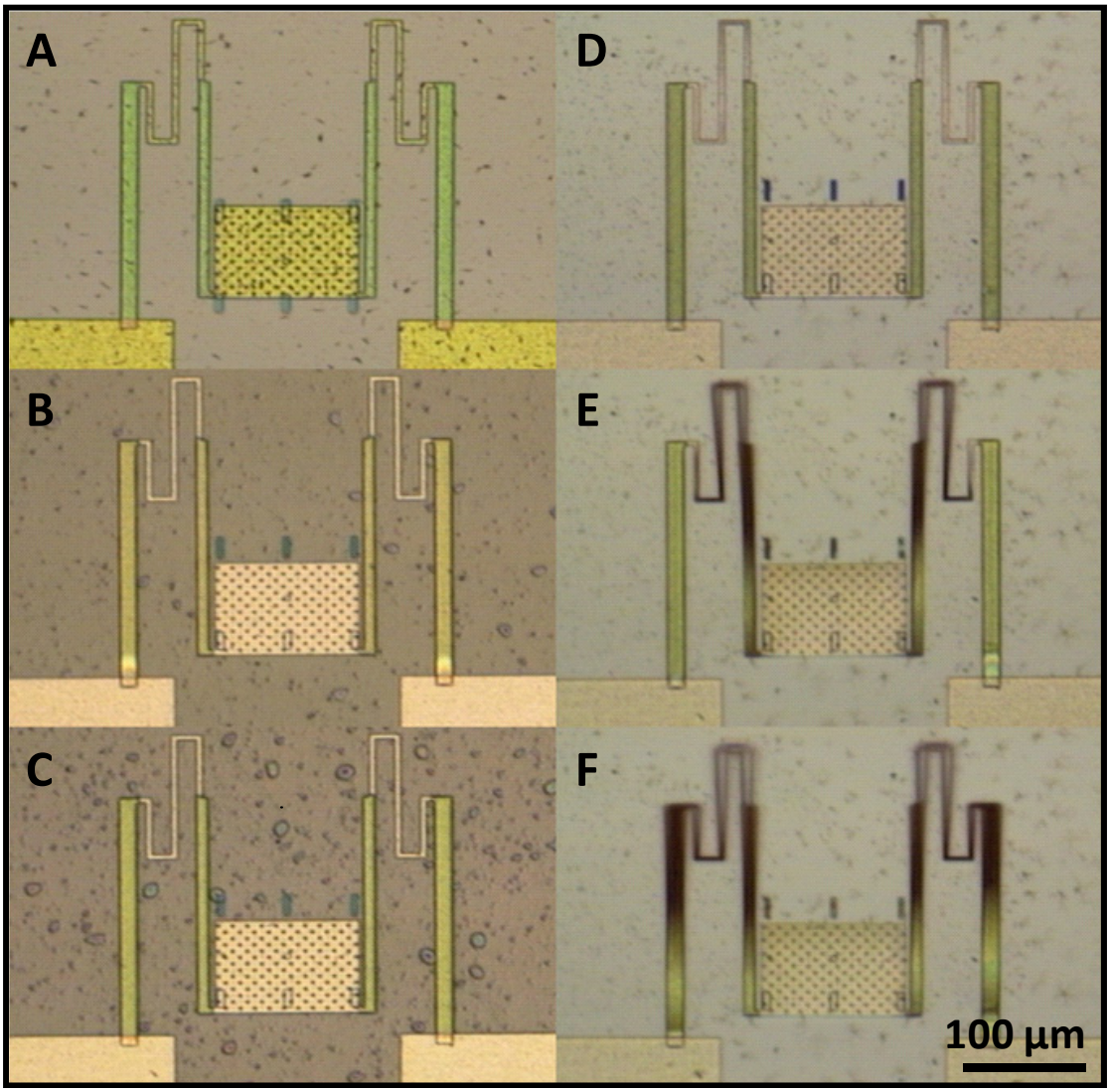

Figure 41. Sequence of microscopic images showing the progress of HF vapor etching

A series of microscopic images illustrating a typical HF vapor etch is presented in Fig. 41, above. Images (A) through (F) were recorded after cumulative etching times of 0, 10, 20, 40, 50, and 60 minutes, respectively. In (A), the oxide hard mask covering the paddle, thermal isolation linkages, and anchors is visible prior to etching and is yellow in color. These areas have been etched away in (B), revealing the poly-silicon beneath then. The progression of the etching of the sacrificial substrate layer is evident in (B) and (C) and has been completed in (D). In (E), the inner bimorph beams and the thermal isolation regions are released and are bending

away from the plane of the substrate. These areas are thinner than the outer beams and therefore require less time to release. Finally, both sets of bimorph beams are released in (F). The bimorph beams bend away from the substrate, but the sensor paddle remains flat.

The spacing of etch holes determines the necessary etch time for sensor paddles. The best results were found to occur for sensors which were designed to allow the sensor paddle to release at the same time as the outer bimorph beams in order to leave the paddle anchored until all other regions were released.

Chapter 4: Results and Evaluation

The results of sensor fabrication, along with experimental results using both optical and capacitance readout techniques are presented in this chapter. Initial estimates of sensor performance are evaluated and discussed.

4.1 Results of Fabrication

Sensors based on the design described in the previous chapter were fabricated with bimorph beams of photoresist on poly-silicon and chitin on poly-silicon. Various geometries were created for comparison and for different methods of testing and evaluation. A double beam sensor which incorporated a sensor paddle, nitride spacers, and thermal isolation regions tilted vertically is shown in Fig. 42, below. The bimorph regions in this device are composed of photoresist on poly-silicon. A detailed view of the sensor paddle is provided in Fig. 43 where the gap between the sensor paddle and substrate is visible. The sensor paddle is parallel to the substrate. Two micro-manipulated probes were used to confirm that the sensor structure was electrically isolated from the substrate by measuring the electrical resistance from one of the bond pads to a nearby location on the substrate. A white light interferometer (Wyko NT3300) was also used to confirm that the sensor paddle was not in contact with the substrate or the nitride spacers by measuring the height of the sensor paddle relative to the substrate.

An array of devices, of the same dimensions as those depicted in Fig. 39, above, is shown in Figs. 45 and 46, below. The bimorph regions are composed of chitin on poly-silicon. This geometry, once bond pads are replaced with buried traces (for an electronic readout) or smaller anchors (for an optical readout), could yield a dense array of devices with a fill-factor of approximately 0.5 or higher, appropriate for imaging.

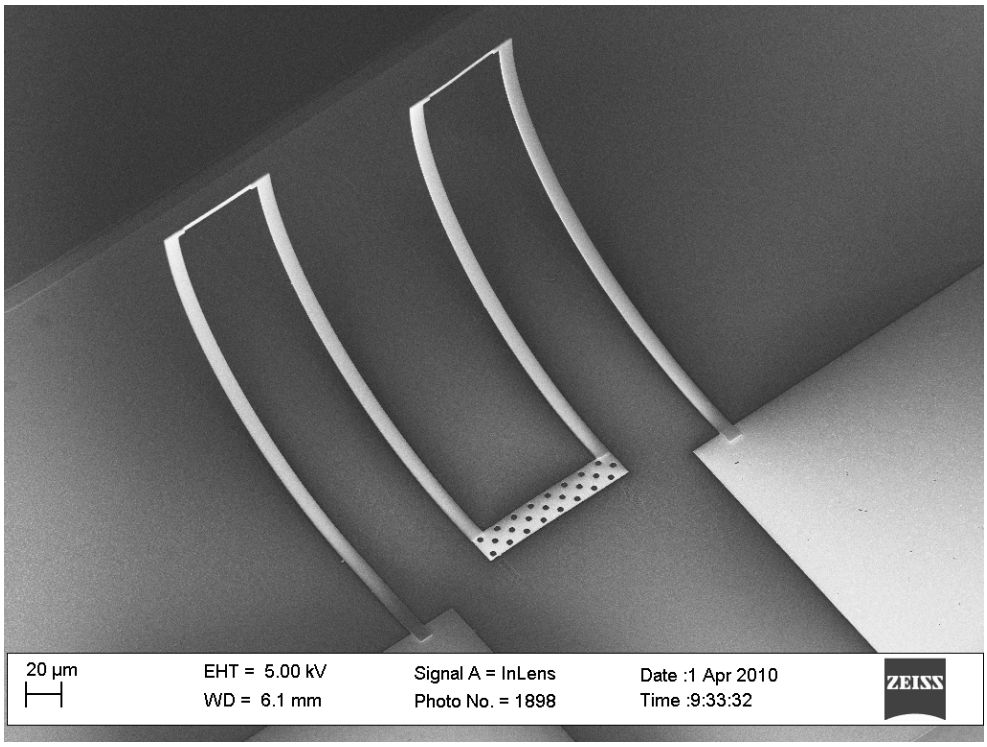

Figure 42. SEM of released double photoresist and poly-silicon bimorph beam sensor anchored to two large poly-silicon bonding pads

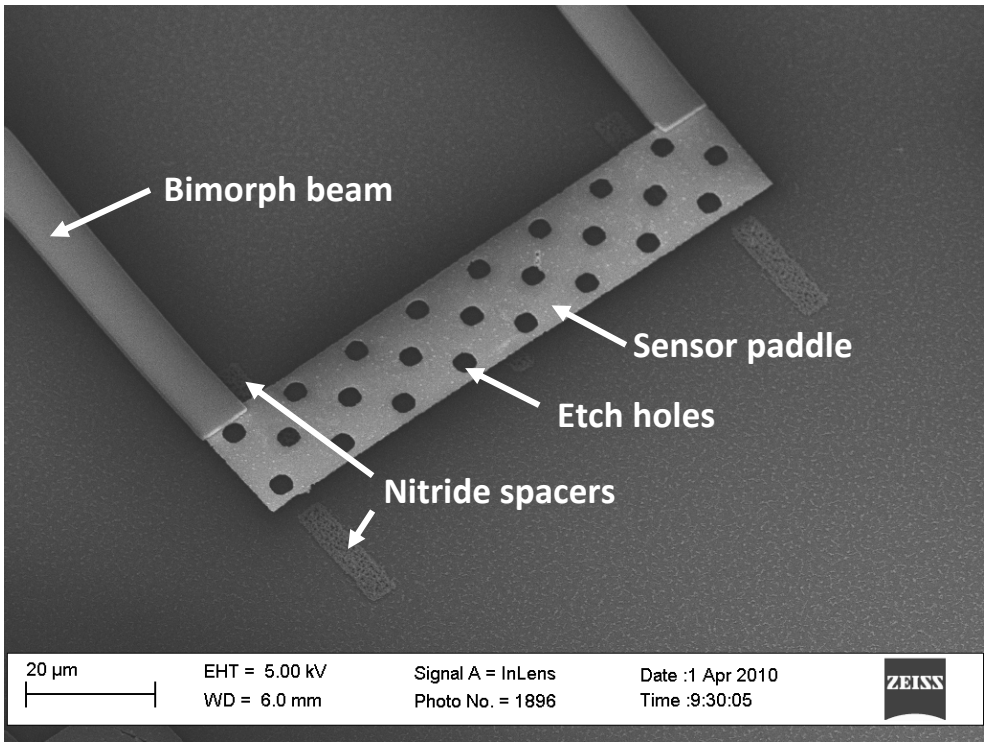

Figure 43. Poly-silicon sensor paddle suspended about substrate and nitride spacers

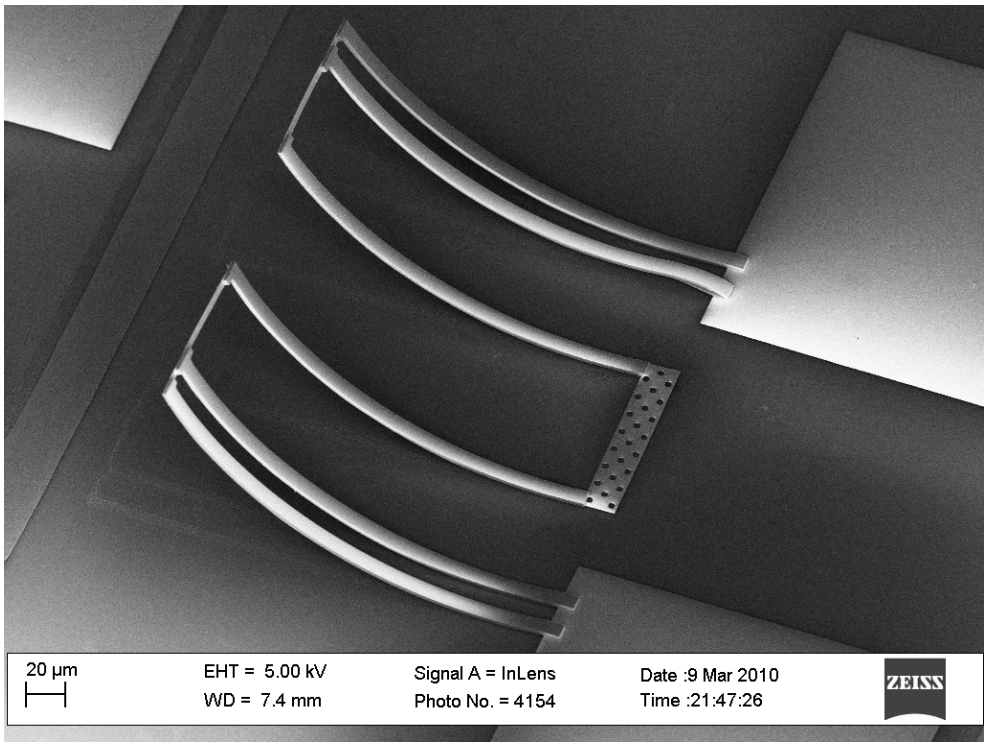

Figure 44. Chitin bimorph sensor with twin outer beams for increased strength

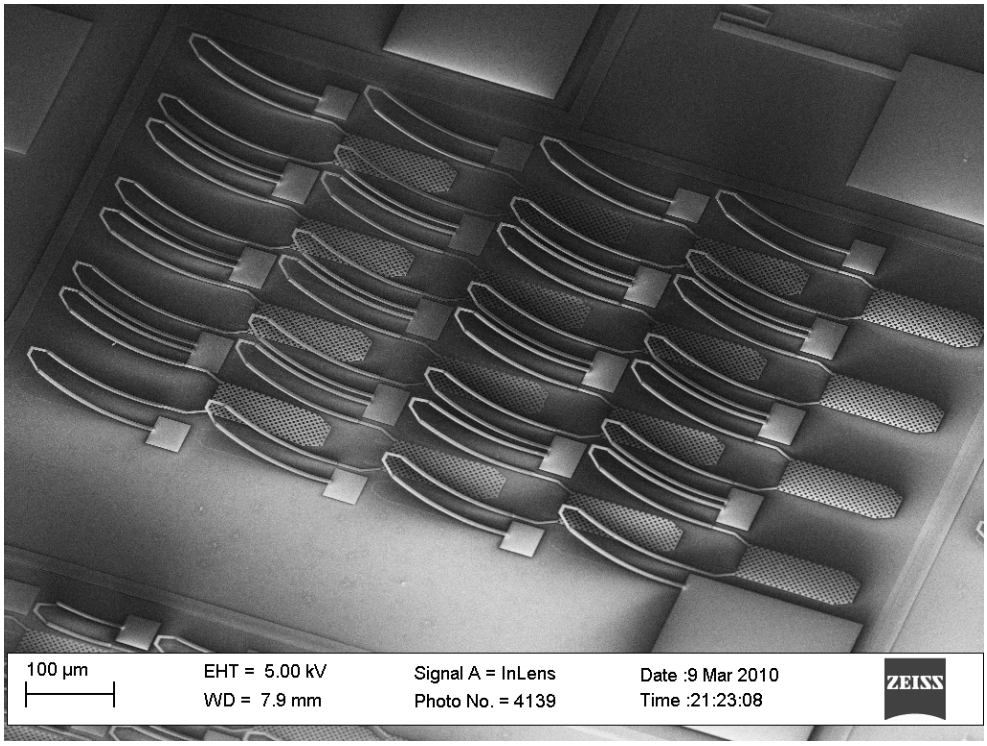

Figure 45. Four by four array of chitin bimorph sensors composed of chitin on poly-silicon

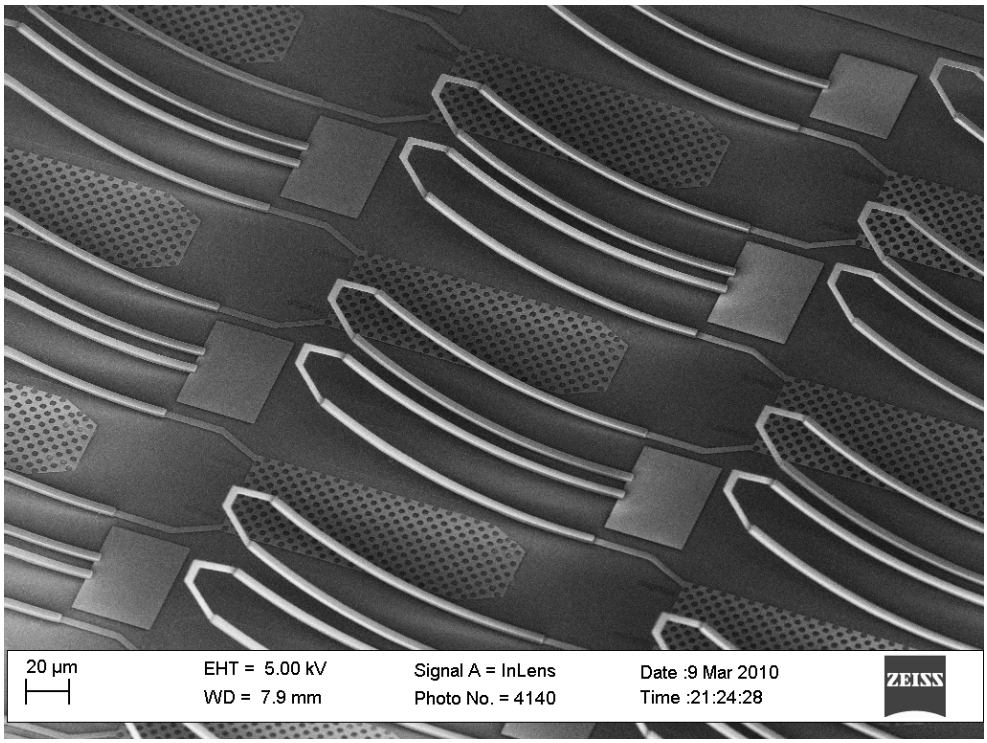

Figure 46. Detail of array of chitin bimorph devices

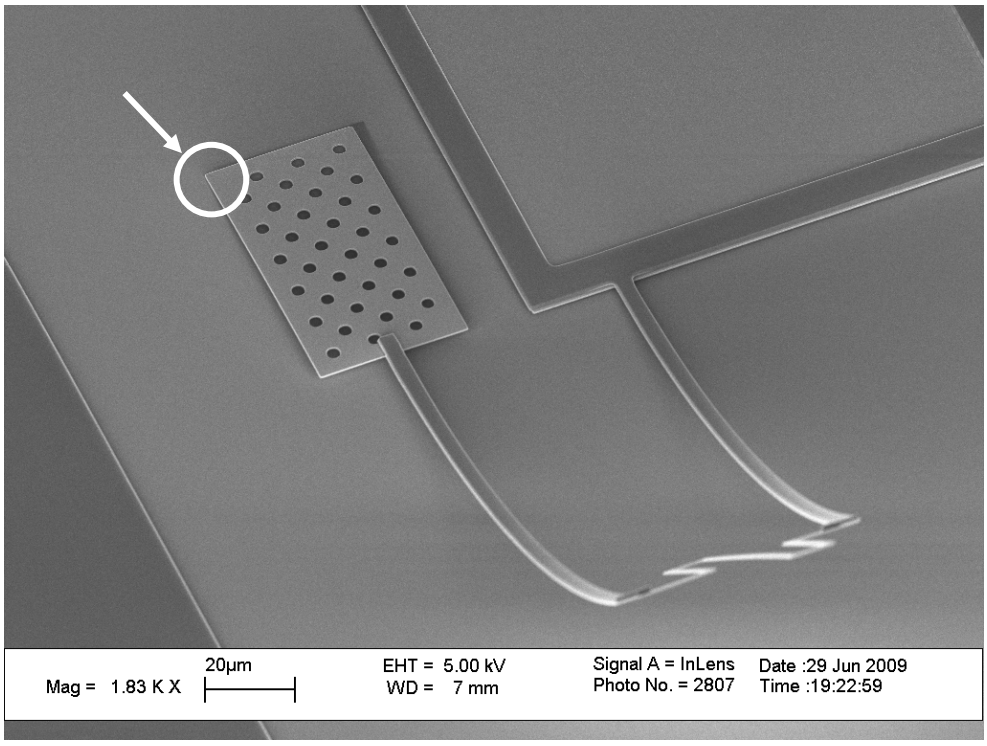

Figure 47. Released single-sided device with serpentine thermal isolation region, shown contacting the substrate at circled location

A device supported from only one side is shown in Fig. 47, above. This device was fabricated without nitride spacers and with a relatively thin sacrificial oxide layer and was therefore observed to make contact with the substrate upon release. It also incorporates a serpentine thermal isolation linkage. Even longer thermal isolation linkages are possible, with one such geometry demonstrated in Fig. 32, above.

It should be noted, however, that the effects of charge accumulation during SEM imaging were often observed to cause released structures to be pulled to the substrate, even though samples had been coated with a thin layer of gold particles. When devices were pulled to the substrate from charging, contact was observed either at the sensor paddle or the base of the bimorph beams. For this reason, SEM inspection is not a reliable way to inspect the success of the release step.

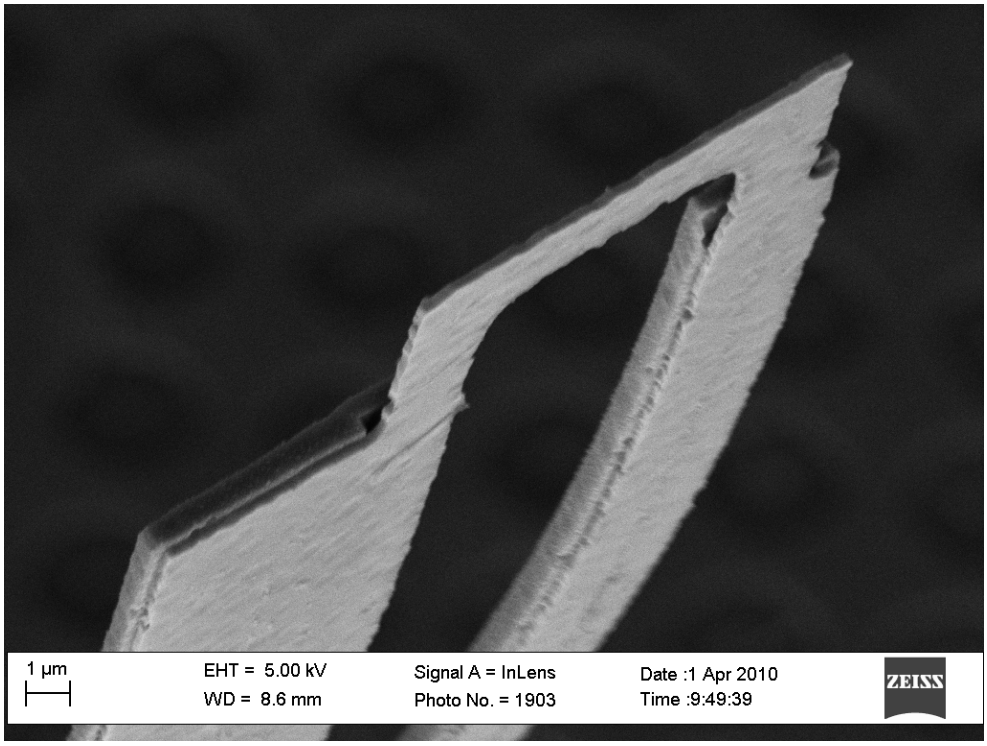

Figure 48. Detail of a poly-silicon thermal isolation region connecting two photoresist bimorphs

4.2 Discussion of Fabrication

Etching of nitride spacers by HF

Although silicon nitride is etched relatively slowly by HF vapor, significant damage to the nitride spacers was apparent after etching and is shown in Fig. 49, below. However, adhesion of the nitride spacers to the substrate remained adequate and the spacers maintained

electrical insulation of the device, even when sensor paddles were pulled toward the substrate by the application of high voltages. Therefore, the etching of the nitride spacers did not affect the success of the fabrication. As expected, the poly-silicon showed no evidence of attack from the HF vapor etching.

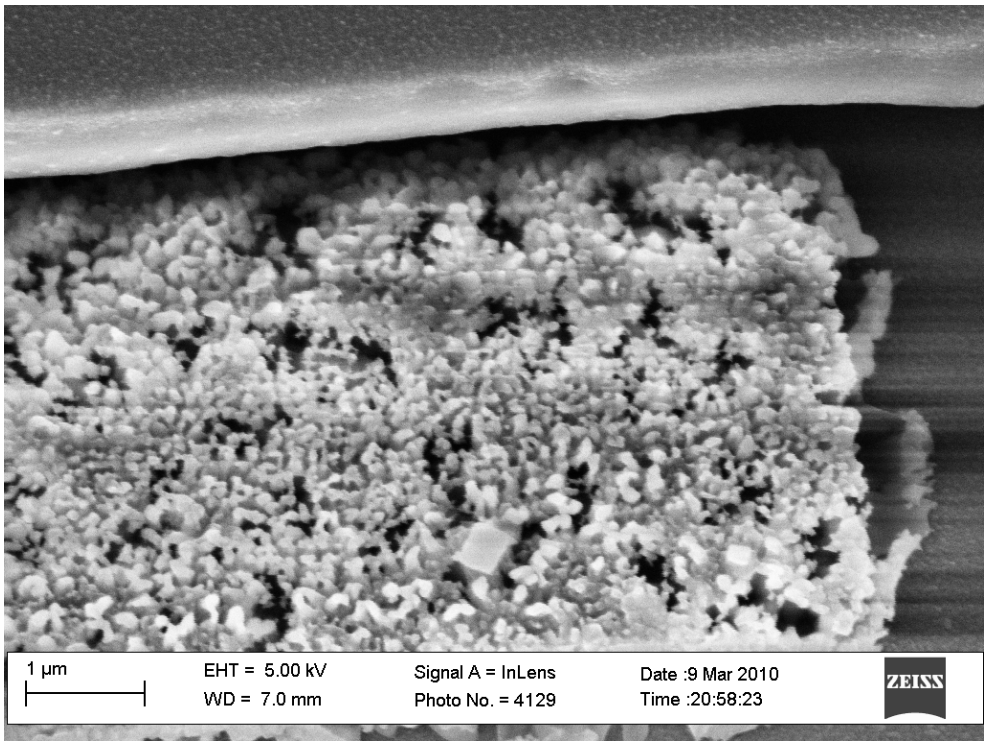

Figure 49. Damage to nitride spacers from HF vapor etching

Photoconductivity and Poly-silicon Deposition

Poly-silicon layers were doped in order to reduce the dependence of their conductivity on the photo-generation of charge carriers. Sensors fabricated with undoped or lightly doped poly-silicon bimorph layers were observed to display significant photoconductivity in response to visible or near infrared light. This effect was observed to interfere with capacitance measurements. The same effect was observed when undoped or lightly doped substrate layers were utilized. Therefore, either a highly doped substrate was used or a layer of highly doped poly-Si was deposited to act as a substrate.

Two different methods of poly-silicon deposition were utilized during this research. In the first, poly-silicon was *in situ* doped using phosphine gas during low pressure chemical vapor deposition (LPCVD) at 615 °C. In the second, the poly-silicon was also deposited via LPCVD (605 °C) but was deposited undoped. An arsenic ion implantation step with a 1000 °C drive in anneal was then performed to achieve doping for the second film. Ion implantation has been widely documented [113] to cause crystal damage in semiconductor films and, as expected, these two doping techniques resulted in poly-silicon films of similar electrical resistances but of different surface roughness and qualities. A comparison of the two poly-silicon films is provided in Figure 50, below. A poly-Si film which was doped via ion implantation is shown on the left

(A) and a film which was doped *in situ* is shown on the right (B). In both images, the etch holes have a diameter of 2 μm. The *in situ* doped film had much less surface roughness and no large defects. However, the film which was doped via ion implantation had much more surface roughness and many large scale defects such as pin-holes and cracks. Both the surface roughness and a large crack, indicated with a red arrow, are visible in Fig. 50 (A). These attributes decreased the definition of fabricated sensor geometries. In addition, defects in the anchors were sometimes observed to allow the HF vapor to etch through the bond pad, compromising the anchor. Ideal poly-silicon films will have low levels of residual stress, no stress gradients, no pin-holes or cracks, and exhibit good uniformity across the wafer. Based on this research, *in situ* doping was observed to produce superior poly-silicon films.

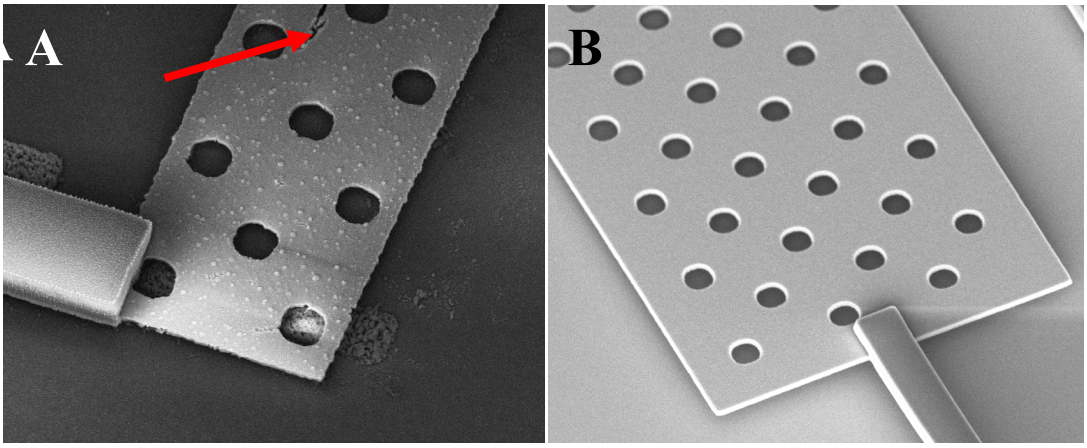

Figure 50. Comparison of poly-silicon film qualities: ion implantation doped (A) and *in situ* doped (B) with arrow indicating a large crack in image A

4.3 Optical Readout Measurements

In order to confirm the response of the fabricated sensors, a simple optical readout method was utilized. For these experiments, simplified devices with a large poly-silicon plate which was attached to the end of two bimorph beams were utilized. The poly-silicon plate acted as a visible light reflector. Since these devices only utilized single beam geometries, the beams were curled away from the substrate due to the effects of residual stress. An example of one such geometry is show in Fig. 51, below. Although the single beam design does not compensate for ambient temperature variations, the deflection of the reflector away from the substrate allowed a high contrast to be achieved when the sensor was observed for optical readout measurements.

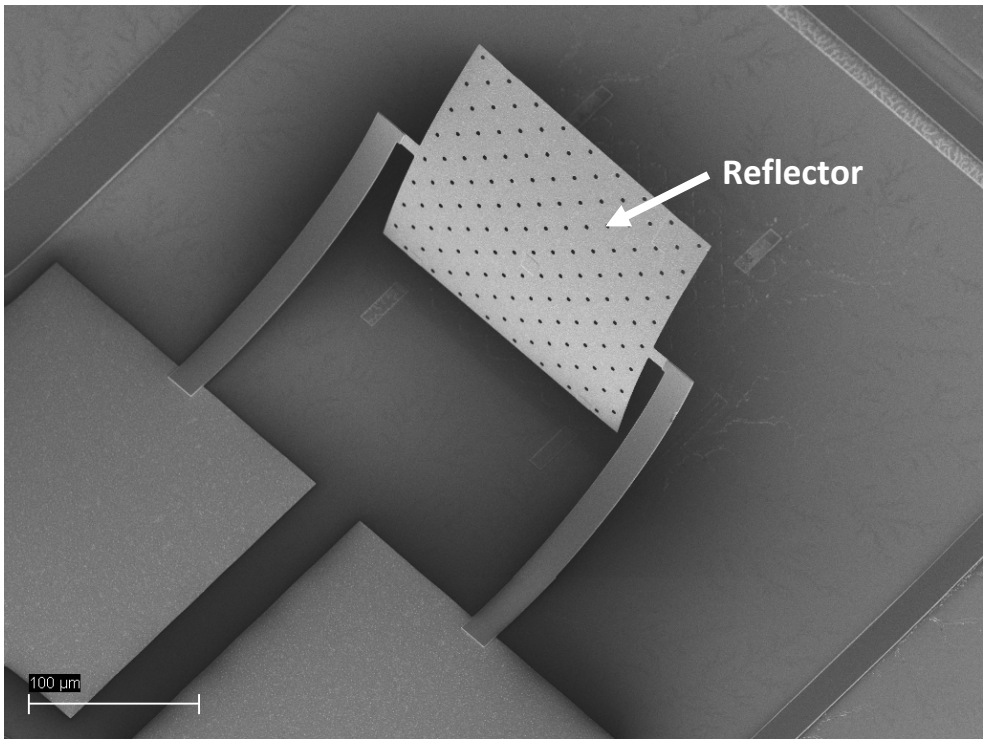

Figure 51. Photoresist on poly-si bimorph sensor with large poly-Si reflector for optical readout

4.3.1 Experimental Setup

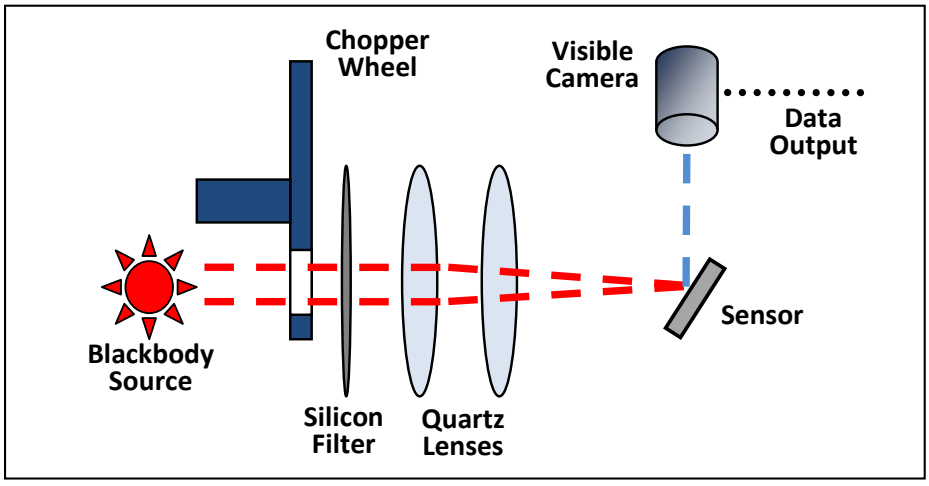

Figure 52. Schematic of optical readout experimental setup

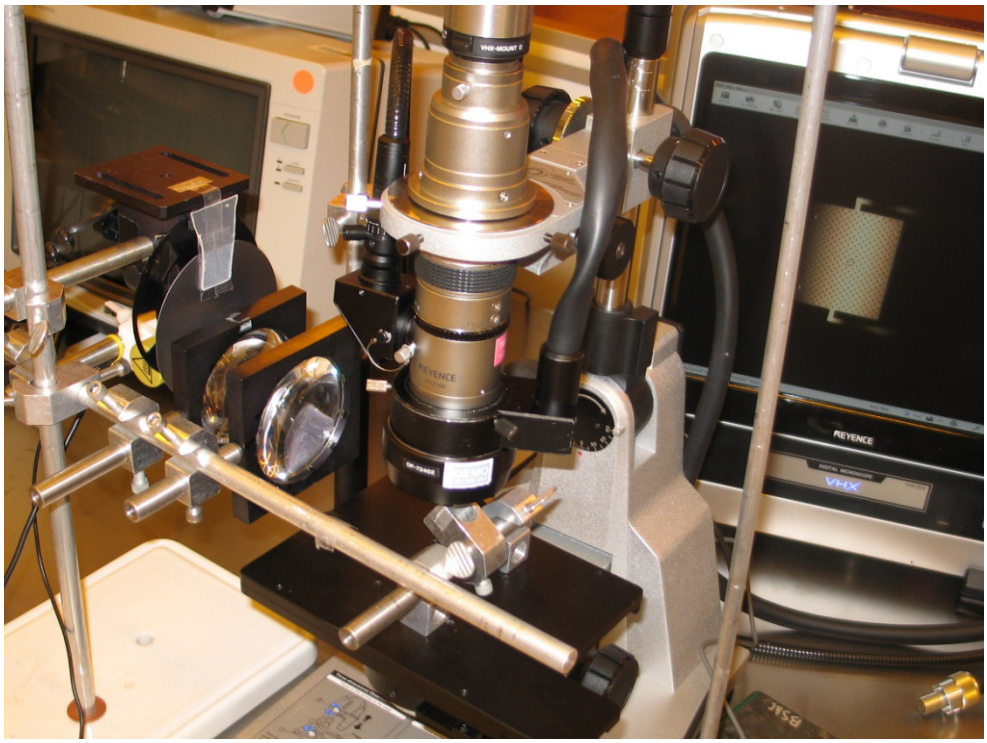

Figure 53. Photograph of optical readout experiment setup

A schematic and photograph of the test setup are shown in Figs. 52 and 53, above. A digital microscope (Keyence VHX-600) was used to record video of a sensor element as it deformed in response to infrared light. The deformation resulted in varying levels of visible light reflected back to the camera. A source which approximated a blackbody emitter (also used in FTIR systems) was used as the infrared source and was controlled by a regulated power supply. A metal chopper wheel with frequency controller (Stanford Systems model SR540) was placed in the light path. Two quartz lenses focused the light to the sensor, which was attached to a metal block using thermal grease. A silicon wafer (thickness ~575 μm) was placed between the chopper wheel and the quartz lenses to block the transmission of visible light from the IR source and also block visible light reflecting from the chopper wheel which might otherwise interfere with the optical readout. Since the sensor was entirely unpackaged, a partial enclosure surrounding the experimental setup was constructed to reduce ambient air currents which could deflect the sensor. This enclosure is not shown in Fig. 53. All equipment was placed on a vibration damped table.

Sensors were individually aligned and tilted in order to maximize reflection to the camera at room temperature and before exposure to the infrared source. After testing, image processing software (ImageJ) was used to extract intensity profiles of the image of the sensor for each video frame. An example of typical images, showing the change in brightness as a result of sensor deflection, is provided in Fig. 54, below. A change in focus is also apparent since the focal length of the camera remained fixed as the reflector tilted from its original plane. For all experiments the microscope lighting, image brightness and contrast, and other adjustments were not changed during measurement.

Two methods were used to extract the optical signal from the recorded images. The first was simply to record the average brightness of the area of the sensor. The second was to

calculate the shift of brightness in the expected direction of motion (left to right, as an example, for the images in Fig. 54). These, and other, methods of image analysis will be discussed in further depth below. Since the measured value of the optical signal was dependent on such factors as lighting conditions, alignment, and the particular sensor which was utilized: optical signals are given in arbitrary units (a.u.) in the results presented below.

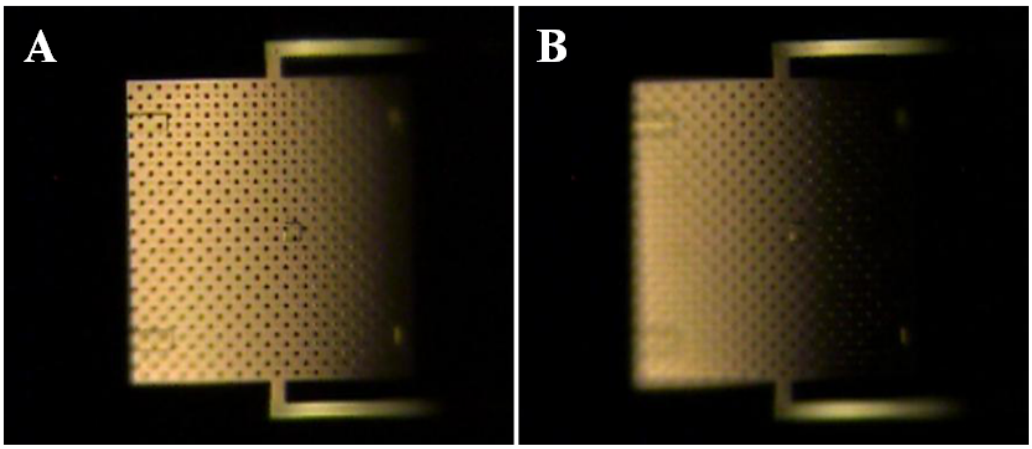

Figure 54. Photographs of individual sensor reflector from optical readout setup before (A) and after (B) IR illumination

4.3.2 Experimental Results

A variety of tests were performed using several different sensor geometries. Sensors utilizing both bimorph beams composed of chitin on poly-silicon and photoresist on poly-silicon were tested. The following section summarizes the most important observations that were made during these tests and provides an initial proof of concept for polymer-ceramic bimorph infrared sensors.

Cycling of Infrared Source

In order to confirm that the sensor was able to detect the heating and cooling of the infrared source, measurements were taken over a 45 second period during which the source was turned on and off twice. The power supply, which self-regulated the applied voltage, was pre-set to deliver 1.30 A. A plot of the average brightness of the image of the sensor as measured by the visible light camera during the duration of the experiment is given in Figure 55, below. Each data point represents a frame of video, which was recorded at 28 frames per second. The times at which the power supply was switched on or off are indicated on the figure (5, 15, 25, and 35 seconds, respectively). These times are approximate since the switching of the power supply was performed manually using a stopwatch. The chopper wheel was aligned to the open position and not rotated during this experiment.

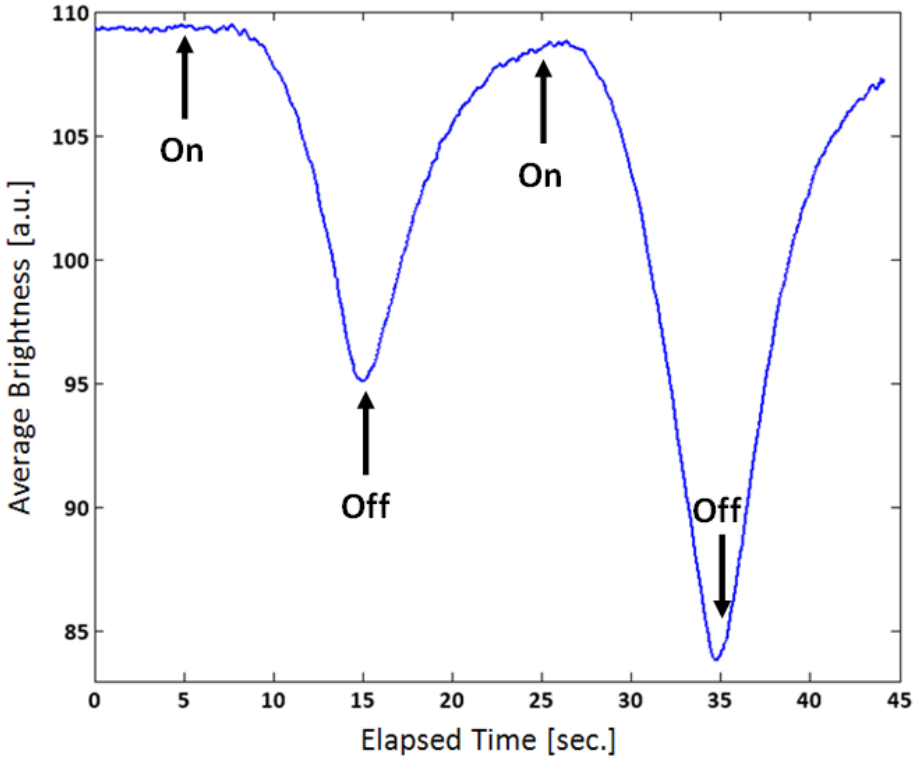

Figure 55. Average brightness of sensor reflector during IR source power cycling, as indicated

For comparison, the temperature of the infrared source was separately measured using an infrared thermometer (Fluke 62 mini). For these measurements, the infrared thermometer was aligned with the IR source without any lenses or filters. Power was supplied to the source in exactly the same way as during measurement with the bimorph sensor. The results of these measurements are shown in Fig. 56, below. For Trials 1 and 2, the power source was switched on and regulated to 1.30 A, as before. For Trails 3 and 4, the power was switched off after having been applied at 1.30 A for a period of at least 1 minute. The infrared thermometer was limited in range to a maximum temperature of about 500 °C. Some variability and the rise and fall times was observed and was likely due to differences in starting temperatures of the filament of the source and fixturing as well as variability in the power controller.

Initial heating of the filament to an equilibrium temperature was observed to require longer than 10 seconds, which suggests that the rate of change of the signal during the experiment shown in Fig. 55, above, was not likely to be primarily limited by the response time of the bimorph sensor, but rather the actual rate of change of temperature of the IR source.

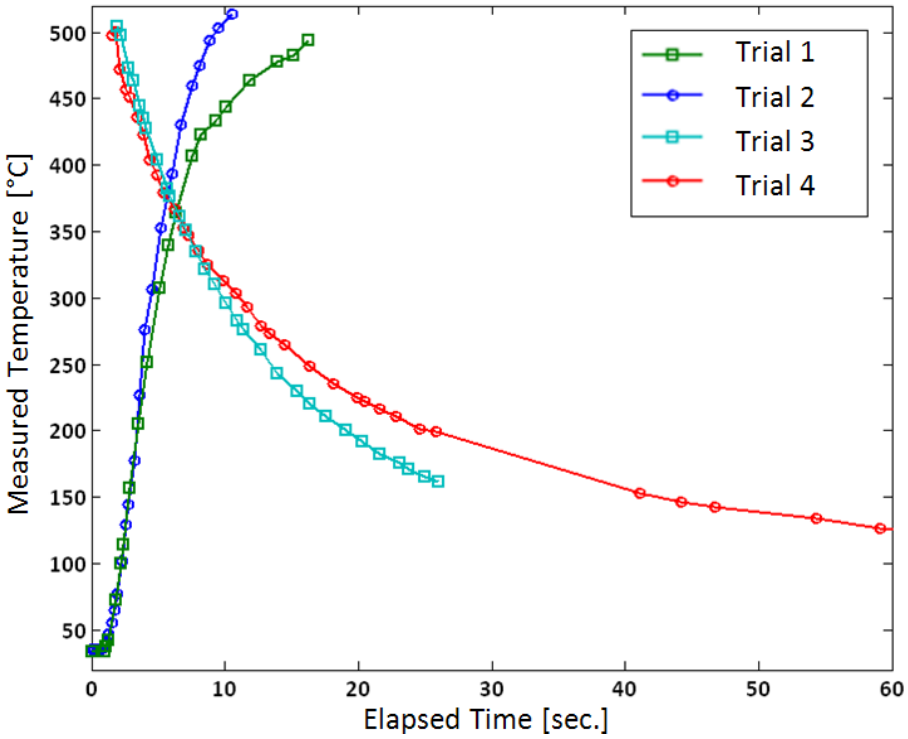

Figure 56. Heating (Trials 1 and 2) and cooling (Trials 3 and 4) of the infrared source as measured with an infrared thermometer

Chopped Signals and Time Response of Sensor

In order to characterize the speed of the bimorph sensors, the response of a sensor to periodic signals created by a mechanical chopper wheel was measured. The chopper wheel (a metal wheel with equally spaced holes) was rotated at a measured rate in order to periodically block the path from the IR source to the sensor. The chopping rate was controlled by a frequency controller and rotated while the IR source had reached a steady state of illumination after at least a minute. Images of the sensors were recorded at a sampling rate of 28 Hz. The same filters and lenses previously described were also used for this experiment.

Representative waveforms for indicated chopping rates of 8, 4, and approximately 1-2 Hz are presented in Fig. 57, below. The vertical lines in the figure show the period of the indicated chopping frequency. It should be noted, however, that at 1-2 Hz, the rotation of the chopper wheel was observed to be somewhat unsteady and irregular. The indicated frequencies are approximate because the frequency controller for the chopper wheel only had a resolution of 1 Hz. Running averages of 2, 4, and 7 points were taken for the 8, 4, and 1-2 Hz signals, respectively. Instead of average brightness, an optical signal based on the movement of a fixed intensity was utilized. This method will be discussed in further depth below.

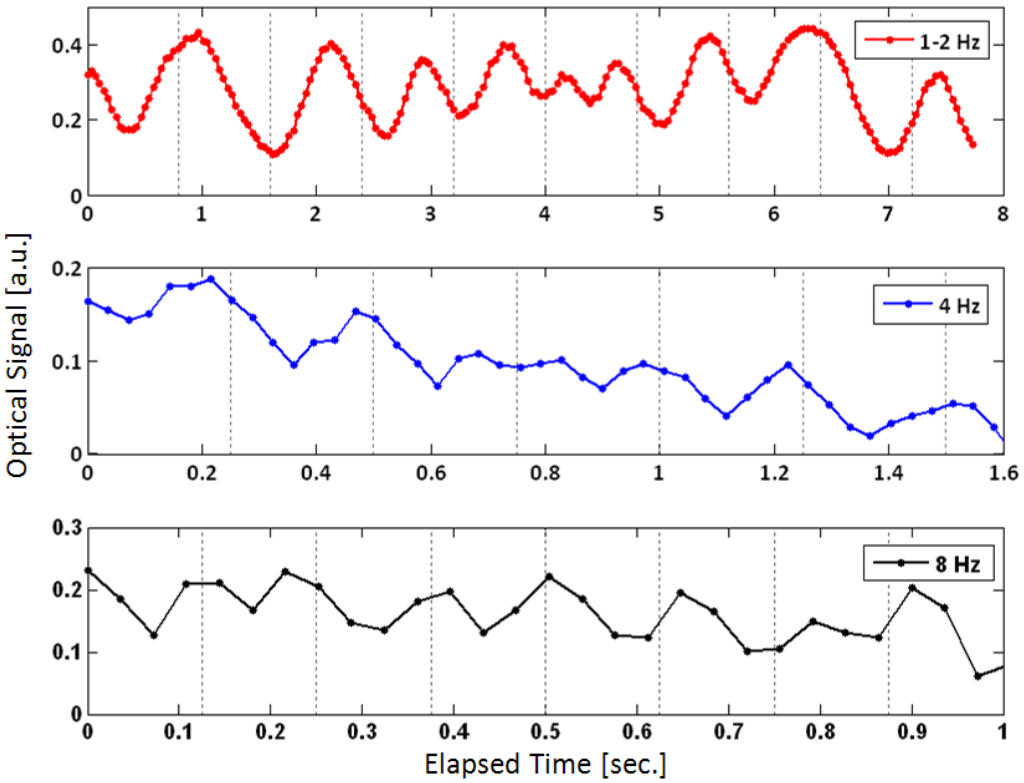

Figure 57. Sample waveforms for chopped signals at indicated frequencies and at a sampling rate of 28 Hz

In order to compare the signal from the sensor to noise and signal drift, measurements were made for identical conditions with and without power supplied to the IR source. The results of one such comparison are presented in Fig. 58, below. In the control trial, Trial 1, no power was supplied to the IR source, although the chopper wheel was run at an indicated frequency of 5 Hz. In Trial 2, the IR source was switched on at the start of data collection while the chopper wheel was maintained at the same frequency as in Trial 1. The warming of the IR source is clearly evident in Trial 2, as is the signal created by the chopper wheel once the IR source rose in temperature. A detailed view of the waveforms during the last three seconds of both of these trials is provided in Fig. 59, below, in which the approximate frequency of the chopper wheel is indicated by vertical dashed lines.

A clear periodic signal which is coincident with the expected frequency of chopping (5 Hz) is visible in Trial 2 but absent from Trial 1, as expected. A signal to noise ratio of approximately 9 was measured. However, significant signal drift was observed in Trial 1 which is visible in Fig. 58. This drift has several possible causes including the influence of ambient air currents, changes in the ambient or microscope lighting, and slight movements of the sensor, source, lenses, or stage. The sampling rate was 28 Hz.

Overall, signals of at least 5 Hz were clearly measured by the sensor. In order to achieve 30 frames per second, the typical requirement for uncooled imagers, a response time of shorter than 10 ms is required [50]. A faster sampling rate would be required to confirm this performance in future experiments.

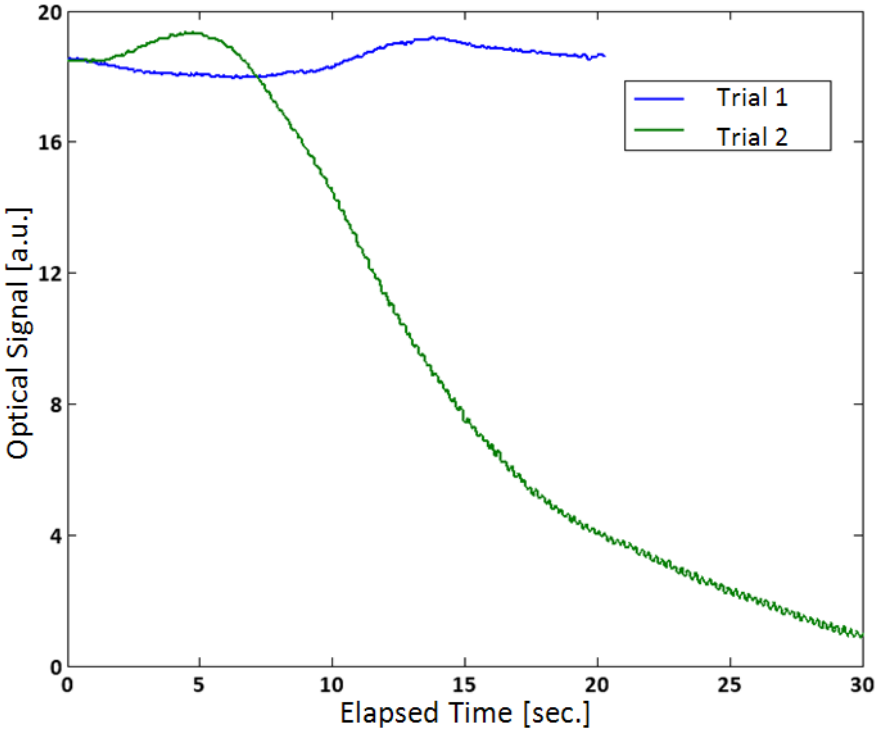

Figure 58. Signal (Trail 2) to noise (Trail 1) comparison

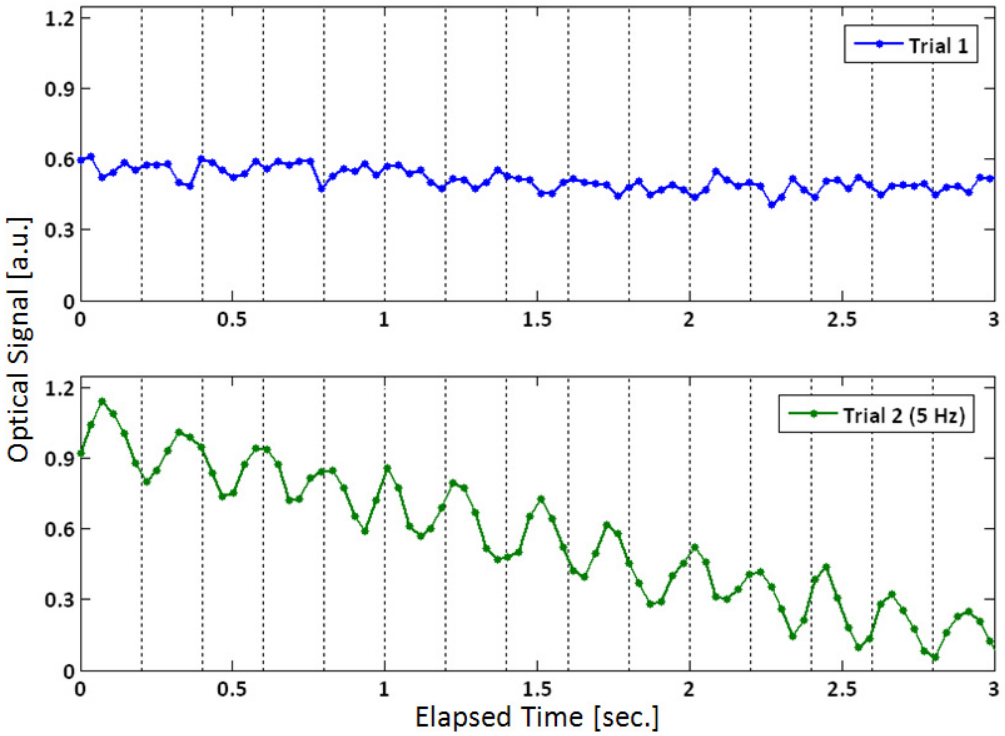

Figure 59. Signal (Trial 2) to noise (Trail 1) comparison detail

Temperature Response of Sensor

In order to characterize the temperature response of the fabricated sensors, devices which did not include ambient temperature compensating double-beam designs were utilized with the optical readout scheme. A die containing such a device was attached to the top of a thin metal plate using thermal grease. A Kapton heater was attached to the bottom of the metal plate and a thermocouple was taped to the top of the metal plate directly adjacent to the sensor die. The die was then aligned with the microscope as previously described. A photograph of this experimental set-up is provided in Fig. 60, below, in which the image of the sensor reflector is visible on the microscope screen.

The temperature of the plate was controlled by slowly varying the power supplied to the heater. As the temperature was varied, still images of the sensor and measurements of the thermocouple temperature were simultaneously recorded. The thermocouple reader was limited to a resolution of 0.1 °C. A plot of the results of this experiment is provided in Fig. 61, below.

To assess the noise level of the sensor, measurements were taken over a period of about 5 minutes while no power was supplied to the heater and the sensor and stage were at thermal equilibrium with the ambient. The temperature of the thermocouple was observed to remain steady at 20.5 °C during this interval. A noise level of between 0.51 and 1.39 a.u. was observed during this interval.[2] Assuming a linear response of the sensor for the measured temperature difference of 20 to 30 °C, the responsivity of the sensor was measured to be approximately 5 a.u/°C.

Following previously published methods [51], these measurements indicated a noise equivalent temperature difference[3] (NETD) of between 100 and 280 mK within the limited range which was measured. Since the resolution of the thermocouple was limited to 0.1 °C, these results suggest that the observed temperature sensitivity may be limited by the resolution of measured temperature rather than noise inherent to the sensor or readout scheme. A more precise experimental setup would be necessary to measure the extent of the bimorph device's temperature sensitivity.

[2] The noise level was measured by taking the standard deviation of the signal or the difference between the maximum and minimum signals, yielding values of 0.51 and 1.39 a.u, respectively.

[3] The NETD is the difference in temperature of the sensor (or blackbody target) which produces a signal-to-noise ratio of unity in the output of the sensor. NETD can describe the response of a sensor to either the actual temperature variation of the sensor or temperature variations of an observed IR target.

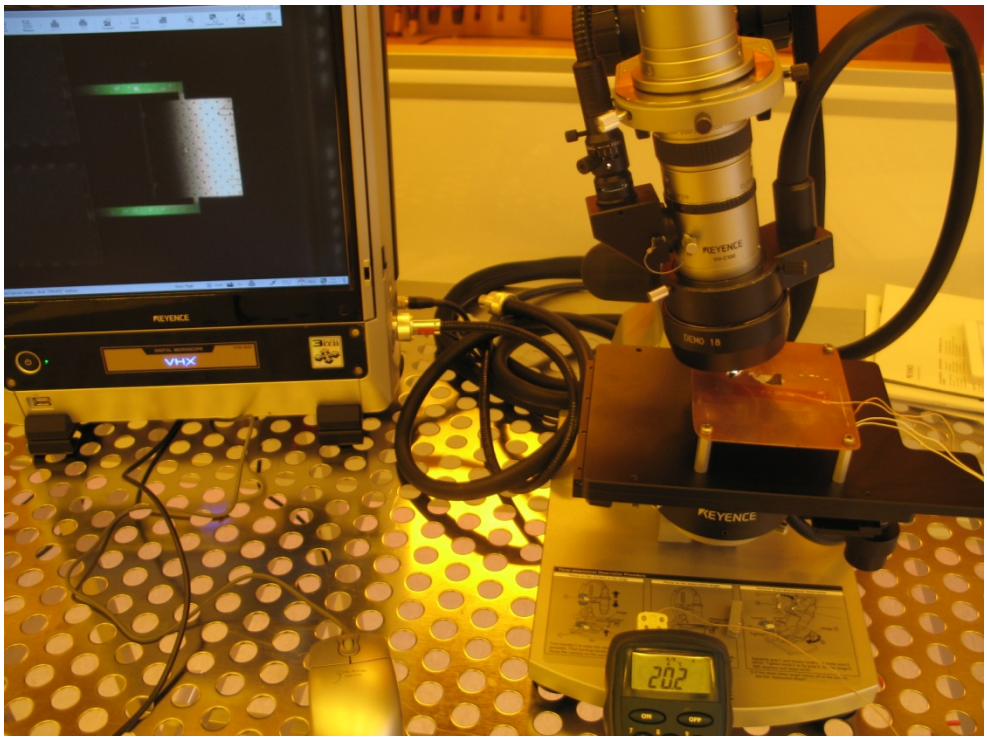

Figure 60. Experimental setup for optical readout of temperature controlled sensor

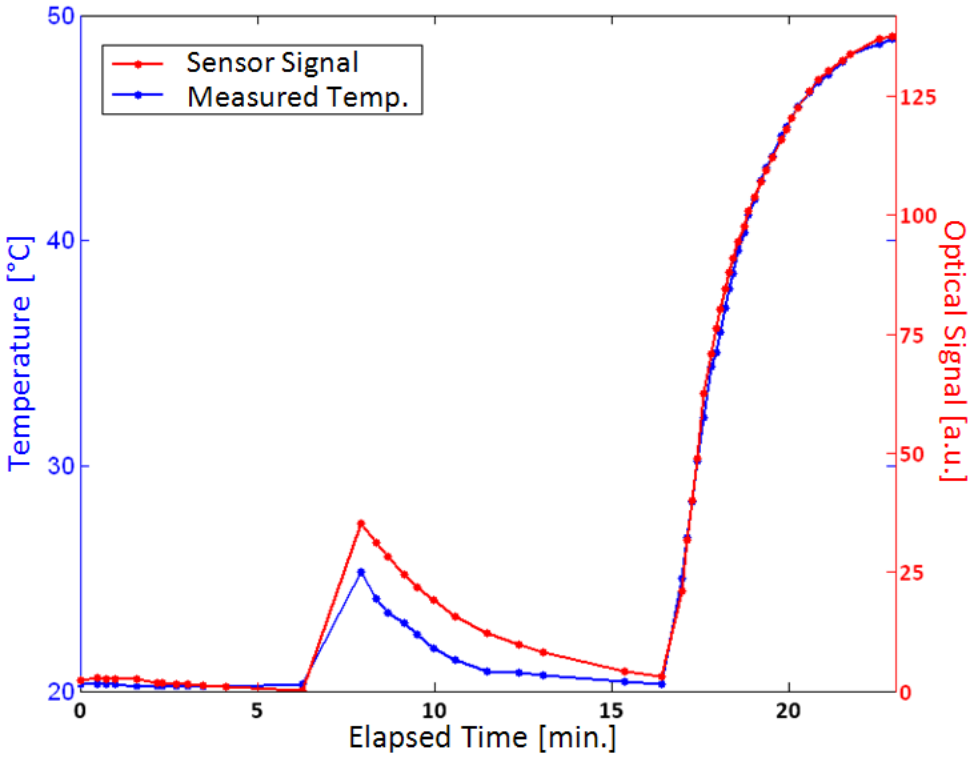

Figure 61. Sensor signal and measured temperature near sensor die as power to heater was slowly varied

Performance Estimate

Although it is difficult to achieve a precise assessment of the performance of the sensors fabricated in this research without a fully characterized IR source and optical setup, a reasonable estimate of performance can be still be made. One way to estimate the performance is to compare the responsivity of the sensor to the observed level of noise, as was done in the previous section for temperature testing.

In order to infer the temperature responsivity of the sensor (defined as the change in sensor signal per change in temperature of the IR source), the sensor signal and IR source temperature were measured as the IR source was being heated by a controlled power source. These tests are shown in Figs. 55 and 56 and are described above. The optical signal was recorded by measuring the "center of mass" of the brightness of the image profile of the sensor. This method will be discussed in further depth below. Although not recorded simultaneously, by assuming the warming rate of the IR source was similar for both experiments (an assumption supported by Fig. 56) and normalizing the times in both trials with respect to the start of application of power to the IR source, a roughly linear region of IR source warming and sensor response can be compared. The changes in sensor signal and measured IR source temperature for the time period from 5 to 7 seconds after power was applied to the IR source are shown in Fig. 62, below. Assuming a linear trend within this limited time period, a sensor signal response of approximately 4.5 $a.u./sec$. was observed during an inferred rate of change of temperature of the IR source of ~51 $°C/sec$. This suggests a temperature responsivity of about .088 $a.u./°C$.

In order to assess the noise level of the sensor, the optical signal during a period of 5 seconds before power was supplied to the IR source was recorded. This data is shown in Fig. 63, below. The noise level was calculated to range from 0.0325 to 0.115 a.u. by taking either the standard deviation of the data or the difference between the maximum and minimum reading during the sample period (not adjusting for the observed signal drift), respectively. For this experiment, the optical signal was recorded at a sampling rate of 28 Hz and subjected to a running average of six data points.

Using the previously calculated value of .088 $a.u./°C$ for the temperature responsivity, these noise measurements indicate an experimental noise equivalent temperature difference (NETD) of 360 to 1300 mK. This result will be discussed in the conclusion of this chapter.

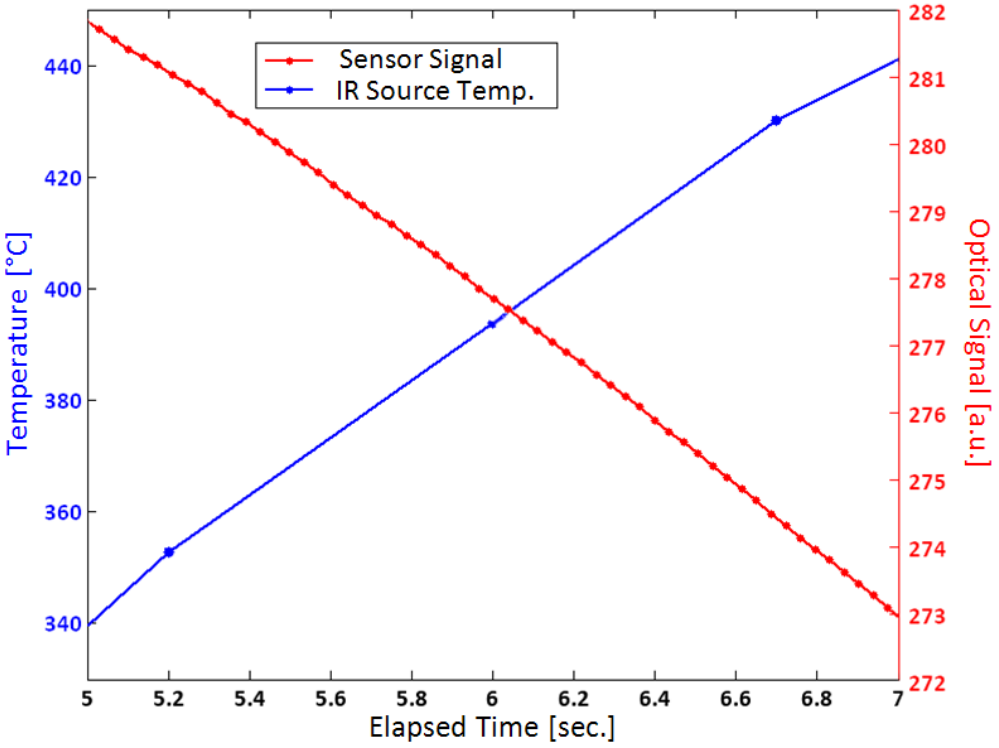

Figure 62. Detail of sensor signal and measured IR source temperature over a limited time period

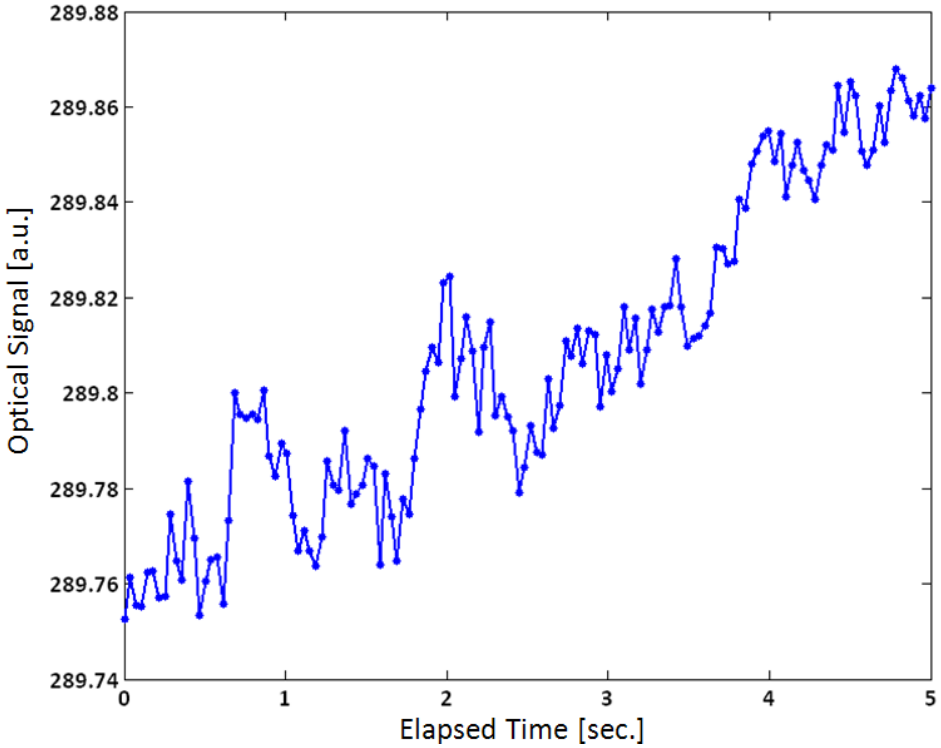

Figure 63. Sensor signal noise before power was applied to IR source

4.3.3 Discussion

Topics related to image analysis, the experimental setup, and hysteresis effects are discussed in this section. Conclusions based on both optical and capacitance experiments will be presented at the end of this chapter.

Optical Readout Method: Image Analysis

In order to extract a quantitative signal from the images observed in an optical readout scheme, some sort of image analysis is required. The simplest method (and probably the most easily directly perceived by a human observer) is to take the average brightness intensity of the area of a sensor. However, for most imaging systems with integrated signal processing, extracting data based on a simple algorithm would also be readily feasible.

For the purposes of this research, several algorithms were tested and compared. The first of these was edge detection. For this algorithm, the apparent motion of the edge of the reflector was calculated based on identifying the abrupt change in intensity from the reflection of the mirror and the background. A sample intensity profile, extracted from the images[4] in Fig. 54, above, is shown in Fig. 64, below, and serves to illustrate the edge detection concept The profile represents a horizontal cross section of the images with y-values corresponding to the average intensity of each column of pixels. For a fixed brightness threshold of 20, the left edge of the profile shifts from a position of about 25 to 5 for image profiles A to B.

The second method was to calculate the shift of brightness in the expected direction of motion (left to right, as an example, for the images in Fig. 54). This was accomplished by taking a weighted average of the positions of the columns of pixels from left to right, with the average brightness of the column acting as the weighting factor. This method can also be thought of as the "center of mass" of the brightness in the horizontal direction. In the profiles shown in Fig. 64, the "center of mass" shifts from position 125 to 67 for profile A to B.

These algorithms were all found to produce meaningful data for all experiments. However, depending on the particular device and the nature of the experiment, certain algorithms were found to perform better than others. For example, in some situations the average brightness was found to exhibit an inflection that was not present in the signal from the IR source or temperature stimulus. This effect was likely due to the reflector reaching a peak reflection angle throughout its range of motion and then passing it, producing a signal which rose and fell even though the mirror was experiencing steady deflection in a single direction. This inflection was usually not observed in the "center of mass" or edge detection algorithms. For all data presented above, the "center of mass" algorithm was used, except in Fig. 55 where average brightness was used. Algorithms which tracked motion were also found to have lower noise levels, in general, than those which measured average brightness. This was probably due to their limited dependence on random fluctuations in the overall brightness of the image recorded by the CCD camera. The linearity of the sensor response for different algorithms also varied significantly and for different individual sensors and alignments.

Further study is required in order to optimize the methods of an optical readout scheme for these sensors but is beyond the scope of this research. Goals for future optical setups include

[4] Image data was extracted using the program ImageJ and was limited to only the area of the images where the sensor reflector was positioned.

achieving high signal to noise ratios, a high dynamic range, ease of alignment and calibration, and strong repeatability. In future array imaging systems, the choice of an image processing technique will depend on factors such as available resolution (when imaging a full sensor array), the required imaging rate, and focusing and alignment constraints.

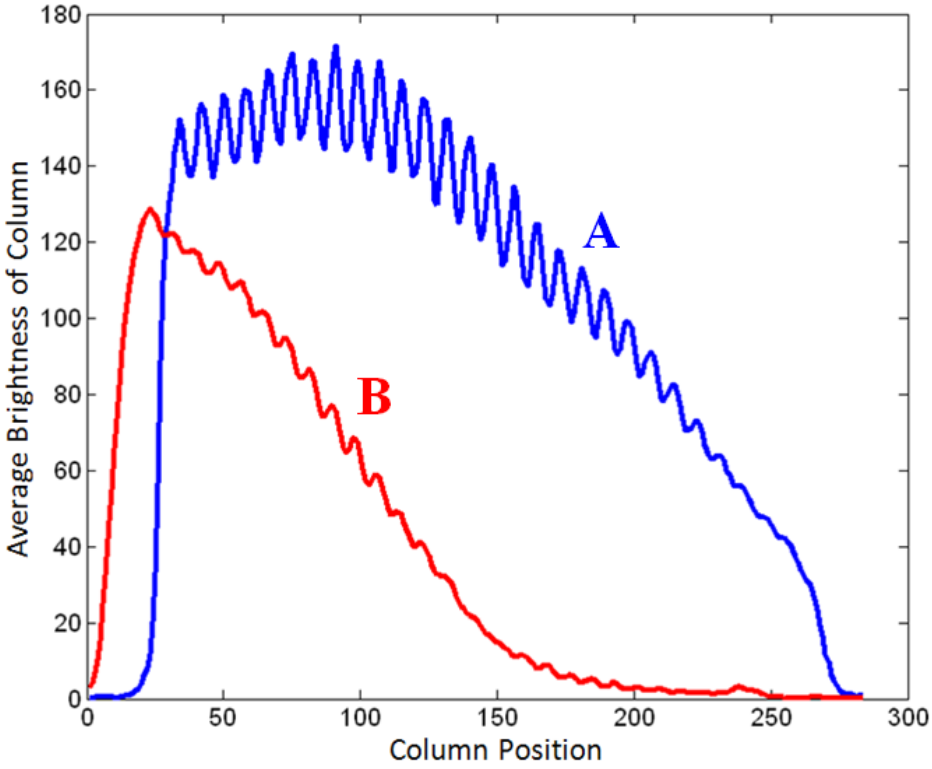

Figure 64. Sample intensity profiles of sensor images from optical readout

Optical Readout Method: Reflector Design and Alignment

In addition to the image processing technique employed, reflector geometry and sensor design also influence the characteristics of the sensor's response. A high contrast between the reflector and the background is desirable. In this research, this contrast was achieved by utilizing reflectors which were tilted at an angle to the substrate due to the effects of residual stress. This allowed the camera to be aligned to the reflectors and not the substrate. However, for ease of alignment and pixel-to-pixel uniformity, it would be desirable to incorporate a double bimorph beam geometry, which would compensate for the curvature of the beams from residual stress and allow the reflector to remain flat, relative to the substrate, at thermal equilibrium. One possible way to achieve contrast in this configuration would be to etch the substrate such that the plane of the substrate near the reflector was angled to reflect away from the camera. Anisotropic bulk micromachining is one way to achieve this geometry and will be discussed in the next chapter.

The shape of the reflector should also be considered when optimizing the optical readout. Reflectors with curvature, gratings, or patterns may yield improved performance, depending on the chosen image processing analysis. The effect of the rows of etch holes on the optical profile of the reflectors in this research, for example, are clearly seen in Fig. 64 and may have the

potential to enhanced the performance of certain image processing methods. Curved reflectors could be produced by patterning a small area of polymer on, for instance, the outside border of the reflector.

Transmission of Optics

As previously described, two quartz lenses and a silicon wafer were placed in the optical path between the IR source and the sensor during these experiments. Although the actual transmission of light through the optical setup in this research was not measured and would depend on the thicknesses and characteristics of the particular lenses and filters used, the relative transmission of light of varying wavelengths through reference samples of these materials is shown in Fig. 65, below. Since silicon does not transmit light with wavelengths shorter than about 1 μm and quartz blocks wavelengths longer than about 3.6 μm, the vast majority of the energy transmitted to the sensor from the IR source was expected to fall within a range of 1.0 – 3.6 μm. This range of wavelengths includes the SWIR band and part of the MWIR band.

Besides limiting the wavelengths of light transmitted, the filter and lenses present significant loss mechanisms because of absorption, reflection, and scattering. No anti-reflective coatings were utilized. Furthermore, focusing of the light by the lenses and alignment with the sensor were performed by hand and were less than optimal. The effects of these considerations on the performance of the sensor will be discussed in further depth below.

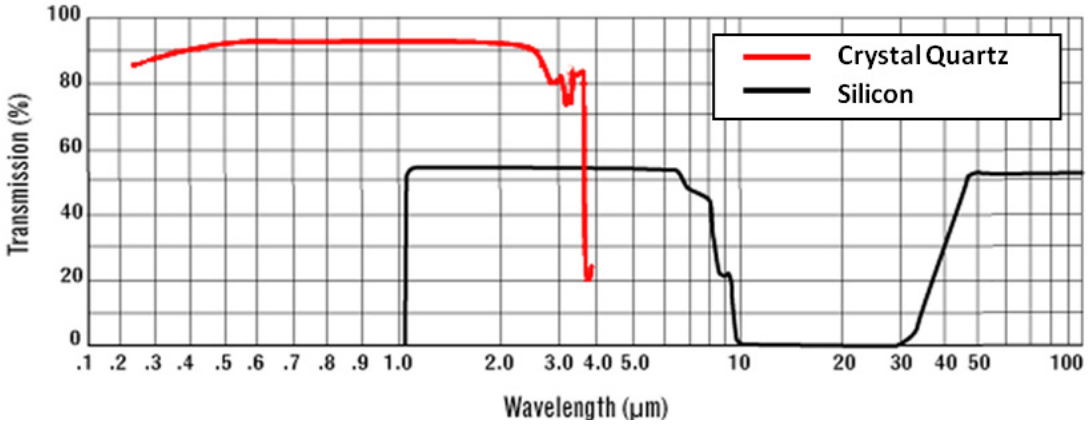

Figure 65. Transmission spectra for reference samples of filter and lens materials [114]

Hysteresis

During temperature controlled experiments, such as those previously described and presented in Fig. 61, significant hysteresis was observed when the sensor was exposed to large temperature variations. Cycling the sensors from 20 to 50 °C was observed to cause an offset in the signal level from its previous room temperature value once it was returned to room temperature after thermal cycling. There are several possible causes of this phenomenon including changes to the polymer with respect to the level of absorbed moisture, crystallinity, cross-linking, or chemical phase. Hysteresis was observed in sensors with both photoresist and chitin as the polymer layer.

It has been shown by Mueller that these effects may be mitigated through thermal annealing and, in the case of chitin, by increasing the degree of acetylation [83]. Since the degree of acetylation for the fabricated chitin sensors in this work was only about 58%, as described in Chapter 2, improvements may be seen by modifying the reacetylation process to achieve more complete conversion to chitin. Additionally, hysteresis effects may be mitigated by packaging sensors in an inert environment or at reduced pressure. Finally, it should be noted that these effects may not be significant for the temperature changes which would be typically experienced by sensors in actual imaging systems.

4.4 Capacitance Measurements

Although not as successful as the optical readout scheme, progress toward a capacitance readout setup was made and an initial proof of concept was demonstrated. The following section describes the experimental setup, initial experimental results, and discusses future work in light of these findings.

4.4.1 Experimental Setup

A commercially available CMOS integrated circuit (Irvine Sensors MS3110) was utilized for capacitance measurements along with a custom printed circuit board and chip wiring board. The MS3110 works as a switched capacitor integrator and operates based upon a sequence of charging the sense capacitors and transferring the charge to a op-amp integration capacitor [115]. A schematic of this concept is presented below in Fig. 66, below, and the transfer function of the circuit is shown in Eq. (44):

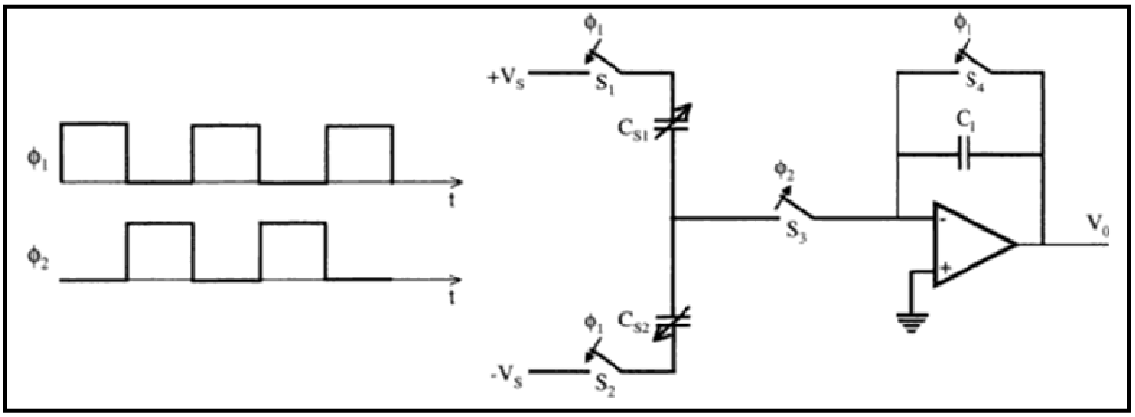

Figure 66. Schematic of switched capacitor integrator found in MS3110 capacitance readout integrated circuit chip [115]

$$V_O = \left(\frac{C_{S1} - C_{S2}}{C_1}\right) V_S \tag{44}$$

where the output and input voltages are given by V_O and V_S, respectively, and C_{S1} is the capacitance of the sensor. The circuit includes programmable feedback and balancing capacitors, C_1 and CS_2, which can be adjusted and stored via an on-chip EEPROM. In order to limit the effects of stray capacitance, sensor dies were wire-bonded to a die wiring board and attached to a custom printed circuit board, shown in Fig. 67, below.

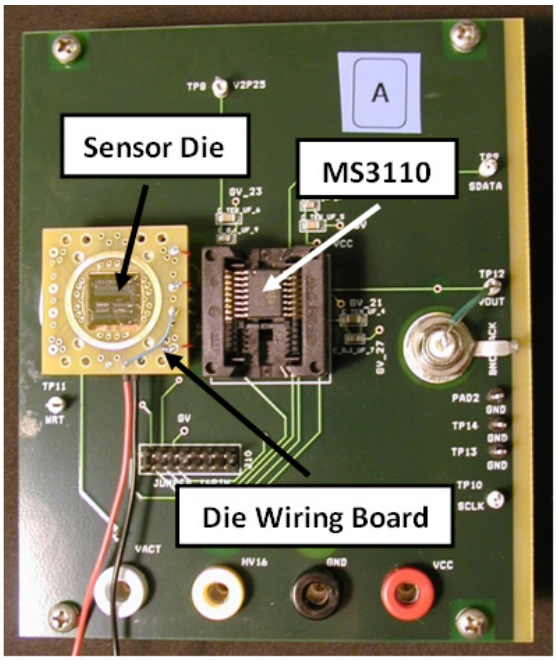

Figure 67. Capacitance readout printed circuit board with sensor die and MS3100 readout IC chip

4.4.2 Experimental Results

A variety of fabricated sensors were tested including simple bimorph cantilever arrays, such as those shown in Fig. 24, above, and residual stress compensated double beam sensors similar to the sensor shown in Fig. 42, above. Large noise levels, electrostatic pull-in, and the influence of stray capacitance prevented meaningful measurements to be made using the double beam sensors. These effects will be discussed in further depth below. However, while extremely limited in their performance due to the effects of residual stress, as previously discussed, the deflection of simple bimorph cantilever arrays was measured and correlated with modeled values. Three different bimorph cantilever arrays were deflected by a stream of air while video and capacitance measurements were simultaneously recorded. The deflection of the beams was measured by video analysis and used to model the predicted change in capacitance based on both parallel plat and fringing field capacitance models. These modeled values were compared with the changes in capacitance indicated by the capacitance readout IC chip (MS3110). The results of this correlation for the three separate devices are shown in Fig. 68, below. Error bars on this figure are based on measurement uncertainties. Changes in capacitance as low as 0.01 pF were measured and correlated with modeled values.

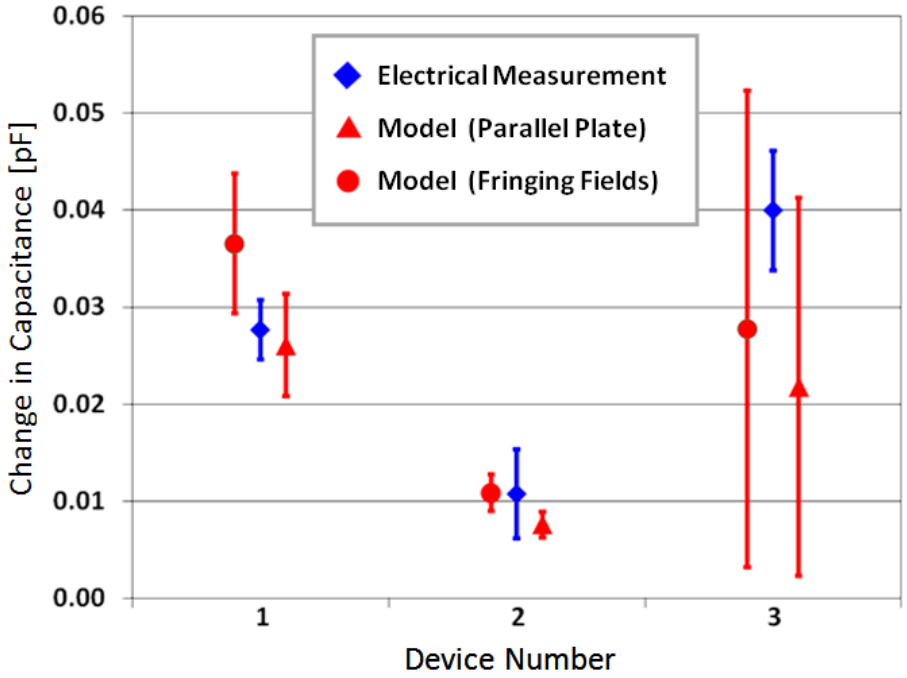

Figure 68. Correlation of experimental and modeled change in capacitance for known sensor deflections

4.4.3 Discussion

Although double beamed bimorph devices with residual stress compensation based on the design presented in Chapter 3 were successfully fabricated, measuring these devices with the current capacitance readout setup proved to be quite difficult. Fundamentally, there is a competition between the goal of maintaining the small dielectric gaps needed to achieve relatively large changes in capacitance for small mechanical deflections and the difficulties that these small gaps create in manufacturing and measurement. Small gaps present obvious difficulties during the release of structures since they increase the tendency of these structures to adhere to the substrate or experience stiction. In addition, small gaps increase the sensitivity of released structures to electrostatic pull-in, as well as to electrostatic deflections caused by electrical measurements.

Further investigation is required to gain a more complete understanding of the sources of noise which were observed in the fabricated double beam sensors and other failure mechanisms which prevented measurement of infrared light. Alternative capacitance readout setups should also be pursued.

4.5 Conclusions

Thermo-mechanical infrared sensors based on novel polymer-ceramic bimorph beams were designed and successfully fabricated. Both optical and capacitance readout experiments were performed to test the sensors fabricated for this research. Although significant progress

toward an improved sensor design for use with a capacitance readout scheme was achieved, the most promising experimental results were observed using the optical readout scheme.

While other researchers have used either lasers [116] or collimated light [51] with precise optical alignments, the optical readout technique employed in this research used diffuse and ambient lighting and did not require precise alignment. Some other researchers have employed AFM systems or interferometers [44] for optical readouts, but the technique used in this research utilize widely available and inexpensive CCD technology. The potential for this approach to be applied to focal plane arrays of sensors has been demonstrated elsewhere [47]. Although a digital microscope was used for the optical readout in this research for ease of alignment and setup, sensors were also easily observable using off-the-shelf digital cameras. This work demonstrates the feasibility of a simple and low cost optical setup being compatible with the sensors designed through this research.

By directly controlling the temperature of a sensor die, a temperature resolution as low as 100 mK was demonstrated. However, is it likely that this measurement was limited by the precision of the experimental setup and that the performance of the sensor has the potential to significantly exceed this figure.

A noise equivalent temperature difference (NETD) of as low as 360 mK was estimated based on measurements made by a single pixel operating within a limited range and responding to an actual IR target. Signals at frequencies of at least 5 Hz were clearly observable for a sampling rate of 28 Hz. These are surprisingly impressive achievements considering that the sensor was uncooled, unpackaged, not temperature stabilized, and tested in a very simple and un-optimized optical setup which was focused and aligned by hand. Although these results should not be interpreted as being completely representative of the performance of these sensors (since testing was preliminary and figures estimated for limited conditions), an encouraging and clear proof of concept has been demonstrated.

Significant gains in performance will be observed by reducing losses through the optical setup, increasing sensor absorption, optimizing the readout mechanism and image analysis method, and packaging the sensor in a reduced pressure environment. It has been estimated [51] that eliminating only the absorption and reflection of infrared light caused by the silicon wafer (which served to act as a filter) in the optical experiments previously discussed in this chapter would reduce the NETD of the sensor by 32%. Suggestions for future improvements which may be achieved through future work will be discussed in the next chapter.

Chapter 5: Conclusion

The concluding chapter of this dissertation presents a summary of findings and discusses the results of this research. Suggestions for future work are also offered that will aid subsequent researchers who seek to improve the current design and work towards the application of this research to a fully functional infrared imaging system.

5.1 Summary and Conclusion

This dissertation has described the design, fabrication, and testing of thermo-mechanical infrared sensors based on MEMS polymer-ceramic bimorph beams. Polymer based bimorph structures have the potential to achieve thermal sensitivities of more than 100 times those of simple cantilever bimorphs composed of gold on silicon. In addition to improving thermal sensitivity, polymer based bimorphs exhibit wavelength selective absorption of infrared light. This characteristic may allow for reduced system cost by eliminating the need for certain infrared filters, or enable imaging arrays with simultaneous sensitivity to multiple wavelength bands. Although polymers have long been recognized as superior materials for MEMS thermal bimorphs, the difficulties involved in their use in this application had prevented researchers from integrating them into their designs. This research, however, has demonstrated the feasibility of using batch fabricated polymer-ceramic MEMS bimorphs for use as thermal infrared detectors.

Sensors utilizing bimorphs composed of both OCG-825 photoresist on poly-silicon and the biopolymer chitin on poly-silicon were fabricated. Photoresist was chosen due to its ease of fabrication and chitin was selected based on its use in the highly sensitive infrared organs of the beetle, *Melanophila acuminata*. A novel chitosan photolithography process was previously developed for this research. In this work, the chitosan process was improved and also modified to include a process for the reacetylation of the chitosan layer to chitin, which is a much more useful form of the polymer for this application. Fabricated bimorphs based on chitin exhibited lower levels of residual stress and less sensitivity to relative humidity than those based on chitosan.

A sensor design based on polymer-ceramic bimorph beams was developed. This design incorporated a geometry which achieved a predictable sensor geometry regardless of the level of residual stress in the polymer layers. This is an important feature since residual stress is very difficult to reliably control in polymer thin films. This geometry also reduces sensitivity to ambient temperature variations. Novel features such as vertically tilted thermal isolation regions and integrated backside shielding of certain device regions were proposed for enhanced sensitivity. Silicon nitride spacers were incorporated into the design in order to reduce sticking during fabrication and prevent electrical shorting in the event of electrostatic pull-in.

Sensors were successfully fabricated and presented. The sensor paddle at the end of fabricated devices was shown to be flat and suspended above the substrate, even for sensors with severe bimorph curvature due to residual stress. Although not experimentally tested, a four by four array of chitin devices, which may serve as a template for larger arrays in future work, was fabricated.

Fabricated sensors were experimentally tested using both optical and capacitance readout methods. Capacitance measurements were made on simple cantilever bimorph devices and correlated with models. Changes of capacitance as low as 0.01 pF were observed. However, high levels of noise, the effects of stray capacitance, and electrostatic pull-in effects prevented successful measurements of sensors based on double bimorph beam design. Promising results were, however, obtained through the optical readout method.

The optical readout method used in this research relied on a digital camera observing the change in reflection of visible light from the sensors as they mechanically deformed in response to heating cause by infrared light. In order to obtain quantitative measurements, image analysis was performed. While the feasibility of simply observing the average brightness of a sensor was demonstrated, several simple image processing algorithms were tested and shown to increase the signal to noise ratio. An IR source approximating a blackbody was combined with a series of filters and lenses to limit transmission of light to the sensor to wavelengths from approximately 1.0 to 3.6 μm (SWIR and partial MWIR).

Signals created by a mechanical chopper wheel, which periodically blocked light from the IR source, were recorded by the sensor for frequencies of at least 5 Hz (for a 28 Hz sampling rate). By comparing the rise in the sensor signal to a known rate of warming of the IR source and the measured noise level at equilibrium, a NETD of as low as 360 mK was measured. Although these results should not be interpreted as being completely representative of the performance of these sensors (since testing was preliminary and figures estimated for limited conditions), an encouraging and clear proof of concept was demonstrated. Significant gains in performance will be observed by reducing losses through the optical setup, increasing sensor absorption, optimizing the readout mechanism and image analysis method, and packaging the sensor in a reduced pressure environment.

5.2 Discussion

Although originally intending to primarily pursue a capacitance readout approach, throughout the course of this research the author has become convinced that the advantages of optical readout techniques are compelling. By utilizing the mature and inexpensive technology of CCD cameras, a fast-track to commercialization for thermo-mechanical infrared detectors has been identified. In addition, the ability to utilize signal processing and other adjustments following fabrication may be especially useful in mitigating some of the difficulties that are inherent to using polymers as a thermo-mechanical MEMS material. By separating the fabrication of the MEMS sensors from the readout system, a natural efficiency is created since off-the-shelf components can be integrated with simple, low-cost, MEMS. Since no CMOS would be directly integrated on the MEMS chip, the usual fabrication limits imposed by compatibility would not apply. The lack of need for any electrical contact to the sensors allows for the exclusive use of insulating materials in the sensor supports, leading to higher sensitivities. Finally, although not currently feasible, the potential to use sensors designed for optical readouts to create a direct-view infrared camera (such that instead of a CCD camera, the human eye is used) which consumes no power whatsoever is undeniably exciting.

5.3 Future Work

In order to further demonstrate the merit of this technology and move it closer to commercialization, future work should focus on performance improvement, increasing the ease and simplicity of fabrication, and demonstrating the unique benefits of polymers as infrared absorbers such as wavelength specific absorption. Suggestions for future work in the areas of sensor design, fabrication, and experimental testing are presented in this section.

5.3.1 Sensor Design

- Replace poly-silicon with silicon dioxide (SiO_2) as the bottom layer of the bimorph. Since SiO_2 has a lower coefficient of thermal expansion and lower thermal conductance than poly-silicon, thermal bimorph sensitivity will be improved. In addition, SiO_2 will be compatible with etching of the silicon substrate. If used with a capacitance readout scheme, a thin layer of a conducting material will be required to make electrical contact to the sensor.

- Reduce anchor size and redesign geometry for high fill factor arrays. Many examples exist in the literature. Further improvement of fill factor can be obtained by adjacent sensors in an array "sharing" outer bimorph legs as proposed by Jones *et al.* [52]. For use with capacitance readouts, this design would required that metal traces only connect to one side of each pixel to avoid shorting all pixels together.

- Modify sensor design to improve the contrast between the sensor paddle and the substrate when residual stress compensated double bimorph beam devices are used with an optical readout. The substrate should either be etched away beneath the sensor or etched to form an angle where light would be reflected away from the readout camera. Completely removing the substrate below the reflector area would have the advantage of limiting losses through the substrate if the sensor is illuminated by infrared from the bottom of the die. A bulk micro-machining process for metal-ceramic devices has been published [51].

5.3.2 Fabrication

- Investigate methods of improving adhesion of chitin to the bottom layer of the bimorph regions. These may include chemical treatments, surface modification of the bottom layer, or three dimensional geometries such as those published by Hunter *et al.* [37]. The results of this investigation may also be used with other polymers.

- Integrate one of the several proposed methods of shielding outer bimorph legs and thermal isolation region from infrared light, the simplest of which may be patterning an integrated metal shield on the back side of the wafer.

- Maximize degree of acetylation achieved during chitosan conversion by increasing the duration of acetic anhydride exposure and raising the reaction temperature. More complete conversion to chitin will further reduce the influence of humidity on chitin sensors, improve the chemical and mechanical properties of the film, and may reduce hysteresis in sensors.

- Investigate method of improving removal of PMMA and photoresist from chitin in order to prevent the need for precisely timed etching. Chitin films with a high degree of acetylation may be more resistant to chemical attack and expand the number of options available.

- If using poly-silicon as the bottom layer of bimorph beams, use *in situ* doping for reduced stress and fewer defects.

- Develop a process whereby two or more unique polymers may be patterned on alternating rows of pixels in a sensor array. This process would enable a "color" infrared camera if each polymer has different absorption characteristics according to the wavelength of light and would be a novel use of polymer-ceramic bimorph devices.

5.3.3 Experimental Testing

- Utilize a characterized IR source in a calibrated test setup in order to more accurately measure the performance of sensors. A photodetector may be used to confirm the level of irradiation near the sensor.

- Characterize the sensitivity of sensors as a function of the wavelength of light using various band pass filters and investigate the correlation with known FTIR absorption spectra of chitin and other polymers.

- Utilize a faster CCD camera in order to more accurately measure the time response of sensors.

- Further investigate image analysis methods, especially for use with images of large arrays when the available resolution of a single pixel will be reduced. Investigate effects of alignment errors on sensitivity. Demonstrate the feasibility of using an off-the-shelf digital camera for optical readout.

- Confirm and quantify performance improvements of sensors in reduced pressure environments. Investigate effect of reduced pressure or inert packaging on hysteresis and long term stability of sensors.

Bibliography

1. Vondran, T., K.H. Apel, and H. Schmitz, *The infrared receptor of Melanophila acuminata De Geer (Coleoptera: Buprestidae): ultrastructural study of a unique insect thermoreceptor and its possible descent from a hair mechanoreceptor.* Tissue and Cell, 1995. **27**(6): p. 645-658.
2. Rogalski, A., *Infrared detectors: status and trends.* Progress in Quantum Electronics, 2003. **27**(2-3): p. 59-210.
3. Niklaus, F., C. Vieider, and H. Jakobsen. *MEMS-based uncooled infrared bolometer arrays: a review*. 2007: SPIE.
4. FLIR Systems Inc, *FLIR Q3 Investor Presentation*. 2009.
5. Jones, C.D.W., et al., *Opportunities in uncooled infrared imaging: A MEMS perspective.* Bell Labs Technical Journal, 2009. **14**(3): p. 85-98.
6. Hudson, R.D., *Infrared System Engineering*. 1969, New York: John Wiley and Sons.
7. Howard, G.B. *Application of airborne thermal infrared imaging for the detection of unexploded ordnance*. 2001: SPIE.
8. Kaplan, H., *Practical applications of infrared thermal sensing and imaging equipment*. 3rd ed. 2007, Winter Park, FL: SPIE Publications.
9. Maldaque, X.P.V., *Theory and practice of infrared technology for nondestructive testing*. 2001, New York: Wiley-Interscience.
10. FLIR Systems, Inc. [cited Jan 11, 2010]; Available from: http://www.flir.com/thermography/americas/us/
11. Balaras, C.A. and A.A. Argiriou, *Infrared thermography for building diagnostics.* Energy and Buildings, 2002. **34**(2): p. 171-183.
12. Grinzato, E., V. Vavilov, and T. Kauppinen, *Quantitative infrared thermography in buildings.* Energy and Buildings, 1998. **29**(1): p. 1-9.
13. Prokoski, F. *History, current status, and future of infrared identification*. in *Computer Vision Beyond the Visible Spectrum: Methods and Applications, 2000. Proceedings. IEEE Workshop on*. 2000.
14. Jiang, L.J., et al., *A perspective on medical infrared imaging.* Journal of Medical Engineering & Technology, 2005. **29**(6): p. 257-267.
15. Von Bierbrauer, A., et al., *Infrared thermography in the diagnosis of Raynaud's phenomenon in vibration-induced white finger.* Vasa, 1998. **27**(2): p. 94-99.
16. Gimzewski, J.K., et al., *Observation of a chemical reaction using a micromechanical sensor.* Chemical Physics Letters, 1994. **217**(5-6): p. 589-594.
17. Holst, G.C., *Common sense approach to thermal imaging*. 2000, New York: JCD Pub. 377.
18. [cited 2010 Jan 10]; http://en.wikipedia.org/wiki/Infrared
19. Kruse, P.W., *Uncooled Thermal Imaging: Arrays, Systems, and Applications*. Tutorial Texts in Optical Engineering, ed. A.R. Weeks. 2001, Bellingham, WA: SPIE Press.
20. Driggers, R., P. Cox, and T. Edwards, *Introduction to Infrared and Electro-Optical Systems*. 1999, Norwood, MA: Artech House, Inc.
21. Li, B., *Design and simulation of an uncooled double-cantilever microbolometer with the potential for ~mK NETD.* Sensors and Actuators A: Physical, 2004. **112**(2-3): p. 351-359.

22. Rogalski, A., *Comparison of photon and thermal detector performance*, in *Handbook of Infrared Detection Technologies*, M. Henini and M. Razeghi, Editors. 2002, Elsevier Science: New York. p. 5-75.
23. Gordon, N.T. and I.M. Baker, *Assessment of Infrared Materials and Devices*, in *Infrared detectors and emitters: materials and devices*, P. Capper and C.T. Elliott, Editors. 2000, Kluwer Academic Publishers.
24. Putley, E.H., *Thermal Detectors*, in *Optical and Infrared Detectors*, R.J. Keyes, Editor. 1977, Springer-Verlag: New York. p. 71-100.
25. Jones, R.C., Proc. IRIS 2, 1957. **1**: p. 9-12.
26. Kinch, M.A., *Fundamentals of Infrared Detector Materials*. 2007, Wellingham, WA: SPIE Press.
27. Kruse, P., L. McGlauchlin, and R. McQuistan, *Elements of infrared technology: generation, transmission, and detection*. 1962: Wiley. 448.
28. Djuric, Z., et al., *A new approach to IR bimaterial detectors theory.* Infrared Physics & Technology, 2007. **50**(1): p. 51-57.
29. Scribner, D.A., M.R. Kruer, and J.M. Killiany, *Infrared focal plane array technology.* Proceedings of the IEEE, 1991. **79**(1): p. 66-85.
30. Wadsworth, A., et al., *Aircraft experiments with visible and infrared sensors.* International Journal of Remote Sensing, 1992. **13**(6): p. 1175-1199.
31. Murphy, D., et al. *640 x 512 17 μm microbolometer FPA and sensor development*. 2007: SPIE.
32. Wood, R.A., *Monolithic silicon microbolometer arrays*, in *Uncooled infrared imaging arrays and systems*, P.W. Kruse and D.D. Skatrud, Editors. 1997, Academic Press: San Diego.
33. Hanson, C.M. *Barriers to background-limited performance for uncooled IR sensors*. 2004: SPIE.
34. Hoof, C.V. and P.D. Moor, *PolySiGe uncooled microbolometers for thermal IR detectoion*, in *Handbook of Infrared Detection Technologies*, M. Henini and M. Razeghi, Editors. 2002, Elsevier Science: New York. p. 449-479.
35. Parrish, W.J. and I. James T. Woolaway. *Improvements in uncooled systems using bias equalization*. 1999: SPIE.
36. Kang, S.G., Y.S. Lee, and H.C. Lee, *CMOS readout circuit allowing microbolometer arrays to operate without temperature stabilisation.* Electronics Letters, 2004. **40**(23): p. 1459-1460.
37. Hunter, S.R., et al. *High-sensitivity 25 μm and 50 μm pitch microcantilever IR imaging arrays*. in *SPIE Defense and Security Symposium*. 2007: SPIE.
38. Barnes, J.R., et al., *A femtojoule calorimeter using micromechanical sensors.* Review of Scientific Instruments, 1994. **65**(12): p. 3793-3798.
39. Barnes, J.R., et al., *Photothermal spectroscopy with femtojoule sensitivity using a micromechanical device.* Nature, 1994. **372**(6501): p. 79-81.
40. Manalis, S.R., et al., *Two-dimensional micromechanical bimorph arrays for detection of thermal radiation.* Applied Physics Letters, 1997. **70**(24): p. 3311-3313.
41. Perazzo, T., et al., *Infrared vision using uncooled micro-optomechanical camera.* Applied Physics Letters, 1999. **74**(23): p. 3567-3569.

42. Zhao, Y., et al., *Optomechanical uncooled infrared imaging system: design, microfabrication, and performance.* Microelectromechanical Systems, Journal of, 2002. **11**(2): p. 136-146.
43. Norton, P.R., et al. *Micro-optomechanical infrared receiver with optical readout: MIRROR*. 2000: SPIE.
44. Lim, S.H., et al., *Design and Fabrication of a Novel Bimorph Microoptomechanical Sensor.* Microelectromechanical Systems, Journal of, 2005. **14**(4): p. 683-690.
45. Corbeil, J.L., et al., *"Self-leveling" uncooled microcantilever thermal detector.* Applied Physics Letters, 2002. **81**(7): p. 1306-1308.
46. Hunter, S.R., et al. *High-sensitivity uncooled microcantilever infrared imaging arrays*. 2006: SPIE.
47. Jack, P.S. *High frame rate imaging using uncooled optical readout photomechanical IR sensor*. 2007: SPIE.
48. Weidong, W., et al., *Simulation and experimental studies of an uncooled MEMS capacitive infrared detector for thermal imaging.* Journal of Physics: Conference Series, 2006: p. 350.
49. Wachter, E.A., et al., *Remote optical detection using microcantilevers.* Review of Scientific Instruments, 1996. **67**(10): p. 3434-3439.
50. Datskos, P.G., N.V. Lavrik, and S. Rajic, *Performance of uncooled microcantilever thermal detectors.* Review of Scientific Instruments, 2004. **75**(4): p. 1134-1148.
51. Yi, Y., et al., *An Uncooled Microcantilever IR Detector Based on Bulk Silicon Technique*, in *Transducers*. 2009: Denver, CO.
52. Jones, C.D.W., et al., *MEMS thermal imager with optical readout.* Sensors and Actuators A: Physical, 2009. **155**(1): p. 47-57.
53. Kwon, I.W., et al., *Design and fabrication of a capacitive infrared detector with a floating electrode and thermally isolatable bimorph legs.* Sensors and Actuators A: Physical, 2008. **147**(2): p. 391-400.
54. Mao, M., et al. *Direct-view uncooled micro-optomechanical infrared camera*. in *Micro Electro Mechanical Systems, 1999. MEMS '99. Twelfth IEEE International Conference on*. 1999.
55. Liu, C., *Recent Developments in Polymer MEMS.* Advanced Materials, 2007. **19**(22): p. 3783-3790.
56. Chatzandroulis, S., et al., *Capacitive-type chemical sensors using thin silicon/polymer bimorph membranes.* Sensors and Actuators B: Chemical, 2004. **103**(1-2): p. 392-396.
57. Snow, D., et al., *Static deflection measurements of cantilever arrays reveal polymer film expansion and contraction.* Journal of Colloid and Interface Science, 2007. **316**(2): p. 687-693.
58. Thundat, T., et al., *Micromechanical radiation dosimeter.* Applied Physics Letters, 1995. **66**(12): p. 1563-1565.
59. Wachter, E.A. and T. Thundat, *Micromechanical sensors for chemical and physical measurements.* Review of Scientific Instruments, 1995. **66**(6): p. 3662-3667.
60. Yan, X., X.K. Xu, and H.-F. Ji, *Glucose Oxidase Multilayer Modified Microcantilevers for Glucose Measurement.* Analytical Chemistry, 2005. **77**(19): p. 6197-6204.
61. Liu, K. and H.-F. Ji, *Detection of Pb2+ Using a Hydrogel Swelling Microcantilever Sensor.* Analytical Sciences, 2004. **20**(1): p. 9-11.

62. Zhang, Y., et al., *A pH Sensor Based on a Microcantilever Coated with Intelligent Hydrogel.* Instrumentation Science & Technology, 2004. **32**(4): p. 361 - 369.
63. Calleja, M., et al., *Polymeric Cantilever Arrays for Biosensing Applications.* Sensor Letters, 2003. **1**: p. 20-24.
64. Ravi Kumar, M.N.V., *A review of chitin and chitosan applications.* Reactive and Functional Polymers, 2000. **46**(1): p. 1-27.
65. Skjåk-Braek, G., T. Anthonsen, and P.A. Sandford, *Chitin and chitosan: sources, chemistry, biochemistry, physical properties, and applications*. 1989: Kluwer Academic Pub.
66. Khor, E. and L.Y. Lim, *Implantable applications of chitin and chitosan.* Biomaterials, 2003. **24**(13): p. 2339-2349.
67. Ravi Kumar, M., *Chitin and chitosan fibres: A review.* Bulletin of Materials Science, 1999. **22**(5): p. 905-915.
68. Shahidi, F., J.K.V. Arachchi, and Y.-J. Jeon, *Food applications of chitin and chitosans.* Trends in Food Science & Technology, 1999. **10**(2): p. 37-51.
69. Muzzarelli, R.A.A., et al., *Removal of trace metal ions from industrial waters, nuclear effluents and drinking water, with the aid of cross-linked N-carboxymethyl chitosan.* Carbohydrate polymers, 1989. **11**(4): p. 293-306.
70. Cheng, J.C.-M., *Chitosan as a MEMS Engineering Material*, in *Electrical Engineering and Computer Science*. 2006, University of California: Berkeley, CA. p. 63.
71. Park, I., et al., *Low temperature, low pressure nanoimprinting of chitosan as a biomaterial for bionanotechnology applications.* Applied Physics Letters, 2007. **90**(9): p. 093902.
72. Wu, L.-Q., et al., *Voltage-Dependent Assembly of the Polysaccharide Chitosan onto an Electrode Surface.* Langmuir, 2002. **18**(22): p. 8620-8625.
73. Karp, J.M., et al., *A photolithographic method to create cellular micropatterns.* Biomaterials, 2006. **27**(27): p. 4755-4764.
74. Koev, S., *Microcantilever Biosensors with Chitosan for the Detection of Nucleic Acids and Dopamine*, in *Electrical Engineering*. 2007, University of Maryland: College Park, MD.
75. Cheng, J.C. and A.P. Pisano, *Photolithographic Process for Integration of the Biopolymer Chitosan Into Micro/Nanostructures.* Microelectromechanical Systems, Journal of, 2008. **17**(2): p. 402-409.
76. Muzzarelli, R.A.A., *Chitin*. 1977, New York: Pergamon.
77. Lammel, G., S. Schweizer, and P. Renaud, *Optical Microscanners and Microspectrometers Using Thermal Bimorph Actuators*. Microsystems, ed. S. Senturia. Vol. 8. 2002, Boston, MA: Kluwer Academic Publishers.
78. Pinnaduwage, L.A., et al., *Sensitive detection of plastic explosives with self-assembled monolayer-coated microcantilevers.* Applied Physics Letters, 2003. **83**(7): p. 1471-1473.
79. Timoshenko, S., *Analysis of Bi-Metal Thermostats.* J. Opt. Soc. Am., 1925. **11**(3): p. 233-233.
80. Gehring, G.A., et al., *Cantilever unified theory and optimization for sensors and actuators.* Smart Material Structure, 2000. **9**: p. 918-31.
81. Wen-Hwa, C., M. Mehregany, and R.L. Mullen, *Analysis of tip deflection and force of a bimetallic cantilever microactuator.* Journal of Micromechanics and Microengineering, 1993(1): p. 4.

82. Krulevitch, P. and G.C. Johnson, *Curvature of a cantilever beam subjected to an equi-biaxial bending moment*. 1998. Medium: ED; Size: 10 p.; Other: FDE: PDF; PL:.
83. Mueller, M., *Biomimetic, Polymer-Based Microcantilever Infrared Sensors*. 2007, University of California - Berkeley: Berkeley, CA.
84. Chen, K.-S., *Techniques in Residual Stress Measurement for MEMS and Their Applications*, in *MEMS/NEMS Handbook Techniques and Applications*. 2006, Springer US. p. 1252-1328.
85. Stoney, G.G., *The Tension of Metallic Films Deposited by Electrolysis.* Proceedings of the Royal Society of London. Series A, 1909. **82**(553): p. 172-175.
86. Fang, W. and J.A. Wickert, *Comments on measuring thin-film stresses using bi-layer micromachined beams.* Journal of Micromechanics and Microengineering, 1995(4): p. 276.
87. Janssen, G.C.A.M., et al., *Celebrating the 100th anniversary of the Stoney equation for film stress: Developments from polycrystalline steel strips to single crystal silicon wafers.* Thin Solid Films, 2009. **517**(6): p. 1858-1867.
88. Amantea, R., et al. *Uncooled IR imager with 5-mK NEDT*. 1997: SPIE.
89. LeMieux, M.C., et al., *Polymeric Nanolayers as Actuators for Ultrasensitive Thermal Bimorphs.* Nano Letters, 2006. **6**(4): p. 730-734.
90. Hunter, S.R. and G. Simelgor, *Apparatus comprising a thermal bimorph with enhanced sensitivity*. 2006, Multispectral Imaging, Inc.: USA.
91. Lin, Y.H., et al., *Trilayered Ceramic-Metal-Polymer Microcantilevers with Dramatically Enhanced Thermal Sensitivity.* Advanced Materials, 2006. **18**(9): p. NA.
92. Jr-Hau, H., et al., *A thermal sensor and switch based on a plasma polymer/ZnO suspended nanobelt bimorph structure.* Nanotechnology, 2009(6): p. 065502.
93. Francis, L.F., et al., *Development and measurement of stress in polymer coatings.* Journal of Materials Science, 2002. **37**(22): p. 4717-4731.
94. Zhang, X., et al., *Residual-stress relaxation in polysilicon thin films by high-temperature rapid thermal annealing.* Sensors and Actuators A: Physical, 1998. **64**(1): p. 109-115.
95. Murray, C.A. and J.R. Dutcher, *Effect of Changes in Relative Humidity and Temperature on Ultrathin Chitosan Films.* Biomacromolecules, 2006. **7**(12): p. 3460-3465.
96. Patel Vijay, R. and M. Amiji Mansoor, *pH-Sensitive Swelling and Drug-Release Properties of Chitosan - Poly(ethylene oxide) Semi-interpenetrating Polymer Network*, in *Hydrogels and Biodegradable Polymers for Bioapplications*. 1996, American Chemical Society: Washington, DC. p. 209-220.
97. East, G.C. and Y. Qin, *Wet spinning of chitosan and the acetylation of chitosan fibers.* Journal of Applied Polymer Science, 1993. **50**(10): p. 1773-1779.
98. Mauf, N. and K. Williams, *An introduction to microelectromechanical systems engineering*. 2nd ed. 2004, New York: Artech House.
99. Storment, C.W., et al., *Flexible, dry-released process for aluminum electrostatic actuators.* Microelectromechanical Systems, Journal of, 1994. **3**(3): p. 90-96.
100. Webster, J.R., et al. *Electrophoresis system with integrated on-chip fluorescence detection*. in *Micro Electro Mechanical Systems, 2000. MEMS 2000. The Thirteenth Annual International Conference on*. 2000.
101. Zhang, Y., et al., *Determination of the degree of deacetylation of chitin and chitosan by X-ray powder diffraction.* Carbohydrate Research, 2005. **340**(11): p. 1914-1917.

102. Leow Cheah, W., A.B. Mohammad, and N.M. Kassim. *Analytical modeling for determination of pull-in voltage for an electrostatic actuated MEMS cantilever beam*. in *Semiconductor Electronics, 2002. Proceedings. ICSE 2002. IEEE International Conference on*. 2002.
103. Chang, W.H., *Analytical IC Metal-Line Capacitance Formulas.* IEEE Transactions on Microwave Theory and Techniques, 1976. **24**(9): p. 608-611.
104. Hu, Y.-C. and C.-S. Wei, *An analytical model considering the fringing fields for calculating the pull-in voltage of micro curled cantilever beams.* Journal of Micromechanics and Microengineering, 2007(1): p. 61.
105. Van Der Meijs, N.P. and J.T. Fokkema, *VLSI circuit reconstruction from mask topology.* INTEGRATION, the VLSI journal, 1984. **2**: p. 85-119.
106. Huang, S., B. Li, and X. Zhang, *Elimination of stress-induced curvature in microcantilever infrared focal plane arrays.* Sensors & Actuators: A. Physical, 2006. **130**: p. 331-339.
107. Arakawa, E.T., et al., *Detection and differentiation of biological species using microcalorimetric spectroscopy.* Ultramicroscopy, 2002. **97**(1-4): p. 459-465.
108. Peng, W., Z. Xiao, and K.R. Farmer, *Optimization of thermally actuated bimorph cantilevers for maximum deflection.* Nanotech Proceedings, 2003. **1**: p. 376-379.
109. Arvi, K., *Analysis and optimization of loaded cantilever beam microactuators.* Smart Materials and Structures, 2000(2): p. 186.
110. Zhao, Y.P., L.S. Wang, and T.X. Yu, *Mechanics of adhesion in MEMS-a review.* Journal of Adhesion Science and Technology, 2003. **17**: p. 519-546.
111. Maboudian, R., *Surface processes in MEMS technology.* Surface Science Reports, 1998. **30**(6-8): p. 207-269.
112. Liddiard, K.C., *Application of interferometric enhancement to self-absorbing thin film thermal IR detectors.* Infrared Physics, 1993. **34**(4): p. 379-387.
113. Madou, M., *Fundamentals of Microfabrication*. 2nd ed. 2002, New York: CRC Press.
114. *Transmission Curves: BK7, Quartz, Ge, Si*. [cited Jan 10, 2010]; Available from: http://rmico.com/technical-notes/bk7-quartz-ge-si.
115. Allen, J.J., *Micro Electro Mechanical System Design*. 2005, Boca Raton, FL: CRC Press.
116. Senesac, L.R., et al., *IR imaging using uncooled microcantilever detectors.* Ultramicroscopy, 2003. **97**(1-4): p. 451-458.